Dynamics of Melt-Lithosphere Interaction

by

Christopher Havlin

B. A., Boston University, 2009

Sc. M., Brown University, 2011

A Dissertation submitted in partial fulfillment of the
requirements for the Degree of Doctor of Philosophy
in the Department of Earth, Environmental, and Planetary Science at Brown
University

Providence, Rhode Island

May 2015

This dissertation by Christopher Havlin is accepted in its present form
by the Department of Earth, Environmental, and Planetary Science as satisfying the
dissertation requirement for the degree of Doctor of Philosophy.

Date ______________ ____

E.M. Parmentier, Ph.D., Advisor

Date ______________ ____

James Gregory Hirth, Ph.D., Advisor

Recommended to the Graduate Council

Date ______________ ____

W. Roger Buck, Ph.D., Reader

Date ______________ ____

Karen M. Fischer, Ph.D., Reader

Date ______________ ____

Alberto Saal, Ph.D., Reader

Approved by the Graduate Council

Date ______________ ____

Peter M. Weber, Dean of the Graduate School

Curriculum Vitæ

Christopher Havlin, born October 27, 1986, Fitchburg, MA.

Education

May 2015	Ph.D. in Geology Brown University, Providence RI Advisors: Marc Parmentier, Greg Hirth
May 2011	Master of Science in Geological Sciences Brown University, Providence RI
May 2009	Bachelor of Arts in Geophysics and Planetary Science Boston University, Boston MA

Honors

2009	Boston University Earth Sciences Undergraduate Research Award
2009	Boston University Center for Space Physics Undergraduate Research Award

Publications

Havlin, C., E.M. Parmentier and G. Hirth, EPSL 2013, Dike propagation driven by melt accumulation at the lithosphere-asthenosphere boundary, http://dx.doi.org/10.1016/j.epsl.2013.06.010.

Havlin, C. and E.M. Parmentier, GRL 2014, Implications for melt transport and source heterogeneity in upwelling mantle from the magnitude of Sp converted phases generated at the onset of melting, http://dx.doi.org/10.1002/2014GL060890.

Talks

2014 AGU Fall Meeting, San Francisco, CA, "Sp receiver functions generated at melting onset: insight from geodynamic models and synthetic receiver functions." (**invited**)

2013 AGU Fall Meeting, San Francisco, CA, "The evolution of lithosphere deformation due to infiltration of asthenosphere melt into a lithosphere with inherited weakness: insight from 2D numerical models of continental rifts"

2012 Boston University Solid Earth Seminar, Boston, MA, "Source limited dike propagation and implications for tectonics." (**invited**)

2012 AGU Fall Meeting, San Francisco, CA,"Development of a sloping lithosphere-asthenosphere boundary and its effect on melt accumulation and lithosphere heating."

2010 AGU Fall Meeting, San Francisco, CA. Talk: "Dike propagation limited by melt extraction; implications for rift initiation."

Absracts

2014 CIG-EarthScope Institute for Lithospheric Modeling Workshop, Tempe, AZ, "Melt migration, accumulation and lithosphere infiltration using the immersed boundary method."

2012 GeoPRISMS Science Workshop for East Africa Rift System, Morristown, NJ, "Lithosphere thinning due to dike propagation at the lithosphere-asthenosphere boundary."

2012 Gordon Conference: Rock Deformation, Andover, NH, "Lithosphere thinning due to dike propagation driven by melt accumulation at the lithosphere-asthenosphere boundary."

2011	AGU Fall Meeting, San Francisco, CA, "Melt transport through the lithosphere by dike injection from a partially molten asthenosphere."
2011	Earthscope Institute: The Lithosphere-Asthenosphere Boundary, Portland, OR, "Dike propagation out of a partially molten boundary layer at the base of the lithosphere: implications for the LAB"
2011	Gordon Research Conference, Interior of the Earth, Holyoke, MA, "The influence of melt extraction from the lithosphere-asthenosphere boundary on the evolution of rifting."
2010	GeoPRISMS RIE Planning Workshop, Santa Fe, NM, "Melt generation and extraction from the upper mantle as a magma source for rifting ."

Teaching and Outreach

2012	Teaching Assistant, Introduction to Solid Earth Geophysics Brown University
2010	Teaching Assistant, Introduction to Solid Earth Geophysics Brown University
Jan. 2013	Exhibition night judge, Blackstone Academy Charter School Pawtucket RI
2012	Lesson planning and teaching, Vartan Gregorian Elementary School Providence RI

Acknowledgments

My sincere thanks and gratitude go out to my advisors, Marc Parmentier and Greg Hirth. Marc's ability to see the physics that control geological processes is inspiring and I am grateful for having benefited from his insight, expertise and instruction. In addition to sharing his vast knowledge of earth materials, Greg's constant encouragement was indispensable, especially when the "re" in research kept repeating. I am also thankful for the other professors on my committee, Alberto Saal, Karen Fischer and Roger Buck, for their valuable insight. Chapter 1 in particular was greatly improved through discussion with Karen.

Throughout my academic journey, I have had the good fortune of learning from many excellent teachers and peers. While I was an undergraduate student at Boston University, Paul Hall was especially influential in setting me down the path of geodynamics. At Brown, in addition to my committee members, Don Forsyth and Reid Cooper were instrumental in shaping my understanding of geophysics and thermodynamics. During my time here, I have also benefited from many scientific discussions with fellow graduate students, especially Amanda Getsinger, Mary Peterson, Kei Shimizu, Nick Dygert and Colin Jackson. My thanks go out especially to the geochemists for answering all my questions and I apologize if my geophysicist brain was at times slow to catch on. Emily Hopper was instrumental in Chapter 1 and patiently answered all my questions on receiver functions. I also enjoyed many discussions on numerical methods and the physics of melt migration with post doctoral researcher, Nan Zhang.

Throughout graduate school, I had the opportunity to attend many conferences that broadened my scientific view and intellectual interests. In particular, the GeoPRISMS workshops on Rift Initiation and Evolution were influential in spurring my interest in continental rifts and I appreciate the emphasis placed on graduate student involvement by conference conveners Maggie Benoit, Tyrone Rooney, Donna Shillington, and Ramon Arrowsmith, who ensured that graduate students were given an opportunity to shape the RIE initiative. I made many close friends and colleagues from which I anticipate many exciting collaborations.

The family of graduate students in the geology department provided day to day support through the ups and downs of graduate school. I have many fond memories of cookouts, the GCB, campfires and bicycle rides and I am thankful for the general good cheer and support of my fellow graduate students.

In particular, there are several people that I am happily indebted to. To Bronwen, I can't thank you enough for our time together and your constant support, especially while I was in the throes of dissertation writing. To my thesis buddy, Amanda, I enjoyed our writing sessions and I appreciate your concern for whether or not I am properly feeding myself (don't worry, I am). To my fellow outdoor enthusiasts and thrill seekers, Danielle, Jeff, Nick and Will, our time in the wilderness was an energizing respite from my computer screen. And thankfully geologic time is much longer than dissertation-writing time and the mountains are still there. Let's go climb them!

My parents and siblings have been an ever present, positive force in my life. I am lucky to have such a loving family and I look forward to the years to come.

And finally, I'd like to thank the Earth, for being so interesting. In the words of John Muir [1], "When we try to pick out anything by itself, we find it hitched to everything else in the Universe."

[1] John Muir, *My first summer in the Sierra.* Vol. 15. Canongate Books, 2010.

Preface

The majority of melt production on Earth occurs in the mantle, yet there are significant gaps in our knowledge of the physical process controlling its ascent from the initial depth of melting to its eventual eruption or emplacement within the crust. Particularly, the processes controlling the transition in magma ascent mechanism from a diffuse, inter-granular porous flow to flow in macroscopic dikes and sills is poorly understood, despite its important role in controlling the supply of melt to eruptive centers. Motivated by recent geophysical observations of a possible melt-rich boundary layer at the base of the lithosphere (e.g. Fischer *et al.*, 2010) and by the importance of melt in assisting continental breakup (e.g. Bialas *et al.*, 2010) and "lubricating" plate boundaries (e.g. Holtzman and Kendall, 2010), the work presented in this dissertation investigates the dynamics of melt generation in the asthenosphere, accumulation at the base of the lithosphere and subsequent infiltration into the lithosphere.

In Chapter 1, we investigate the possibility that the seismic velocity structure produced by the onset of melting can give rise to converted seismic phases. We use a combination of numerical modeling of melt migration and forward modeling of synthetic receiver functions to show that the magnitude of converted phases generated by melting onset depends strongly on the thermodynamic state of the upwelling mantle. We find that the observed phases that have been attributed to melting onset (e.g. Rychert *et al.*, 2013, 2014) are most easily explained with melting of a relatively dry source. Because lavas erupted from regions where melting onset phases have been proposed contain abundant dissolved water, either (1) water is entrained as an initially dry plume passes through a hydrated transition zone or (2) the dependence of seismic velocity on melt fraction is much stronger than the standard relationship used in this study.

In Chapter 2, we consider the dynamics of a partially molten boundary layer at the base of the lithosphere. This work is motivated by seismic observations that record a rapid drop in seismic velocity with increasing depth at the base of the lithosphere (e.g. Gaherty *et al.*, 1996; Tan and Helmberger, 2007; Rychert and Shearer, 2009; Yuan and Romanowicz, 2010; Fischer *et al.*, 2010) that has been attributed in some locations to melt accumulating beneath a solidus isotherm (e.g. Kawakatsu *et al.*, 2009; Schmerr, 2012). Specifically, we use semi-analytical and numerical models to understand how the accumulation of melt at the solidus-geotherm intersection may be relieved by propagation of dikes into the lithosphere. We find that the excess pressure generated in a decompacting boundary layer is sufficient to generate dikes that propagate a short height into the lithosphere where they freeze. Because diking is limited by melt supply, the melt-rich layer is not fully drained so that a quasi-steady state boundary layer of high melt fraction can persist at the base of the lithosphere above regions of melt production.

In the final Chapter, we use the results from Chapter 2 to investigate how melt intruding at the base of the lithosphere may influence the thermal and mechanical evolution of the lithosphere. We formulate a model for extensional environments, where magmatic intrusions can thermally weaken of the lithosphere (Bialas *et al.*, 2010) and control strain accommodation in rift basins (Ebinger and Casey, 2001). Given the potential link between mantle plumes, flood basalts and rifting (e.g. Morgan, 1981, 1983; McHone *et al.*, 2005), we consider the case where melt is generated by a mantle plume at the base of a lithosphere subjected to a horizontal tectonic force. We find that heating of the lithosphere base by intruding dikes can rapidly thin the lithosphere on the order of tens of km Myr^{-1}, resulting in stress concentration and extension onset in the remaining lithosphere with little to no evidence of intrusion at depth. The predicted time between extension onset and mantle lithosphere erosion matches the observed time over which strain accommodation in rift basins transfers from extension along border faults to magmatic accommodation (Ebinger and Casey, 2001). We find that diking from the lithosphere-asthenosphere boundary (a) reduces lateral melt transport, perhaps explaining how lavas erupted in close vicinity within rifts preserve unique characteristics of their source (Rooney, 2010; Rooney *et al.*, 2011) and (b) matches lithosphere erosion rates estimated from thermobarometry of melt inclusions in the western U.S. (Gazel *et al.*, 2012). Finally, the calculated 2-D melt distributions seem to suggest that the rapid velocity decrease observed near the base of the lithosphere in volcanic (Ford *et al.*, 2010; Rychert *et al.*, 2013, 2014; Hopper *et al.*, 2014) and extensional (Lekic *et al.*, 2011; Rychert *et al.*, 2012; Lekic and Fischer, 2013) regions is caused by melt accumulating at its solidus.

References

Bialas, R. W., W. R. Buck, and R. Qin 2010. How much magma is required to rift a continent? *Earth and Planetary Science Letters 292*(1-2), 68–78.

Ebinger, C., and M. Casey 2001. Continental breakup in magmatic provinces: An Ethiopian example. *Geology 29*(6), 527–530.

Fischer, K. M., H. A. Ford, D. L. Abt, and C. A. Rychert 2010. The lithosphere-asthenosphere boundary. *Annual Review of Earth and Planetary Sciences* **38**, 551–575.

Ford, H. A., K. M. Fischer, D. L. Abt, C. A. Rychert, and L. T. Elkins-Tanton 2010. The lithosphere-asthenosphere boundary and cratonic lithospheric layering beneath Australia from Sp wave imaging. *Earth and Planetary Science Letters 300*(3-4), 299–310.

Gaherty, J. B., T. H. Jordan, and L. S. Gee 1996. Seismic structure of the upper mantle in a central Pacific corridor. *J. Geophys. Res. 101*(B10), 22291–22309.

Gazel, E., T. Plank, D. W. Forsyth, C. Bendersky, C. A. Lee, and E. H. Hauri 2012. Lithosphere versus asthenosphere mantle sources at the Big Pine Volcanic Field, California. *Geochemistry, Geophysics, Geosystems 13*(6).

Holtzman, B. K., and J. Kendall 2010. Organized melt, seismic anisotropy, and plate boundary lubrication. *Geochemistry, Geophysics, Geosystems 11*(12), –.

Hopper, E., H. A. Ford, K. M. Fischer, V. Lekic, and M. J. Fouch 2014. The lithosphere–asthenosphere boundary and the tectonic and magmatic history of the northwestern United States. *Earth and Planetary Science Letters*.

Kawakatsu, H., P. Kumar, Y. Takei, M. Shinohara, T. Kanazawa, E. Araki, and K. Suyehiro 2009. Seismic Evidence for Sharp Lithosphere-Asthenosphere Boundaries of Oceanic Plates. *Science 324*(5926), 499–502.

Lekic, V., and K. M. Fischer 2013. Contrasting lithospheric signatures across the western United States revealed by Sp receiver functions. *Earth and Planetary Science Letters*.

Lekic, V., S. W. French, and K. M. Fischer 2011. Lithospheric thinning beneath rifted regions of Southern California. *Science 334*(6057), 783–787.

McHone, J. G., D. L. Anderson, E. K. Beutel, and Y. A. Fialko 2005. Giant dikes, rifts, flood basalts, and plate tectonics: A contention of mantle models. *Geological Society of America Special Papers* **388**, 401–420.

Morgan, J. 1981. Hotspot tracks and the opening of the Atlantic and Indian oceans. In C. Emiliani (Ed.), *The Oceanic Lithosphere*, Volume 7. of *The Sea.*, pp. 443–487. New York, N.Y.: John Wiley and Sons, Inc.

Morgan, J. 1983. Hotspot tracks and the early rifting of the Atlantic. *Tectonophysics 94*(1-4), 123–139.

Rooney, T. O. 2010. Geochemical evidence of lithospheric thinning in the southern Main Ethiopian Rift. *Lithos 117*(1), 33–48.

Rooney, T. O., I. D. Bastow, and D. Keir 2011. Insights into extensional processes during magma assisted rifting: Evidence from aligned scoria cones. *Journal of Volcanology and Geothermal Research 201*(1-4), 83–96.

Rychert, C. A., J. O. Hammond, N. Harmon, J. M. Kendall, D. Keir, C. Ebinger, I. D. Bastow, A. Ayele, M. Belachew, and G. Stuart 2012. Volcanism in the Afar Rift sustained by decompression melting with minimal plume influence. *Nature Geoscience 5*(6), 406–409.

Rychert, C. A., N. Harmon, and C. Ebinger 2014. Receiver function imaging of lithospheric structure and the onset of melting beneath the Galpagos Archipelago. *Earth and Planetary Science Letters* **388**, 156–165.

Rychert, C. A., G. Laske, N. Harmon, and P. M. Shearer 2013. Seismic imaging of melt in a displaced Hawaiian plume. *Nature Geoscience 6*(8), 657–660.

Rychert, C. A., and P. M. Shearer 2009. A Global View of the Lithosphere-Asthenosphere Boundary. *Science 324*(5926), 495–498.

Schmerr, N. 2012. The Gutenberg Discontinuity: Melt at the Lithosphere-Asthenosphere Boundary. *Science 335*(6075), 1480–1483.

Tan, Y., and D. V. Helmberger 2007. Trans-Pacific upper mantle shear velocity structure. *J. Geophys. Res. 112*(B8).

Yuan, H., and B. Romanowicz 2010. Lithospheric layering in the North American craton. *Nature 466*(7310), 1063–1068.

Contents

List of Tables

List of Figures

Chapter 1 | Implications for Melt Transport and Source Heterogeneity in Upwelling Mantle from the Magnitude of S_p Converted Phases Generated at the Onset of Melting

C. Havlin[1] **and E.M. Parmentier**[1].

1. Department of Earth, Environmental and Planetary Science, Brown University, Providence, RI 02912, USA

Published in its present form in:

Geophysical Research Letters (2014), 41, 5444-5450, doi:10.1002/2014GL060890

1.1 Abstract

Recently detected converted phases in upwelling mantle have been attributed to seismic velocity gradients at the onset of melting. In this study, we investigate conditions required to generate a melting onset phase by combining melt migration models with synthetic receiver functions. We find that increasing upwelling velocity, increasing mantle viscosity, and decreasing water content in the mantle source increases the predicted strength of a melting onset phase. Differences in these parameters between study regions may explain observed variations in converted phase magnitude.

For a wet mantle source, the amplitude of synthetic receiver functions, calculated using a standard relationship for dependence of seismic velocity on melt fraction, is lower than observed amplitudes. One possibility is that the observed receiver functions indicate a heterogeneous mantle source in which wet and dry components melt independently. Alternatively, the dependence of seismic velocity on melt fraction at very low melt fractions may be much stronger than that used here, as suggested in recent studies.

1.2 Introduction

Recent receiver function observations of the upper mantle in the vicinity of proposed mantle plumes detect a rapid increase in seismic velocity with depth attributed to the onset of adiabatic decompression melting in upwelling mantle (Vinnik *et al.*, 2004, 2005; Rychert *et al.*, 2012, 2013, 2014). The proposition is that the transition from subsolidus, melt-free mantle to partially molten mantle with some retained melt is sufficiently sharp for a body wave to generate a measurable converted phase. If the observed converted phases are indeed associated with the onset of melting, then these observations have the potential to further explore melting, melt migration, and the dependence of shear wave velocity on melt at very low melt fraction in upwelling mantle. In this study, we use 1-D melt migration models of the base of the melting zone and a standard dependence of shear wave velocity on melt fraction to generate synthetic S_p receiver functions to compare to the observed converted phases that may arise from the onset of melting.

Receiver function studies of mantle velocity structure beneath the Afar Triple Junction and Gulf of Aden (Vinnik *et al.*, 2004), Iceland (Vinnik *et al.*, 2005), Main Ethiopian Rift (Rychert *et al.*, 2012), Hawaii (Rychert *et al.*, 2013), and Galapagos (Rychert *et al.*, 2014) detect a sharp velocity increase in the depth range of 75–160 km, similar to the depth at which upwelling asthenosphere is expected to cross the dry peridotite solidus. The Main Ethiopian Rift exhibits a converted phase at 75 km beneath the rift, consistent with mid-ocean ridge-like potential temperatures between 1350 and 1400°C (Rychert *et al.*, 2012). Depths of 125 km to 160 km in the Hawaiian, Galapagos, and Afar plumes suggest an excess mantle potential temperature of 1450–1550°C (Rychert *et al.*, 2013, 2014; Vinnik *et al.*, 2004), consistent with estimates of plume excess temperature from transition-zone thinning (e.g. Li *et al.*, 2000; Hooft *et al.*, 2003). Furthermore, in both the Hawaiian and Galapagos plumes, 3-D receiver functions show that the velocity increase deepens below regions with relatively low surface wave velocity, consistent with increased depth of melting in a hotter plume interior (Rychert *et al.*, 2013, 2014).

A similar converted S_p phase is also observed in the western U.S. (Hopper *et al.*, 2014). The authors detect and comment on a rapid velocity increase with depth at depths of 110–150 km beneath the High Lava Plains at the base of a low-velocity zone. Though this observation is not emphasized by Hopper *et al.* (2014) whose main concern was investigating the lithosphere-asthenosphere boundary, the abundance of young (less than 10 Ma) basaltic eruptions in the High Lava Plains (e.g. Jordan *et al.*, 2004) suggests that the converted phase could due to the onset of melting.

In order confirm the validity of interpreting the observed converted phases as melting onset phases (MOPs) and to understand constraints such phases may place on melting and melt migration, we use a 1-D melt migration model (Section 1.3.1) in combination with synthetic S_p receiver functions (Section 1.3.2) to predict how the magnitude of a MOP depends on solid shear viscosity, upwelling rate, source water content, and pyroxenite fraction (Section 1.4).

We find limited conditions that yield shear wave velocity gradients capable of producing a MOP magnitude similar to the detected converted phases. The melt productivity in particular has a large influence on the magnitude of a MOP, and we find that hydrated peridotite with more than $\sim 25 - -50$ ppm dissolved water is unlikely to produce the observed melting onset phases for a prescribed shear wave velocity dependence on melt fraction. Because there is significant water in the mantle source of the Galapagos and Hawaiian plumes, the observed converted phases may indicate a heterogeneous mantle source. Entrainment of a hydrated rim as a dry plume passes through a hydrated transition zone (Bercovici and Karato, 2003) could produce conditions favorable for generation of a strong MOP. Alternatively, a stronger reduction in seismic velocity with the addition of the first small amount of partial melt (e.g Takei and Holtzman, 2009; McCarthy and Takei, 2011) could explain the observed phases.

1.3 Methods

1.3.1 Steady State Melt Fraction Profiles

We generate a suite of melt fraction profiles by finding steady state numerical solutions to the 1-D two-phase system describing a fluid percolating through a viscously deforming matrix (e.g. Ribe, 1985). We assume thermal steady state and so only solve the equations for mass and momentum conservation with a prescribed melt production rate (Ribe, 1985). The solution assumes standard constitutive relationships for permeability k and compaction viscosity ξ: $k=\frac{\phi^3 a^2}{300}$ (Wark and Watson, 1998), where ϕ is melt fraction (porosity), a is grain size, and $\xi=\mu_s^{\circ}\exp(-\alpha\phi)(4/3+\phi^{-1})$ with $\alpha=45$ (Hirth and Kohlstedt, 1995b,a) where μ_s° is the background solid shear viscosity. The form of ξ assumes that bulk viscosity varies inversely with ϕ as suggested by both experimental (Renner *et al.*, 2003) and theoretical (e.g. Simpson *et al.*, 2010) work. The singular nature of the standard form of the compaction viscosity as $\phi \to 0$ suggests that a better understanding of compaction viscosity is required. Grain size is treated as constant, and a=1 cm so ϕ does not exceed ∼1% in order to be consistent with estimates of ϕ from U-series disequilibria (Bourdon *et al.*, 2006). Grain sizes smaller than ∼0.8 cm yield melt fractions over 1% (a=1 mm yields melt fraction in the range of 2–3%). Additional parameters that we treat as constant include fluid viscosity μ_f (1 Pa s) and the solid-fluid density difference $\Delta\rho$ (500 kg m^{-3}).

Melting in the model is treated as steady state adiabatic decompression for which the melting rate is

$$\dot{\Gamma} = V_s \rho_s g \frac{\mathrm{d}F}{\mathrm{d}P}, \tag{1.1}$$

where V_s is solid velocity, ρ_s is solid density, g is gravitational acceleration, F is the amount of melt generated by the mantle source, and $\frac{\mathrm{d}F}{\mathrm{d}P}$ is the melt productivity. In 1-D, the solid velocity is the difference between a background upwelling velocity, V_{up}, and the melt flux, S: $V_s = V_{\mathrm{up}} - S$.

The melt productivity function strongly influences the resulting melt fraction profile and depends on composition, water content, and mantle potential temperature. Because the mantle is hydrated to varying degrees (e.g. Hirschmann, 2010) and may contain as much as ∼25% pyroxenite (Sobolev *et al.*, 2007), melt productivity may vary significantly depending on mantle composition. In Figure 1.1a we plot $\frac{\mathrm{d}F}{\mathrm{d}P}$ along a melting isentrope for anhydrous peridotite (black), hydrous peridotite with 100 ppm (green) and 300 ppm (red) H_2O, and an anhydrous pyroxenite-peridotite mixture with pyroxenite fraction of ϕ_{pyx}=0.2 (blue). For purposes of comparison between model parameters, we fix the melting onset depth (150 km) and use the potential temperature required for melting to begin at that depth, resulting in a potential temperature range of 1426–1518°C. A shallower melting onset depth or lower potential temperature would increase $\frac{\mathrm{d}F}{\mathrm{d}P}$, but this effect will be at least partly balanced by the decrease in total melting column thickness. $\frac{\mathrm{d}F}{\mathrm{d}P}$ was calculated in the same manner as in Section 6.1 of Katz *et al.* (2003) but modified for the peridotite-pyroxenite mixture to account for the cooling of the surrounding matrix from heat absorbed by the deeper pyroxenite melting (Phipps Morgan, 2001). We used the parameterized solidus of Katz *et al.* (2003) for peridotite and the parameterized solidus of Shorttle *et al.* (2014) for pyroxenite. Finally, it is worth noting that generation of a converted phase is sensitive to $\frac{\mathrm{d}F}{\mathrm{d}P}$ at the onset of melting, which may not be well represented by the parameterized solidi. A better understanding of $\frac{\mathrm{d}F}{\mathrm{d}P}$ at low F may improve our ability to interpret the observed converted phases.

The 1-D two-phase system is solved numerically as in Havlin *et al.* (2013) with the addition of the melting rate described above. The boundary condition at the base of the model domain is zero Darcy flux and the boundary condition at z=80km is buoyant flux $S=\frac{k}{\mu_f}\Delta\rho g$. This assumes melt can freely escape the top of the model domain so that we can focus on melting onset without the added complexity of melt accumulation, freezing, and ascent through the lithosphere (e.g. Havlin *et al.*, 2013). The time-dependent system is solved to steady state, as indicated by the decay of $\frac{\partial\phi}{\partial t}$ to numerical precision. We vary the background solid shear viscosity μ_s° between 10^{18} and 10^{21} Pa s, background upwelling velocity V_{up} between 5 and 40 cm yr^{-1}, peridotite water content from 0−300 ppm and pyroxenite fractions of 0, 0.2, and 0.4, which covers the likely range for mantle plumes and fast spreading ridges.

A representative set of steady state melt fraction profiles is shown in Figure 1.1b to illustrate the dependence of the steady state melt fraction on μ_s° and $\frac{\mathrm{d}F}{\mathrm{d}P}$. The lower productivity of wet melting results in lower melt fraction but also smaller melt fraction gradient at the onset of melting (green, red) compared to anhydrous peridotite (black). As μ_s° increases, the compaction length increases and the melt fraction profile mimics the productivity curve more closely (dashed black). The pyroxenite-peridotite mixture produces a small kink in melt fraction at the onset of peridotite melting (blue).

1.3.2 Synthetic Receiver Functions and Data

To calculate synthetic S_p receiver functions, we use the steady state melt fraction calculated for a given set of melt migration parameters to calculate a velocity perturbation. The velocity perturbation is added to a 1-D velocity profile from which we generate synthetic S_p receiver functions. While seismic velocity depends on additional thermodynamic variables, gradients in temperature, pressure and dehydration in upwelling mantle are significantly less than gradients in melt fraction. To first order, considering velocity perturbations solely due to melt fraction is sufficient in studying the generation of melting onset phases.

Shear wave velocity perturbations from melt are calculated using the dependence from Hammond and Humphreys (2000) for relaxed, organized cuspate geometry (7.9% decrease in S-wave velocity for 1% melt). While we use a simple relationship between seismic velocity and melt fraction, different melt geometries (Schmeling, 1985) and anelastic effects (e.g. McCarthy and Takei, 2011) could strongly influence MOP generation. Using a smaller shear wave reduction (e.g. <3% per percent melt) decreases the synthetic MOP magnitude considerably. The velocity decrease due to melt is added to a two layer model composed of a 20 km thick crust with 6.8 km/s and 3.9 km/s P and S wave velocities and a mantle half-space with 8.2 km/s and 4.55 km/s P and S wave velocities (gray dashed curve, figure 1.2a). Here, the base of the lithosphere is placed at 80 km to minimize potential interference between the resulting negative phase and the Moho or MOPs. The resulting 1-D velocity profile is discretized into a finite number of layers and used to generate synthetic waveforms in the same manner as previous studies (e.g. Rychert *et al.*, 2007; Ford *et al.*, 2010; Rychert *et al.*, 2012). Synthetic seismograms were generated using a propagator matrix method (Kikuchi and Kanamori, 1982) for a parent S wave with a 10 s dominant period. The synthetics were then deconvolved for S_p receiver functions with the extended-time multitaper method (Helffrich, 2006) using a band-pass filter of 0.03 to 0.5 Hz before deconvolution. For each input velocity profile, the final S_p receiver function is a stack of ~40 waveforms from fictitious sources within a range of epicentral distances (55-80) and depths (1-300 km). A typical set of synthetic S_p receiver functions are shown in Figure 1.2 for the same parameters in Figure 1.1. A clear MOP is visible at a depth of 150 km.

The amplitude of S_p receiver functions is frequently reported in the literature as the fraction of incident S-wave energy, but comparing absolute magnitudes of phases between studies can be misleading due to differences in methods and implementation. Rather than compare absolute magnitudes, we compare the ratio of MOP magnitude to Moho magnitude because a given velocity structure should produce phases that have the same relative magnitude regardless of processing method. The sensitivity of our result to both the applied filter band as well as crustal velocity structure is described further in the supporting information. The magnitude of the normalized MOP is plotted in Figures 1.3a and 1.3b for a range of water content, background viscosity μ_s°, upwelling rate V_{up}, and pyroxenite fraction ϕ_{pyx}. These results are discussed in Section 1.4.

To compare the predicted MOP/Moho values to observations, we calculate a MOP/Moho magnitude for the Main Ethiopian Rift (MER), High Lava Plains (HLP), and Galapagos using the mean values from reported receiver functions. The Galapagos MOP/Moho value of 0.33 was calculated using the mean values of the 1-D data in Figure 3 of Rychert *et al.* (2014) and the MER MOP/Moho value of 0.20 was calculated using the 1-D data in Figure 2 of Rychert *et al.* (2012). The potential MOP observed beneath the MER is much shallower than the depth considered here and is likely affected by interference with a negative sidelobe from the Moho (Rychert *et al.*, 2012). We therefore view the mean value for the MER as a minimum. For the HLP, we calculate a proposed MOP/Moho magnitude of 0.21 found by taking the average of the positive phase between 100 and 150 km and Moho phases identified in figure 6a of Hopper *et al.* (2014) (Hopper *et al.*, 2014, E. Hopper and K. Fischer, Personal Communications 2014). Despite a well-resolved potential MOP in Hawaii, the Moho is not well constrained by Rychert *et al.* (2013) (e.g., supplemental Figure S2 of Rychert *et al.* (2013)). Because of this ambiguity, we do not calculate a MOP/Moho value for Hawaii.

Mean values of possible MOP/Moho magnitudes are plotted as black squares in Figure 1.3c. The Moho normalization removes some but not all of the dependence on the filtering applied to the data, so in Figure 1.3c we indicate the possible variation that could arise from filtering effects with arrows (see supporting information). Considering the standard deviation for each of these data points, the range for proposed MOP/Moho for each location is 0.13–0.78, 0.1–0.5 and 0.03–0.70 for the Galapagos, High Lava Plains, and Main Ethiopian Rift, respectively.

1.4 Results and Discussion

The calculated magnitude of a melting onset phase (MOP) is significantly larger for a dry, high viscosity mantle compared to a hydrated or low viscosity mantle (Figure 1.3). As water in the source increases, the productivity and resulting retained melt fraction drops, significantly decreasing MOP magnitude. As solid shear viscosity increases (Figure 1.3b), the solid matrix becomes more difficult to compact and the retained melt fraction mimics the melt productivity (i.e., $\frac{\mathrm{d}\phi}{\mathrm{d}z} \rightarrow \frac{\mathrm{d}F}{\mathrm{d}z}$). As a result, MOP magnitude is more sensitive to changes in melt productivity and upwelling velocity for a high mantle viscosity. Melting rate is directly proportional to upwelling velocity, so higher upwelling velocity results in larger MOP magnitude.

Our modeling implies that a melting onset phase magnitude should vary between tectonic settings. Full spreading rates at mid-ocean ridges range from 0.2 to 15 cm yr^{-1} (Dick *et al.*, 2003). For idealized isoviscous corner flow, a full spreading rate of 15-16 cm yr^{-1} results in an upwelling rate of $\sim$5 cm/yr (Turcotte and Schubert, 2002) so the MOP magnitude predicted for the 5 cm/yr case (Figure 1.3a, blue) is an upper limit for ridges. As a result, MOPs should be easier to observe in mantle plumes with significantly larger upwelling velocities. Consistent with the conclusion that conditions beneath the Main Ethiopian Rift may be more similar to a ridge than a plume (Rychert *et al.*, 2012), the Main Ethiopian Rift exhibits a MOP/Moho value that could be achieved with upwelling velocity $<$ 20 cm yr^{-1} and viscosity $\geq 10^{19}$ Pa s. A stronger upwelling velocity may explain the larger mean MOP/Moho value beneath the Galapagos compared to the Main Ethiopian Rift.

The possible MOPs observed in the Main Ethiopian Rift (Rychert *et al.*, 2012), High Lava Plains (Hopper *et al.*, 2014), and Galapagos (Rychert *et al.*, 2014) exhibit mean MOP/Moho values consistent with melting of relatively dry peridotite. While a variety of combinations of viscosity and upwelling rate (e.g., viscosity $\sim 10^{19}$ Pa s, upwelling rates greater than $\sim$20 cm yr^{-1}) can produce MOP/Moho magnitudes of greater than 0.2, water content greater than $\sim 25 - 50$ ppm results in magnitudes smaller than the observed mean values (Figure 1.3c). Though we could not calculate a mean MOP/Moho magnitude for Hawaii (Section 1.3.2), the proposed melting onset phase in Hawaii is strong and well resolved, with an absolute magnitude greater than that in the Galapagos. Therefore, we expect Hawaii to be similar to the Galapagos.

Studies of volatiles in ocean island basalts report mantle source water concentrations of 300–900 ppm H_2O (Hirschmann, 2010, and references therein). One way to explain both the strength of the observed converted phase and the measured water content is a heterogeneous mantle source. Hydrogen diffusivity in the mantle is relatively fast ($D \approx 10^{-7}$ m^{2}s^{-1} (Mackwell and Kohlstedt, 1990)) so that heterogeneity in water content would not be preserved in a fine (subkilometer) scale plum-pudding mixture, but a relatively dry plume passing through a hydrated transition zone could develop a hydrated outer rim as entrained water diffuses toward the plume interior (Bercovici and Karato, 2003). Hydrogen diffusivity in the transition zone may be a much as $\sim$1000 times greater than in the upper mantle (Bercovici and Karato, 2003), so that the characteristic diffusion distance for a plume upwelling at 40 cm yr^{-1} through a 250 km thick transition zone is $\sim$1 to $\sim$40 km ($\sqrt{Dt}$ for $10^{-7} \leq D \leq 10^{-4}$ m^{2}s^{-1}). These estimates indicate that an initially dry plume of radius 100 km would retain a dry inner core after passing through the transition zone.

In the Hawaiian and Galapagos plume there may be additional heterogeneity in mantle source composition. The source for oceanic island basalts may contain a significant fraction of pyroxenite, with estimates of $\sim$25% pyroxenite in the Hawaiian plume source (Sobolev *et al.*, 2007). A pyroxenite fraction of 20% decreases MOP magnitude (Figure 1.3a) due to the lower bulk productivity (Figure 1.1a) but a larger component of pyroxenite drives MOP magnitude upward again (Figure 1.3a).

Alternatively, it is possible that a stronger reduction of seismic velocity with small amounts of melt may generate velocity gradients capable of producing the observed MOPs without invoking dry melting. Rapid variation in solid viscosity (e.g Takei and Holtzman, 2009; McCarthy and Takei, 2011) and/or dihedral angle (Yoshino *et al.*, 2007) with the addition of the small amount of partial melt could further decrease shear wave velocity at melting onset.

1.5 Conclusions

We have used 1-D numerical solutions of melting and melt transport together with synthetic S_p receiver functions to investigate the conditions required for the generation of observed converted phases in regions of mantle upwelling. We find that the variation in melt fraction in the vicinity of melting onset is sufficiently sharp to generate converted seismic phases for a range of upwelling velocity, solid shear viscosity, and water content. Stronger converted phases are generated for higher upwelling velocity or higher mantle viscosity. Increasing upwelling velocity may explain the apparent increase in melting onset phase strength between the Main Ethiopian Rift, Galapagos, and Hawaii.

The calculated magnitude of converted phases decreases significantly as water content increases. While erupted melt compositions contain significant water at oceanic islands where melting onset phases have been proposed, entrainment of a water-rich component as a relatively dry plume passes through a hydrated transition zone could provide the observed water while maintaining a relatively dry plume interior capable of producing the observed melting onset phases. Alternatively, a stronger dependence of seismic velocity on melt fraction at very low melt fraction could provide additional velocity change.

1.6 Acknowledgments

We thank (1) E. Hopper and K. Fischer for use of their synthetic receiver function code and for sharing their seismic expertise, (2) G. Hirth and Y. Liang for useful discussion, and (3) J. Armitage and an anonymous reviewer for helpful comments. Data used to generate Figure 1.3c are available in publications cited in Section 1.3.2. This work was supported by NSF grant OCE1156706.

1.7 Supplemental Material

1.7.1 Filter Band Sensitivity

Comparing absolute magnitudes of converted phases between studies can be difficult because the converted phase magnitude depends on the filtering applied to data during processing. The relative amplitude of phases, however, should be less sensitive to the filtering and so we normalized the melting onset phase (MOP) magnitude by the Moho magnitude in order to compare to studies that filter the data at different frequency ranges. In this section, we verify the usefulness of the Moho normalization by showing a subset of MOP magnitude calculations repeated for different filter ranges. In the following section, we comment on the expected variation in MOP/Moho values for different crustal structures.

To further explore the MOP/Moho normalization, we use the input velocity model from a subset of the melt migration runs for a shear viscosity of 10^{19} Pa s, upwelling velocity of 20 cm yr^{-1} and water content increasing from 0 to 300 PPM. In figure 1.4a, we plot the absolute magnitude of the MOP (i.e., the energy of the phase relative to the parent S wave) for a range of frequencies. In figure 1.4b, we plot the MOP normalized by the Moho for the same range of frequencies. Comparing the two plots, it is clear that normalizing by the Moho reduces some of the variation in MOP amplitude, particularly at low water content.

In general, the upper corner of the bandpass filter applied during receiver function processing has the greatest impact on the character of the phases and interference between phases. This is apparent in figure 1.4b; changes to the lower corner frequency result in minimal changes in MOP/Moho amplitudes (compare red, magenta and dashed black curves) while decreasing the value of the upper corner reduces the sensitivity to short lengthscale velocity variations so that the sensitivity to increasing water content changes (compare red, green and blue curves).

While the dependence of the MOP/Moho on increasing water content is somewhat sensitive to the frequency range, the variations due to changing the filter band are relatively small so that it is reasonable to compare MOP/Moho values from data filtered at different frequencies. Figure 1.4 shows the resulting MOP/Moho value for filter band used in this study (red curve), the High Lava Plains study (green curve, HLP) and the Main Ethiopian Rift (cyan curve, MER). These curves are similar enough that variations in MOP/Moho arising from filtering are not large enough to significantly affect our conclusions.

As a final note on filters, using a very narrow filter in calculating synthetic receiver functions can result in unstable behavior. Our synthetics use a single, prescribed dominant period, so that the synthetic signal is susceptible to over-filtering; when we use the very narrow filter 0.05-0.14 Hz used in the studies of the Galapagos and Hawaii (Rychert *et al.*, 2014, 2013), too much of the signal is filtered, resulting in harmonic ringing due to phase interference and significant shifts in the depth location of phase peaks. While we cannot use 0.05-0.14 Hz, varying the upper and lower corner frequencies separately results in similar MOP/Moho values so that it is reasonable to compare the MOP/Moho value from the Galapagos.

1.7.2 Moho Sensitivity

While normalizing the melting onset phase (MOP) magnitude to the Moho magnitude removes some of the dependence on the frequency filter, it introduces a dependence on local crustal velocity structure. Because the crustal velocity structure and hence Moho amplitude varies between the study regions considered here, we experimented with using increasingly complex crustal structures while keeping the mantle velocity structure fixed.

Figure 1.5 shows the input velocity structure and resulting receiver functions for 4 crustal structures: (1) the crustal structure used in this study which is based off that of Rychert *et al.* (2013), (2) same as (1) but with an extra velocity step, and two cases (3 and 4) based on the crustal structure reported in Leahy *et al.* (2010). Table 1.1 shows the MOP/Moho value of for each crustal structure relative to MOP/Moho calculated with crust (1). These calculations suggest that the MOP/Moho value may vary between a factor of 0.86-1.31 due to variations in the Moho.

1.8 References

Bercovici, D., and S.-i. Karato 2003. Whole-mantle convection and the transition-zone water filter. *Nature 425*(6953), 39–44.

Bourdon, B., N. Ribe, A. Stracke, A. Saal, and S. Turner 2006. Insights into the dynamics of mantle plumes from uranium-series geochemistry. *Nature 444*(7120).

Dick, H. J. B., J. Lin, and H. Schouten 2003. An ultraslow-spreading class of ocean ridge. *Nature 426*(6965), 405–412.

Ford, H. A., K. M. Fischer, D. L. Abt, C. A. Rychert, and L. T. Elkins-Tanton 2010. The lithosphere-asthenosphere boundary and cratonic lithospheric layering beneath Australia from Sp wave imaging. *Earth and Planetary Science Letters 300*(3-4), 299–310.

Hammond, W. C., and E. D. Humphreys 2000. Upper mantle seismic wave velocity: Effects of realistic partial melt geometries. *J. Geophys. Res. 105*(B5), 10975–10986.

Havlin, C., E. Parmentier, and G. Hirth 2013. Dike propagation driven by melt accumulation at the lithosphere-asthenosphere boundary. *Earth and Planetary Science Letters* **376**, 20–28.

Helffrich, G. 2006. Extended-time multitaper frequency domain cross-correlation receiver-function estimation. *Bulletin of the Seismological Society of America 96*(1), 344–347.

Hirschmann, M. M. 2010. Partial melt in the oceanic low velocity zone. *Physics of the Earth and Planetary Interiors 179*(1-2), 60–71.

Hirth, G., and D. L. Kohlstedt 1995a. Experimental constraints on the dynamics of the partially molten upper mantle 2. Deformation in the dislocation creep regime. *J. geophys. Res 100*(8), 15441–15052.

Hirth, G., and D. L. Kohlstedt 1995b. Experimental constraints on the dynamics of the partially molten upper mantle: Deformation in the diffusion creep regime. *Journal of Geophysical Research 100*(B2), 1981–2001.

Hooft, E. E., D. R. Toomey, and S. C. Solomon 2003. Anomalously thin transition zone beneath the Galpagos hotspot. *Earth and Planetary Science Letters 216*(1), 55–64.

Hopper, E., H. A. Ford, K. M. Fischer, V. Lekic, and M. J. Fouch 2014. The lithosphere–asthenosphere boundary and the tectonic and magmatic history of the northwestern United States. *Earth and Planetary Science Letters*.

Jordan, B. T., A. L. Grunder, R. A. Duncan, and A. L. Deino 2004. Geochronology of age–progressive volcanism of the Oregon High Lava Plains: Implications for the plume interpretation of Yellowstone. *Journal of Geophysical Research 109*(B10).

Katz, R. F., M. Spiegelman, and C. H. Langmuir 2003. A new parameterization of hydrous mantle melting. *Geochemistry, Geophysics, Geosystems 4*(9).

Kikuchi, M., and H. Kanamori 1982. Inversion of complex body waves. *Bulletin of the Seismological Society of America 72*(2), 491–506.

Leahy, G. M., J. A. Collins, C. J. Wolfe, G. Laske, and S. C. Solomon 2010. Underplating of the Hawaiian Swell: evidence from teleseismic receiver functions. *Geophysical Journal International 183*(1), 313–329.

Li, X., R. Kind, K. Priestley, S. Sobolev, F. Tilmann, X. Yuan, and M. Weber 2000. Mapping the Hawaiian plume conduit with converted seismic waves. *Nature 405*(6789), 938–941.

Mackwell, S. J., and D. L. Kohlstedt 1990. Diffusion of hydrogen in olivine: implications for water in the mantle. *Journal of Geophysical Research 95*(B4), 5079–5088.

McCarthy, C., and Y. Takei 2011. Anelasticity and viscosity of partially molten rock analogue: Toward seismic detection of small quantities of melt. *Geophysical Research Letters 38*(L18306).

Phipps Morgan, J. 2001. Thermodynamics of pressure release melting of a veined plum pudding mantle. *Geochemistry, Geophysics, Geosystems 2*(4).

Renner, J., K. Viskupic, G. Hirth, and B. Evans 2003. Melt extraction from partially molten peridotites. *Geochem. Geophys. Geosyst. 4*(5).

Ribe, N. M. 1985. The generation and composition of partial melts in the earth's mantle. *Earth and planetary science letters 73*(2), 361–376.

Rychert, C. A., J. O. Hammond, N. Harmon, J. M. Kendall, D. Keir, C. Ebinger, I. D. Bastow, A. Ayele, M. Belachew, and G. Stuart 2012. Volcanism in the Afar Rift sustained by decompression melting with minimal plume influence. *Nature Geoscience 5*(6), 406–409.

Rychert, C. A., N. Harmon, and C. Ebinger 2014. Receiver function imaging of lithospheric structure and the onset of melting beneath the Galpagos Archipelago. *Earth and Planetary Science Letters* **388**, 156–165.

Rychert, C. A., G. Laske, N. Harmon, and P. M. Shearer 2013. Seismic imaging of melt in a displaced Hawaiian plume. *Nature Geoscience 6*(8), 657–660.

Rychert, C. A., S. Rondenay, and K. M. Fischer 2007. P-to-S and S-to-P imaging of a sharp lithosphere-asthenosphere boundary beneath eastern North America. *J. Geophys. Res. 112*(B8).

Schmeling, H. 1985. Numerical models on the influence of partial melt on elastic, anelastic and electric properties of rocks. Part I: elasticity and anelasticity. *Physics of the earth and planetary interiors 41*(1), 34–57.

Shorttle, O., J. Maclennan, and S. Lambart 2014. Quantifying lithological variability in the mantle. *Earth and Planetary Science Letters* **395**, 24–40.

Simpson, G., M. Spiegelman, and M. I. Weinstein 2010. A multiscale model of partial melts: 2. Numerical results. *J. Geophys. Res. 115*(B4).

Sobolev, A. V., A. W. Hofmann, D. V. Kuzmin, G. M. Yaxley, N. T. Arndt, S.-L. Chung, L. V. Danyushevsky, T. Elliott, F. A. Frey, and M. O. Garcia 2007. The amount of recycled crust in sources of mantle-derived melts. *Science 316*(5823), 412–417.

Takei, Y., and B. K. Holtzman 2009. Viscous constitutive relations of solidliquid composites in terms of grain boundary contiguity: 2. Compositional model for small melt fractions. *Journal of Geophysical Research 114*(B6).

Turcotte, D., and G. Schubert 2002. *Geodynamics* (2 ed.). New York, N.Y.: Cambridge University Press.

Vinnik, L., V. Farra, and R. Kind 2004. Deep structure of the AfroArabian hotspot by S receiver functions. *Geophysical Research Letters 31*(11).

Vinnik, L., G. Foulger, and Z. Du 2005. Seismic boundaries in the mantle beneath Iceland: a new constraint on temperature. *Geophysical Journal International 160*(2), 533–538.

Wark, D. A., and E. B. Watson 1998. Grain-scale permeabilities of texturally equilibrated, monomineralic rocks. *Earth and Planetary Science Letters 164*(3-4), 591–605.

Yoshino, T., Y. Nishihara, and S.-i. Karato 2007. Complete wetting of olivine grain boundaries by a hydrous melt near the mantle transition zone. *Earth and Planetary Science Letters 256*(3), 466–472.

1.9 Figures

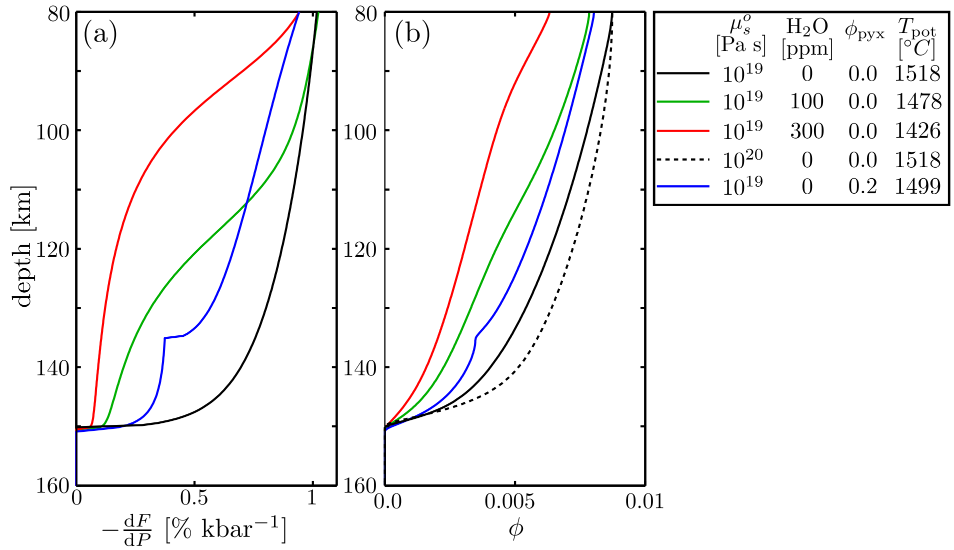

Figure 1.1: (a) Melt productivity functions for isentropic melting and (b) steady state melt fraction profiles for representative values of background solid viscosity μ_s°, peridotite water fraction and pyroxenite fraction $\phi_{\rm pyx}$. Melting onset depth was fixed at 150 km, which corresponds to mantle potential temperatures shown in the legend.

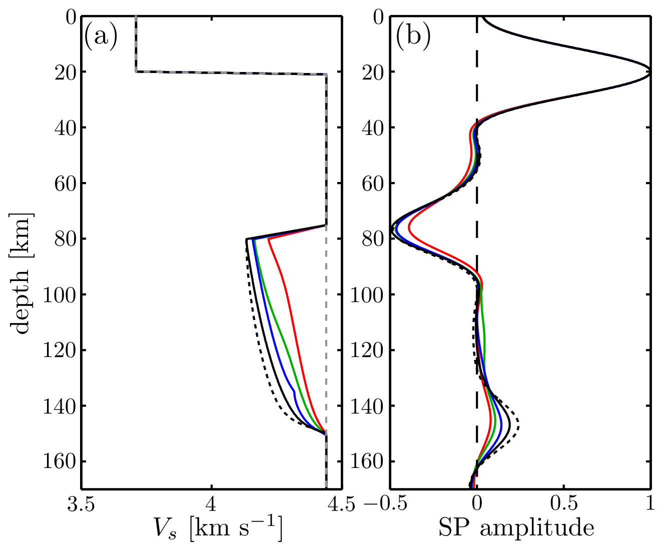

Figure 1.2: (a) Input shear wave velocities and background velocity structure (dashed gray) and (b) resulting S_p receiver function amplitude for the same parameters as in figure 1.

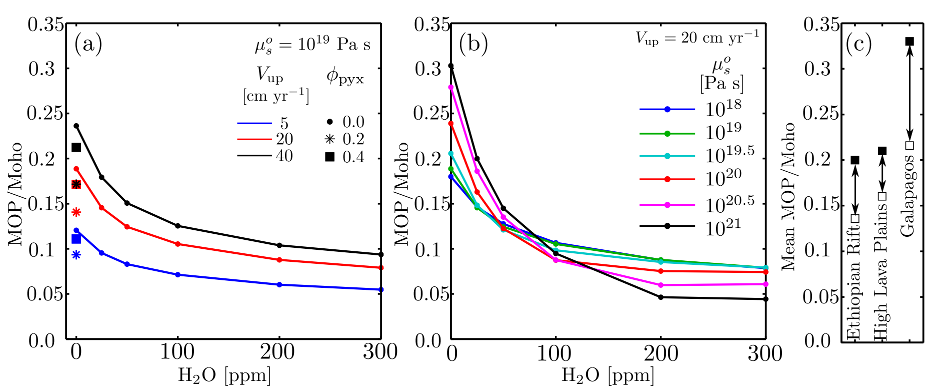

Figure 1.3: (a) Magnitude of melting onset phase (MOP) normalized by Moho magnitude as a function of water, upwelling velocity and pyroxenite fraction, (b) MOP/Moho dependence on solid shear viscosity and water and (c) observed mean values of potential MOPs.

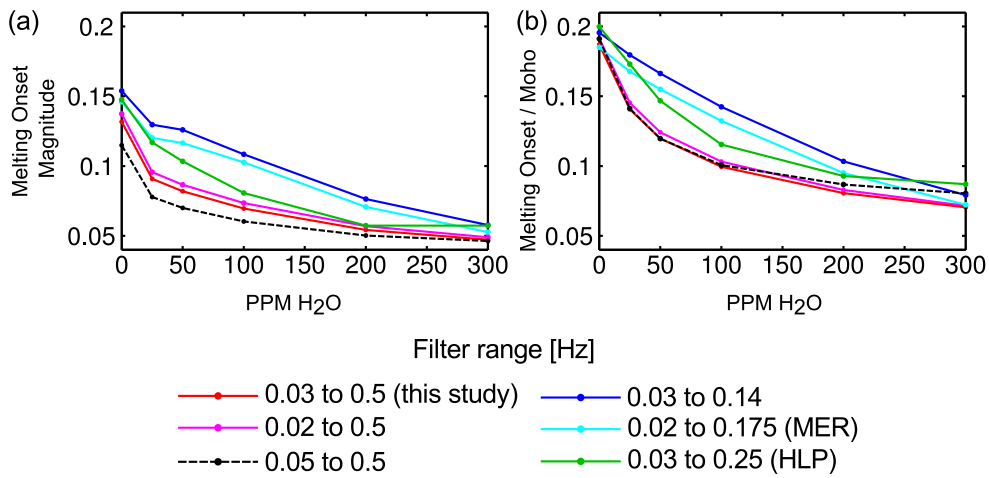

Figure 1.4: (a) absolute magnitude of melting onset phase relative to parent S wave and (b) melting onset phase magnitude normalized by the Moho magnitude. This study used 0.03 to 0.5 Hz (red line) while studies of the Main Ethiopian Rift (MER Rychert *et al.*, 2012), High Lava Plains (HLP Hopper *et al.*, 2014), Galapagos (Rychert *et al.*, 2014) and Hawaii (Rychert *et al.*, 2013) used filters of 0.02 to 0.175 Hz, 0.03 to 0.25 Hz, 0.05 to 0.14 Hz and 0.05 to 0.14 Hz, respectively.

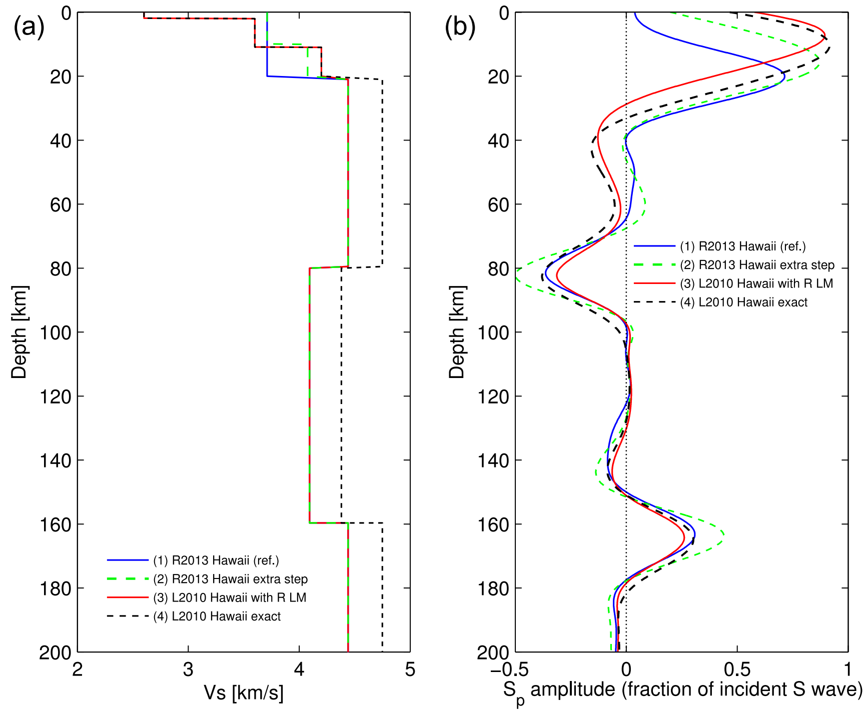

Figure 1.5: (a) input velocity models for a range of crustal structures and (b) resulting receiver functions

Crustal structure:	(1)	(2)	(3)	(4)
Relative MOP/Moho:	1	0.86	1.48	1.31

Table 1.1: Sensitivity of normalized melting onset phase to Moho. Crustal structures refer to the crustal velocity structures used in Figure 1.2. Sensitivity is reported relative to crustal structure 1, the velocity structure used in this study (i.e., the normalized MOP/Moho using crustal structure 2 is a factor of 0.86 times the MOP/Moho using crustal structure 1.

Chapter 2 | Dike Propagation Driven by Melt Accumulation at the Lithosphere-Asthenosphere Boundary

C. Havlin[1], E.M. Parmentier[1], and G. Hirth[1].

1. Department of Earth, Environmental and Planetary Science, Brown University, Providence, RI 02912, USA

Published in its present form in:

Earth and Planetary Science Letters (2013), 376, 20-28, doi:10.1016/j.epsl.2013.06.010

2.1 Abstract

This study examines the combined effects of melt migration by porous flow in the asthenosphere and dike propagation in the lithosphere. Melt collecting at the base of the lithosphere forms a decompacting boundary layer (DBL), in which the overpressure is sufficient to nucleate dikes that propagate buoyantly upward into the lithosphere. The asthenosphere melt flux determines the excess pressure and melt accumulation rate in the DBL, which together with the state of lithospheric stress, control dike growth rate, dike recurrence interval and the height to which dikes propagate. The vertical propagation and subsequent freezing of melt filled dikes heats and thins the lithosphere.

Our model couples fundamental aspects of dike propagation and porous flow that are commonly treated separately. Our model allows us to estimate conditions under which vertically propagating dikes can thin the lithosphere, given a melt flux determined by the rate of melt production in the asthenosphere. The model also provides an estimate of the amount of melt present at the base of the lithosphere. We find that a steady state high-porosity boundary layer at the lithosphere-asthenosphere boundary, with a melt fraction about 2.5-4 times higher than the asthenosphere melt fraction. Diking occurs at melt fractions much less than the disaggregation limit, so dikes are only a few km tall and about 1 cm wide. Though dikes are small, their recurrence on the order of days can lead to lithosphere erosion rates on the order of a few km/Myr with a melt fraction of a few percent at the base of the lithosphere. The steady state boundary layer melt fraction is controlled by differences in lithospheric stress state and or asthenosphere melt flux, indicating that seismic discontinuities associated with melt accumulation at the lithosphere-asthenosphere boundary should vary systematically with variations in asthenosphere melt generation and tectonic setting.

2.2 Introduction

2.2.1 Motivation and Background

The near global observation of a sharp drop in seismic velocity near the base of the lithosphere (e.g. Gaherty *et al.*, 1996; Tan and Helmberger, 2007; Rychert and Shearer, 2009; Yuan and Romanowicz, 2010; Fischer *et al.*, 2010) has been attributed in some locations to melt accumulating beneath a solidus isotherm (e.g. Kawakatsu *et al.*, 2009; Schmerr, 2012). Accumulation of melt at the lithosphere-asthenosphere boundary (LAB) has important consequences for the transport of melt into the lithosphere by diking, a significant factor in creation of divergent plate boundaries (e.g. Buck, 2004; Bialas *et al.*, 2010). In this study, we focus on vertical dike propagation from a melt-rich boundary layer at the LAB. We synthesize the results of previous studies on melt migration in the asthenosphere and buoyant dike propagation in the lithosphere in a coupled model that captures the important physical characteristics of both porous flow and dike propagation. Our new approach allows us to quantify the melt flux and heat flux into the lithosphere, as well as the stability of melt at the LAB.

The melt flux into the lithosphere via diking controls tectonic behavior at mid-ocean ridges (MORs) and active continental rifts where continental margins are created. Dike propagation accommodates extension (Buck *et al.*, 2005; Tucholke *et al.*, 2008) and provides heat that weakens the lithosphere by increasing the fraction of the lithosphere deforming by ductile creep (Royden *et al.*, 1980; Bialas *et al.*, 2010), resulting in differences between regions of magma rich and magma poor extension. Magma rich margins, for example, display narrow zones of localized extension with little detachment faulting (White *et al.*, 1987; Menzies *et al.*, 2002) while amagmatic margins are characterized by deep extensional basins formed by diffuse normal faulting (Whitmarsh *et al.*, 2001; Cochran, 1983). The supply of melt is tied to production of melt in the asthenosphere, evident in the correlation of rifting location with continental flood basalt eruption and plume head arrival (Morgan, 1971, 1983).

The melt distribution below the lithosphere, which determines the source volume for diking, is constrained by seismic studies. Average melt fractions in upwelling mantle beneath a mid-ocean ridge are between 10^{-4} and 0.02 (Forsyth, 1998; Evans *et al.*, 1999), but may increase on length scales shorter than the resolution of seismic tomography and magnetotelluric inversion. The sharp drop in seismic velocity at depths consistent with the base of the oceanic and Phanerozoic continental lithosphere, may in some locations be due to the accumulation of melt at a permeability or freezing boundary (e.g. Rychert *et al.*, 2005; Kawakatsu *et al.*, 2009; Fischer *et al.*, 2010). Beneath Hawaii, where melt is generated by a mantle plume, the similarity in discontinuity depth (~75 km, Rychert and Shearer (2011); Schmerr (2012)), and the maximum depth of dike-associated seismicity (~60 km, Wright and Klein (2006)), suggests that dikes propagate upwards from these zones of melt accumulation, which may contribute to the local thinning of the lithosphere above the Hawaiian plume as observed by Li *et al.* (2004).

Despite the relationship between lithosphere dike propagation and asthenosphere porous flow, most studies treat the two regimes independently. Studies on melt migration in the asthenosphere typically assume that melt generated beneath the lithosphere or a ridge axis is extracted from the asthenosphere, forming new crust. Some studies use a partial coupling by assuming a critical melt fraction above which melt is removed (Ghods and Arkani Hamed, 2000), by imposing a narrow window through which melt can escape (Katz, 2008) or by applying a suction due to an existing buoyantly pressurized dike (Katz, 2010). In contrast, fracture mechanics models of dike propagation assume a constant fluid flux (Spence and Turcotte, 1985) or constant fluid excess pressure (Lister and Kerr, 1991) at the base of an upwardly propagating dike. Studies that focus on the effect of melt emplacement on tectonics

(Tucholke *et al.*, 2008; Bialas *et al.*, 2010) treat the supply of melt at the base of the lithosphere as an adjustable parameter.

2.2.2 Conceptual Model

The degree to which melt remains stable at the top of the asthenosphere or penetrates the lithosphere, subsequently affecting lithosphere strength and structure, is a function of melt availability, tectonic environment, and the ability for melt to migrate without freezing. To investigate the coupling among these variables, we synthesize results from earlier studies to develop a coupled model of melt migration from source to surface. These processes are illustrated schematically in Figure 2.1.

Melt generated by adiabatic decompression in the mantle rises buoyantly. When melt collects at a freezing boundary (Figure 2.1b), the solid matrix decompacts to accommodate the additional melt. If the pressure difference between fluid and solid (excess pressure, P) is large enough, dikes will propagate from the decompacting boundary layer (DBL) into the lithosphere. Dike growth (Figure 2.1c) is limited by the rate at which fluid flows into the dike from the source region as well as the flux of melt into the DBL from below.

The porosity, ϕ, of a DBL when dike propagation begins controls the kinetics of dike growth. If dike propagation begins after ϕ increases to the rheologically critical melt fraction ($\phi_{RCMF} \approx 0.25$, Scott and Kohlstedt (2006)), where solid grains lose contact, dike growth is controlled by the combination of magma buoyancy, source excess pressure and viscous pressure gradients due to flow (e.g. Lister, 1990; Roper and Lister, 2005). If dikes propagate when $\phi < \phi_{RCMF}$, pressure gradients due to compressibility drive melt flow and dike growth is limited by ϕ in the DBL at dike initiation (e.g. Sleep, 1988; Fowler and Scott, 1996; Rubin, 1998). As dikes propagate into the lithosphere, they draw melt from near their bases, so adjacent dikes compete for melt.

The distance a dike propagates upwards depends on the thermal state of the lithosphere (Figure 2.1d). The freezing rate of a dike depends primarily on the horizontal temperature gradient between the dike and host rock at each height in the dike. Magma flowing into a dike from just beneath a freezing boundary remains at a temperature close to its solidus. Thus, near the bottom of a dike the freezing rate is negligible. Higher up, the host rock temperature decreases so freezing rates increase as a dike grows in height. Different geotherms result in different freezing rates at a fixed height above the base of the lithosphere. The height to which dikes rise before freezing depends on the rate of mechanical opening relative to thermal closure.

In the following section we describe the theoretical formulation and coupling between magma accumulation and dike propagation. As both processes have been studied extensively on their own, we employ simplified models that capture the basic physics and allow us to focus on understanding the feedbacks involved in their coupling. The processes incorporated in the model are (1) magma accumulation by porous flow through a viscous matrix, (2) elastic dike propagation from a (3) poroelastic source region and (4) freezing of dike walls. After considering the behavior of a single dike, we consider the evolution of a decompacting boundary layer subject to a time-averaged dike flux.

The important results of this study are (1) the excess pressure in zones of melt accumulation initiates dike propagation before before solid grains disaggregate. (2) Dikes propagating upward into the lithosphere are $\sim$1 cm wide and freeze when a few km tall and (3) the melt flux out of the asthenosphere due to successive emplacement of dikes should evolve to balance the melt flux into the melt accumulation zone, resulting in a steady state with elevated melt fraction in a boundary layer at the LAB. These results indicate that thermal erosion of homogeneous lithosphere proceeds by dike-induced heating of only a few km above the LAB. Furthermore, a high melt fraction boundary layer at the LAB can be a relatively stable feature, though the magnitude of any seismic discontinuity associated with it should vary with tectonic setting.

2.3 Methods

2.3.1 Magma Accumulation

To calculate the initial porosity and excess pressure available for diking at the LAB, we treat the asthenosphere as a viscously deforming two-phase medium. The system of equations describing two-phase magma migration in the asthenosphere have been studied extensively (e.g. McKenzie, 1984; Scott and Stevenson, 1984; Fowler, 1985; Bercovici *et al.*, 2001), thus we present them here in a supplemental appendix. We solve for the excess pressure, P, in one dimension assuming a porosity-dependent permeability, $k{=}\frac{a^2\phi^3}{300}$ (Wark and Watson, 1998) where a is grain size (a=1 cm throughout). Additionally, we use a compaction viscosity of the form $\xi = \eta\phi^{-1}$ where η is the solid shear viscosity (Renner *et al.*, 2003; Bercovici *et al.*, 2001; Simpson *et al.*, 2010). The system of equations is discretized with a finite volume formulation and solved via a direct solver.

Our model domain is restricted to the top of an idealized melting column. We impose an impermeable boundary condition at z=0 by setting the Darcy flux to 0, which requires the vertical derivative of P to balance the melt buoyancy. We consider the case of broad, distributed melting and assume that melt flow into the model domain is due to a steady state buoyant melt flux in which the porosity is a constant, ϕ_o, and P=0. Chemical heterogeneities (e.g. Katz and Weatherley, 2012) as well as chemical and mechanical instabilities (e.g. Daines and Kohlstedt, 1994; Aharonov *et al.*, 1995; Stevenson, 1989; Holtzman *et al.*, 2003) may result in a more complicated view of magma migration in the asthenosphere, but attempting to include these processes introduces complexity that masks the basic physics involved in the coupling of asthenospheric magma migration to dike propagation in the lithosphere.

2.3.2 Dike Propagation: Fracturing and Fluid Flow

Here we develop a simplified dike propagation model that captures the behavior of more complete treatments of buoyant dikes propagating from an over pressured fluid source (e.g., Lister, 1990; Mériaux and Jaupart, 1998; Roper and Lister, 2005). A dike propagates when the sum of the excess pressure, P, and tectonic stress (horizontal normal stress at the base of the lithosphere), σ, equals or exceeds the critical stress, $P(z{=}h)+\sigma \geq K_c/\sqrt{h}$, where h is the dike height and K_c is the critical stress intensity factor (Lawn, 1993; Rubin, 1995). We assume constant K_c=1 MPa m$^{1/2}$ (Rubin, 1995), though at high confining pressures this relation may not hold (Rubin, 1993). Note that we use the sign convention in which $\sigma > 0$ is a tensile stress.

In a propagating dike, gradients in P arise from buoyancy and viscous resistance:

$$\frac{\partial P}{\partial z} = \Delta\rho g - \frac{12 Q \mu_f}{w^3}, \tag{2.1}$$

where $\Delta\rho$ is the density difference between fluid and host rock, w is the full dike width, μ_f is fluid viscosity, Q is the fluid volume flux and z is the vertical coordinate, increasing upwards from the LAB at z=0. The second term is simply the pressure gradient in a channel (Turcotte and Schubert, 2002). Buoyancy-driven dikes propagating into an elastic half space maintain almost constant thickness from their base to close to their tip due to the balance between the viscous and buoyant pressure gradients (Lister, 1990), even with an overpressured source (Roper and Lister, 2005). So we assume h, w and Q are independent of z. Thus integrating equation 2.1 over z and requiring that $P(h)$ equals the critical P for propagation results in

$$Q = \frac{w^3}{12\mu_f h}\left(P_d + \sigma - \frac{K_c}{\sqrt{h}} + \Delta\rho g h\right), \tag{2.2}$$

where P_d is the excess pressure at the dike base. Equation 2.2 captures the evolution in driving and resisting forces determined in more complete models. When dikes are small, $\frac{K_c}{\sqrt{h}}$ is large and an equivalently large source pressure or tectonic stress is required for a dike to grow ($Q > 0$). As a dike begins to grow, $\frac{K_c}{\sqrt{h}}$ decreases, which some studies (e.g. Mériaux and Jaupart, 1998; Roper and Lister, 2005) use as justification for neglecting this term entirely. In addition, as h increases, the buoyancy term becomes more important relative to $P_d + \sigma$, and $\Delta\rho g h$ eventually dominates, causing a nonlinear acceleration in growth when the base pressure is constant (Roper and Lister, 2005).

Pollard (1976) provided an analytical solution for $w(z)$ when pressure varies linearly with z. Taking w, h and Q as independent of z in integrating equation 2.1 to arrive at equation 2.2 implies constant pressure gradients, so we calculate the dike width by substituting the buoyant and viscous pressure gradients into Pollard's relationship (equation 1, Pollard (1976)), substituting equation 2.2 and solving for w at z=0:

$$w = \frac{2h}{M}\left((P_d + \sigma)(1 - 1/\pi) + \frac{K_c}{\pi\sqrt{h}}\right), \tag{2.3}$$

where M is the elastic stiffness of the host rock (Table 2.1).

Finally, mass conservation relates Q to $\frac{\mathrm{d}h}{\mathrm{d}t}$. Since w does not vary much along h, the total area (volume per unit length of strike) of the dike is $\sim wh$ and Q=$\frac{\mathrm{d}}{\mathrm{d}t}(wh)$. Applying the product rule, and substituting equation 2.3 yields

$$\frac{\mathrm{d}h}{\mathrm{d}t} = \frac{Q - (1-1/\pi)\frac{2h^2}{M}\frac{\mathrm{d}P_d}{\mathrm{d}t}}{2w - \frac{K_c\sqrt{h}}{M\pi}}. \tag{2.4}$$

Given an excess base pressure, equations 2.2, 2.3, 2.4 constitute an initial value problem. The following section describes the evolution of P_d and the details of the numerical solution are presented in Section 2.3.5.

2.3.3 Dike Propagation: the Source Region

We treat the source region for diking as a compressible, poro-elastic medium, in which case the conservation equation for fluid mass reduces to a pressure diffusion equation (e.g. Brace *et al.*, 1968; Wong *et al.*, 1997):

$$\frac{\partial P}{\partial t} = \frac{1}{\beta_{\mathrm{e}}}\nabla \cdot \left(\frac{k}{\mu_f}\nabla P\right), \tag{2.5}$$

where β_{e} is the effective compressibility. β_{e} is related to the compressibility of the porous matrix, β_{PM}, the intrinsic compressibility of the solid, β_{s}, and the fluid compressibility, β_{f}, by $\beta_{\mathrm{e}}=\beta_{\mathrm{PM}} + \phi\beta_{\mathrm{f}} - (1+\phi)\beta_{\mathrm{s}}$ (Brace *et al.*, 1968). The matrix compressibility can be written $\beta_{\mathrm{PM}}=\beta_{\mathrm{s}}(1+c\phi)$ with c between 3 and 10 (Renner *et al.*, 2000; Coble and Kingery, 1956), in which case $\beta_{\mathrm{e}}=\phi(\beta_f + c\beta_s)$. The compressibility of silicate melt is $\sim 0.5 \cdot 10^{-10}$ Pa^{-1} (Lange and Carmichael, 1990), similar to rock at LAB depths so we take $\beta_f + c\beta_s \approx 10^{-10}$ Pa^{-1} as a representative value.

Treating the source region as elastic during dike propagation is justified because dike growth is on the order of tens of hours while the viscous decompaction time scale is tens of thousands of years (Results, Section 2.4). Furthermore, a porous source is used because excess pressures in a DBL are sufficient to initiate dikes well before disaggregation (Results, Section 2.4). Fowler and Scott (1996) and Rubin (1998) used a similar description of the source region in studying dike growth in partially molten materials. In these earlier studies, melt migrates horizontally through the porous dike walls, allowing the dike to grow vertically. In contrast, our model considers a dike that only propagates upward, by drawing melt into its base.

At the base of the dike, P decreases as melt is extracted, which eventually slows dikes growth. The pressure decrease diffuses downward and outward into the partially molten source at a rate that depends on the local distribution of ϕ and $k(\phi)$ (Table 2.2). Regions of high ϕ are regions of high permeability and thus high pressure diffusivity, so that the state of the DBL when dikes initiate dictates the local pressure diffusivity. The diffusivity is highest at the top of a DBL and decreases deeper into the asthenosphere.

The source region is coupled to the dike (Section 2.3.2) by conserving mass and requiring that P is continuous at the dike entrance. While the boundary conditions are conceptually straightforward, the challenge of coupling the diffusion equation to the dike propagation system is the large difference in length scales involved; the dike entrance is on the order of cm while the pressure diffusion length scale is tens of m to km (e.g., taking a porosity of 0.01, the diffusivity is $D{=}k/(\phi\mu_f\beta) \approx 0.3$ m^2/s, which together with a typical dike growth time of ∼10 hours, gives a diffusion distance of ∼200 m). Because of the large difference in scales, it is appropriate to treat the dike as a line sink in cylindrical coordinates (radial coordinate r, angular coordinate θ, see Figure 2.1c).

The construction of our solution is based on the presence of a region close to the dike entrance in quasi-steady state. For a line sink into which there is a constant flow rate, the radial flux in regions where $r{<<}2\sqrt{Dt}$ is independent of time (see supplemental material). Thus, in regions where $r{<<}2\sqrt{Dt}$, the flow rate across a semicircular surface close to the dike must equal the flow rate in the dike, $-Q{=}\pi r S_r$, where S_r is the radial Darcy flux, $S_r{=}-k\frac{\partial P}{\partial r}/\mu_f$. Substituting S_r, integrating over r

and solving for the excess pressure at the base of the dike under the constraint that mass flux at the dike entrance, $r{=}w/2$, equals the mass flux in the dike ($\pi \frac{w}{2} S_r(w/2){=}-Q$) yields

$$P_d = P(r) + \frac{\mu_f Q}{\pi k} \ln \frac{w/2}{r}. \tag{2.6}$$

Our approach is to solve equation 2.5 numerically with a flux boundary condition $S_r{=}-Q/(\pi r)$ applied at a small distance, r_o, beyond the dike entrance to update $P(r_o)$ (see Section 2.3.5 for numerical approach). We then calculate the excess pressure at the base of the dike, P_d, using equation 2.6, which is used in the crack propagation equations. Results presented here used $r_o{=}1$ m; decreasing r_o by an order of magnitude changes the results by only a few percent (while significantly increasing computation time). The time it takes for $r_o{<<}2\sqrt{Dt}$ to be satisfied is a small fraction of the growth time of a dike so that errors introduced at t near 0 should be negligible; at $r_o{=}1$ m with $D{=}0.3$ m^2/s, it takes $\sim$1 minute for $r_o{<<}2\sqrt{Dt}$, compared to tens of hours of growth.

Because melt fraction increases at the top of a DBL, the diffusivity will be maximum at the LAB and decrease with depth. To simplify the solution, we consider a constant diffusivity that reflects the average ϕ just under the LAB and solve equation 2.5 in 1D cylindrical coordinates with constant diffusivity.

2.3.4 Freezing

As a dike leaves the source region, the magma in direct contact with the host rock freezes, forming a chilled margin of thickness w_{chill} along the dike edges. w_{chill} grows at a velocity of $\lambda\sqrt{\kappa/t}$ (p. 163, Turcotte and Schubert, 2002) where λ is a constant that depends on the horizontal temperature difference between the magma and host rock temperature and the latent heat of crystallization. The host rock temperature decreases with height above the base of the lithosphere, so that the horizontal temperature difference and thus λ depends on z and different geotherms result in different freezing rates at a fixed height above the LAB. Rather than fully couple the freezing to the dike propagation model, we calculate the dike growth and freezing separately and compare the two as a first order indicator of whether or not a dike freezes.

2.3.5 Numerical Approach

The numerical scheme employed for the propagation of a single dike is as follows. Given initial conditions for P and ϕ from the viscous decompaction model and constant tectonic stress σ, we use the critically unstable dike height as the initial height. We do not address the origin of initial flaws in our model, but possibilities include sub-critical crack growth from stress concentrations along grain boundary triple junctions (Rubin, 1998) or microfracturing in porosity waves (Cai and Bercovici, 2013).

After the initial height is calculated, we calculate the width (equation 2.3), flow rate (equation 2.2) and growth rate (equation 2.4). We then use an explicit finite volume discretization (Euler forward step, centered in space) of the pressure diffusion equation (equation 2.5) with the aforementioned flux condition $S_r\big|_{r_o} = -Q/(\pi r)$ and a fixed pressure at the extent of the computational domain (r=20 km) to calculate $\frac{\partial P}{\partial t}$. The domain is large enough so that the diffusion front does not interact with the boundary. We then simultaneously update the height h and source pressure $P(r)$ over a time step that is the minimum of the 2D diffusion stability criteria and an Euler time step limiter, in which the change in h over a single time step is small (i.e. $h_{\text{new}} - h_{\text{old}} = \epsilon h_{old}$, where ϵ is small). We used $\epsilon = 10^{-3}$, and further decreasing ϵ does not change our results. Because w, Q and P_d (equations 2.3,2.2 and 2.6) are mutually dependent, we solve the three equations simultaneously after updating h and $P(r)$ using a zero finding method via MATLAB (MATLAB, 2010).

The relationship for dike growth rate (equation 2.4) contains a term that depends on the time derivative of P_d. We neglect this term and verify that it is about an order of magnitude smaller than Q by calculating $\frac{\mathrm{d}P_d}{\mathrm{d}t}$ after each run.

To calculate the chilled margin width, we discretize the vertical coordinate above the LAB into a set of finite nodes, z_i, and record the time since the arrival of the dike at each height, $t_a(z_i)$. We then calculate $w_{\text{chill}}{=}2\lambda\sqrt{\kappa t_a}$ by choosing a far-field temperature $T(z)$ and solving for λ at each height by numerically solving the transcendental equation that arises in the similarity solution of a moving freezing front (p. 163 Turcotte and Schubert, 2002) using the specific heat, thermal diffusivity and latent heat of crystallization in Table 2.1. If $w_{\text{chill}} \geq w/2$ at any time or height, a dike is considered frozen.

2.4 Results

We first show the evolution of a decompacting boundary layer (DBL) beneath the LAB with no diking in order to estimate the typical excess pressure and melt fraction available to drive diking. We then focus on the growth of a single dike independent of DBL evolution to illustrate the influence of initial excess pressure, tectonic stress, source porosity, dike viscosity and lithosphere thermal structure on dike propagation. Combining the results of a single dike with estimates for dike spacing and recurrence interval, we calculate a time-averaged dike flux that can be applied as a time variable boundary condition in a DBL with diking.

The evolution of a DBL dictates the starting conditions for diking, so we present a reference case with no diking to constrain when dikes initiate. Figure 2.1b shows the evolution of normalized melt fraction, ϕ/ϕ_o, vs depth in reference compaction lengths, δ_c, beneath the LAB. For ϕ=0.01 and a grain size of 1 cm, the DBL thickness is about 10 km. The excess pressure is highest just beneath the LAB, so in Figure 2.2 we plot $\phi(z{=}0, t)$ and $P(z{=}0, t)$ for ϕ_o=0.01 for the case of a melt dependent (dashed line) and independent (solid line) compaction viscosity, $\xi{=}\eta\phi^{n_\xi}$ (see supplemental material for more on ξ). Varying the melt dependence of ξ controls the initial excess pressure and accumulation rate. With ξ=η/ϕ, accumulation is slower because ξ is higher. Increasing ξ also increases $P(z{=}0)$ because the excess pressure at the top of a DBL scales with $\Delta\rho g\delta_c$ and δ_c is a function of ξ.

By comparing these calculations to the excess pressure required for dike formation, we find that small dikes are unstable for the excess pressure generated in a DBL at melt fractions less than the disaggregation limit. The magnitude of $P(z{=}0)$ is $\sim$40 MPa for the more realistic case of ξ=η/ϕ, indicating that small flaws would be critically unstable (for 10 MPa and a critical stress intensity of 1 MPa m$^{1/2}$, the critical flaw size is $\sim$1 cm). Increasing ϕ_o by an order of magnitude increases $P(z{=}0)$ by an order of magnitude. We used a representative value of η=10^{19} Pa s for the cases presented here. Increasing η by a factor of 10 increases $P(z{=}0)$ by $10^{1/2}$ and increases the accumulation time by a factor of 10 (time scales with $\xi/(\Delta\rho g\delta_c)$). The high excess pressure at small melt fraction justifies treating the source for diking as porous rather than disaggregated.

The behavior of a single dike propagating from a porous source region is controlled by the initial excess pressure, tectonic stress, source porosity, fluid viscosity and lithosphere thermal structure. Figure 2.3 shows the evolution of height, h, width, w, and excess pressure at the dike base, P_d, for systematic variations in the test parameters. In Figure 2.3, we do not include dike freezing in order to isolate the physical controls on dike propagation. In all cases, dike height increases roughly linearly in time while the rate of increase in dike width decreases in time as the base pressure falls. The source porosity, ϕ_{DBL}, has a strong control on dike growth; increasing ϕ_{DBL} from 0.01 to 0.03 and keeping the fluid viscosity and tectonic stress fixed increases the height and width by a factor of $\sim$3 at 35 hours. The excess pressure at the dike base, P_d, asymptotically approaches the applied tectonic stress and increasing tectonic stress results in a faster growth rate and wider dike. If the fluid in the dike is a mixture of melt and suspended crystals, the viscosity of the composite would increase, so we also varied the dike melt viscosity while keeping the source fluid viscosity constant. Higher dike viscosity results in a slower growth rate, but an increased dike width.

Pressure-diffusion-limited dikes are only a few cm wide at most and freeze after propagating a short distance into the lithosphere. Figure 2.4 shows the dike variables when a portion of the dikes freezes for the same variation in parameters as Figure 2.3 for geothermal gradients of 10 ^{o}C/km and 15 ^{o}C/km at the base of the lithosphere. For source melt fractions, ϕ_{DBL} less than 0.05, dikes are no more than a few km tall and few cm wide. For higher source melt fractions, dikes propagate ~10 km above the LAB. A smaller geothermal gradient allows dikes to propagate farther. Though a higher melt viscosity results in slower growth (Figure 2.3), dikes with higher viscosity propagate farther because they are wider and take longer to cool.

The minimum recurrence interval for diking is the sum of the emplacement time, t_e (shown in Figure 2.4), and the elapsed time required for the excess pressure to recover to pre-dike levels, t_r. We estimate t_r by removing the pressure sink when a dike freezes and calculating the time for the final pressure field in the asthenosphere to return to pre-dike levels. Recovery time is on the order of hours to days with larger ϕ_{DBL} requiring only a few hours for pressure to build up to pre-dike levels. Though dikes limited by the partially molten source only propagate a few km before freezing, successive emplacement of dikes could thermally erode the lithosphere at a rate dependent on the recurrence interval (see Section 2.5).

When more than one dike forms, adjacent dikes compete for melt when the low pressure front from adjacent dikes interacts. The diffusion front distance, the minimum spacing for non-interacting cracks, is estimated by the poro-elastic diffusion distance, $2\sqrt{Dt}$. For a source region with ϕ_{DBL}=0.01 and 0.25, dikes interact when spaced closer than about ~200 m and ~10 km, respectively (Figure 2.4d).

Because dike growth and recurrence times are orders of magnitude shorter than the time scale of melt accumulation in a DBL (days vs kyrs), modeling the evolution of a DBL due to the successive emplacement of dikes requires scaling the results of a single dike up to a time scale consistent with a DBL. We assume that dikes are emplaced with regular spacing and timing and that each emplacement is unaffected by previous diking events, though it is possible that dikes may intrude more easily in locations of previous intrusions. The volume of melt extracted from a DBL by a single dike is simply the area of the dike at freezing, $\sim wh$. Assuming that dikes are emplaced as soon as excess pressure builds up to pre-dike levels, then the melt flux out of a DBL due to diking is $\sim wh/(t_e + t_r)$ where t_e is the emplacement time and t_r is the recovery time. The volumetric flow rate out of the DBL due to diking is then,

$$S_{\text{dike}} = \frac{wh}{(t_e + t_r)}/d, \tag{2.7}$$

where d is the dike spacing. Using the minimum spacing for dikes not to compete for melt as the dike spacing, we calculate S_{dike} as a function of ϕ_{DBL}, shown in Figure 2.5. The vertical melt flux into the DBL, $S_{\text{b}}=\frac{(1-\phi_o)\Delta\rho g k(\phi_o)}{\mu}$, for ϕ_o of 0.01, 0.03 and 0.05 (horizontal lines) is also plotted in Figure 2.5. Initially for small ϕ_{DBL}, $S_{\text{dike}}<S_{\text{b}}$, implying net accumulation early in DBL formation. As ϕ_{DBL} increases and S_{dike} approaches S_{b}, the dike flux balances the buoyant flux, indicating that a DBL should evolve to a steady state in which ϕ_{DBL} is constant. The steady state ϕ_{DBL} increases as ϕ_o increases because a larger buoyant flux is balanced by greater vertical transport rate in dikes. Numerical solutions (see supplemental material) of the DBL system using S_{dike} as a time dependent boundary condition at the LAB shows that ϕ_{DBL} reaches a steady state after $\sim$10 kyrs. For the range of dike parameters tested, the steady state melt fraction is between 2.5 and 4 times larger than the background

asthenosphere melt fraction.

2.5 Discussion

Our results can be applied to investigate how dike propagation driven by melt accumulation at the LAB affects the evolution of the lithosphere and seismic discontinuity at the LAB. In this section, we use the steady state dike flux from Section 2.4 to estimate the thermal erosion rate of the lithosphere and the long term melt fraction in a DBL.

To study lithosphere thinning, we consider the heat released by freezing dikes at the LAB. The LAB temperature is taken as the solidus temperature, T_m, and we employ a moving coordinate system with z=0 fixed on the LAB (Figure 2.6). The temperature in $z\leq 0$ is constant so as heat is released, the LAB moves upwards at a velocity, V. Above the LAB, a thermal boundary layer (TBL) with a thickness δ, that is thin compared to the thickness of the lithosphere, conducts heat away from the LAB. To be clear, the lithosphere is itself a conductive TBL, but we are considering a transient TBL superimposed on the lithospheric geotherm (Figure 2.6).

Because dike height is much less than δ, we approximate the heat source as a discontinuous planar heat source just above the LAB. The heat source is given by $q_o = S_{\mathrm{dike}}\rho_f H$, where H is the latent heat of crystallization. Carslaw and Jaeger (1959, p 267) treated the problem of heat release on a moving plane and showed that at steady state $\delta \approx \kappa/V$ with $V = q'/(\rho_m C_p \Delta T)$, where κ is the thermal diffusivity, q' is the heat source and ΔT is the difference between the temperature at $z\leq 0$, T_m, and the temperature at $z>>0$, T_o (Figure 2.6). In our application, the boundary is moving on the geotherm so that an additional conductive heat flux carries heat away at a rate $-k\alpha$ where α is the original geothermal gradient just above the LAB and k the thermal conductivity. The effective heat source is then $q' = q_o - k\alpha$ and assuming $\rho_f \approx \rho_m$, the boundary velocity is

$$V = \frac{S_{\text{dike}} H / C_p - \kappa\alpha}{\Delta T}. \tag{2.8}$$

Carslaw and Jaeger (1959) used constant ΔT, but here, ΔT changes as the LAB moves upward (Figure 2.6). To approximate a variable ΔT, we assume instantaneous steady state at each increment of thinning and take ΔT as the difference between the solidus temperature and the original temperature at the current depth. Assuming constant α, ΔT=αl where l is the distance the freezing front has moved above the initial lithosphere base (Figure 2.6). The assumption of quasi-steady state is reasonable as long as the δ is small compared to the thickness of the remaining lithosphere, $L - l$, where L is the initial lithosphere thickness. Substituting ΔT=αl into equation 2.8 gives:

$$V = \frac{\frac{S_{\text{dike}} H}{C_p \alpha} - \kappa}{l}. \tag{2.9}$$

Substituting S_{dike} from Section 2.4, equation 2.9 predicts that lithosphere erosion (V>0) occurs only if $\phi_{DBL} > 0.014$ for the low melt viscosity (1 Pa s) and high stress (10 MPa) case (Figures 2.5). ϕ_{DBL}=0.014 is maintained by $\phi_o \approx 0.006$ assuming $\phi_{DBL} \sim 2.5\phi_o$.

As noted above, equation 2.9 is applicable when $\delta << L - l(t)$. Because $\delta \approx \kappa/V$ and V depends on melt fraction, changing ϕ_{DBL} changes when this condition is not satisfied. For ϕ_{DBL}=0.02 and 80 km thick lithosphere, δ approaches $L - l(t)$ after ~50 km of thinning, so that our model is appropriate for thinning of most of the mantle lithosphere. DBL melt fractions of 0.02 and 0.03 result in an average thinning velocity of 1 and 6 km Myr^{-1} over the first 40 km of thinning, respectively. Once δ becomes comparable to the remaining lithosphere thickness, the geothermal gradient

α changes rapidly and thinning would proceed as in the model of England and Katz (2010, Appendix B.3).

One difference between base up erosion and distributed lithosphere heating (e.g. Bialas *et al.*, 2010) is that even in magma rich regions, dikes fed by a DBL would erode the lithosphere without surface eruptions, perhaps explaining how crustal extension in some rift zones can pre-date volcanic activity (McHone *et al.*, 2005) even if the lithosphere is initially too strong to rift. A recent study of mantle structure beneath Afar shows a LAB signal on the rift flanks while directly beneath the rift there is no corresponding decrease (Rychert *et al.*, 2012). Our results suggest that the absence of a melt accumulation boundary is explained by dike-induced lithosphere thinning.

Because a DBL is not emptied by diking, the LAB discontinuity (e.g. Rychert *et al.*, 2005; Fischer *et al.*, 2010) could reflect a stable boundary layer of melt. The LAB depth should reflect where the melt solidus crosses the geotherm, a function of the initial LAB depth, the time since melting began and variations in melt production. By stacking SS precursors, Schmerr (2012) mapped the LAB magnitude and depth across the Pacific. Schmerr observed an intermittent LAB signal with the strongest signals near hot spots and found that the magnitude of the velocity decrease required only 0.001 to 0.03 melt. Using our result $\phi_{DBL} \sim 2.5\phi_o$ yields ϕ_o in melt-producing regions of the Pacific between 0.0004 and 0.01, within the range found beneath the East Pacific Rise (Forsyth, 1998; Evans *et al.*, 1999). The higher melt fraction yields positive erosion rates, so that a melt-enhanced LAB would shallow considerably over the lifetime of an oceanic plate. While observed locally in Hawaii (Li *et al.*, 2004), LAB thinning is not observed in general in the Pacific. Possible explanations are that (1) melt supply is limited and solid state mechanisms cause the LAB discontinuity in most of the Pacific, (2) the melt fraction is below the threshold to cause thinning or (3) compressive tectonic stresses limit diking.

The dike widths predicted by our model are consistent with pyroxenite dikes in the upper mantle section of ophiolites, typically ∼1cm wide (e.g. Nicolas and Jackson, 1982). Our model shows that to obtain dikes larger than a few cm, such as dikes greater than 1 m wide commonly observed at MORs and continental rifts (McHone *et al.*, 2005; Qin and Buck, 2008), the melt flux into a DBL must be greater than that supplied by a vertical buoyant flux alone. The melt flux may increase due to migration along a dipping solidus isotherm (Sparks and Parmentier, 1991; Spiegelman, 1993), the creation of high-porosity pathways formed by shear (Stevenson, 1989; Holtzman *et al.*, 2003), reactive infiltration instabilities (Daines and Kohlstedt, 1994; Aharonov *et al.*, 1995) or melting of mantle heterogeneities (Katz and Weatherley, 2012).

2.6 Summary

In summary, when melt generated in the asthenosphere rises buoyantly and collects at the intersection of the melt solidus and the geotherm, dikes about 1 cm wide relieve the overpressure, balancing the buoyant flow of melt from the source region. This process results in a steady state melt fraction at the base of the lithosphere that is greater than in the background asthenosphere. If the asthenosphere melt fraction is greater than $\sim 6 \cdot 10^{-3}$, the repeated intrusion of small dikes thins the lithosphere. Eventually extension of the crust and remaining lithospheric mantle can occur if there is a tensile tectonic stress.

2.7 Acknowledgements

We thank N. Schmerr, W.R. Buck and an anonymous reviewer for comments that greatly improved the manuscript. Thanks also to editor Y. Ricard for his own reading and evaluation of the work presented here. A final thanks to N. Kusznir for early discussions from which this project emerged. This research was partially supported by NSF grant OCE-0728028 to EMP.

2.8 Supplemental Material

2.8.1 Viscous Two Phase Flow and DBL Evolution

To address magma accumulation beneath a permeability barrier, the asthenosphere is treated as a two-phase compressible medium (McKenzie, 1984; Scott and Stevenson, 1984; Fowler, 1985; Bercovici *et al.*, 2001). The equations used here are most similar to the one dimensional form of McKenzie (1984), solved in terms of excess pressure. In one dimension, the conservation of momentum and mass can be combined into a single equation that can be solved for the excess melt pressure, P, if the melt fraction, ϕ, is known (see Table 2.1 for symbols):

$$\frac{-P}{\xi} + \frac{\partial}{\partial z}\left[\frac{k}{\mu_f}\left(\frac{\partial}{\partial z}\left((1-\phi)(1+(4/3)\frac{\eta}{\xi})P\right)\right)\right] = -\frac{\partial}{\partial z}\left(\frac{k(1-\phi)\Delta\rho g}{\mu_f}\right). \quad (2.10)$$

The solid compaction viscosity, ξ, and permeability, k, vary with ϕ while the fluid shear viscosity, μ_f, is held constant. We adopt $k = \frac{a^2\phi^3}{300}$ (Wark and Watson, 1998) and $\xi = \eta\phi^{n_\xi}$, where η is the solid shear viscosity. The value of n_ξ is discussed below. The following equations relate the gradient in P to the separation velocity (Darcy flux), S, fluid velocity, v^f, and the rate of change in ϕ.

$$S = -\frac{k}{\mu_f}\left(\frac{\partial}{\partial z}\left((1-\phi)(1+\frac{4\eta}{3\xi})P\right) + (1-\phi)\Delta\rho g\right), \quad (2.11)$$

$$v^f = \frac{S}{\phi} - S, \quad (2.12)$$

$$\frac{\partial\phi}{\partial t} = -\frac{\partial}{\partial z}(\phi v^f). \quad (2.13)$$

Equation 2.11, a generalized form of Darcy's law, shows that melt flows in response to pressure gradients generated by buoyancy and compaction. Equation 2.12 arises from fluid and solid mass conservation and equation 2.13 is a statement of conservation of fluid mass with no melting. Note that S is also related to the fluid and solid velocities by $S = \phi(v^f - V^s)$. Given ϕ, P is calculated by solving equation 2.10. The resulting P determines S (equation 2.11) and v^f (equation 2.12), which are used to advect ϕ (equation 2.13).

The domain extends from $z = 0$ to $z = 10\delta_c$, where δ_c is a reference compaction length, $\delta_c \equiv \sqrt{\xi k/\mu_f}$. By limiting our domain to the top of the melting column, we can maximize resolution in the DBL and focus on the coupling at the LAB. We use a finite volume discretization for all the equations with 1000 uniform elements so that variations in melt fraction near $z = 0$ are well resolved. P is calculated using a direct solver and ϕ is advected using a second order accurate Van Leer scheme (Van Leer, 1977; Hourdin and Armengaud, 1999).

The compaction viscosity, ξ, is perhaps the least well constrained parameter above despite its importance in determining the evolution of a DBL. Theoretical considerations require that ξ goes to infinity as $\phi \to 0$ and so a form of $\xi = \eta\phi^{n_\xi}$, with η being the shear viscosity and $n_\xi = -1$, is commonly used (e.g. Bercovici *et al.*, 2001; Simpson *et al.*, 2010) but there is limited observational or experimental work that has verified that this relationship holds in nature. Recent experimental work by Renner *et al.* (2003) shows a definite dependence of ξ on ϕ, with $n_\xi = -1$ plausible. To illustrate the signifance of the melt dependence of ξ, Figure 2.7 shows the evolution of an initially uniform distribution of melt beneath an impermeable barrier for the case of melt-independent ξ ($n_\xi = 0$, Figure 2.7a) and melt-dependent ξ ($n_\xi = -1$, Figure 2.7b). The boundary conditions are $S = 0$ at $z = 0$, and $P = 0$ and $\phi = \phi_o$ at $z = 10\delta_c$ and values for fixed parameters are given in Table 2.1. As expected, ϕ increases beneath the impermeable boundary in both cases. When ξ varies inversely with ϕ the boundary layer that develops is thicker due increased compaction length.

Because the excess pressure at the top of the DBL scales with compaction length (as $\Delta\rho g\delta_c$), the porosity dependent ξ increases the excess pressure at the boundary. But because the time scale is controlled by ξ and ξ varies in time, decompaction takes longer and the excess pressure actually starts to decrease as melt accumulates (Figure 2.8). Figure 2.8 shows ϕ (2.8a), ξ (2.8b), dilatation rate θ (2.8c) and P (2.8d) at $z = 0$ in time for both cases in Figure 2.7. When $n_\xi = 0$, P is initially a few MPa, increases rapidly in the first thousand years, and then increases more gradually. When $n_\xi = -1$, P_o is $\sim$ 40 MPa and begins to decrease after a few kyr. The decrease can be understood by considering the relationship between ξ, θ and P: $P = \xi\theta$. For both $n_\xi = 0$ and $n_\xi = -1$, the dilatation rate increases as ϕ increases (Figure 2.8c). When $n_\xi = 0$, this simply results in an increase in P, but when $n_\xi = -1$, ξ decreases more rapidly than θ increases, resulting in a lower P.

If $n_\xi = -1$ as laboratory and theoretical studies suggest, P generated in a DBL may be higher than typically considered (e.g. Rubin, 1998; Kelemen and Aharonov, 1998). It is possible, however, that P greater than $\sim$10 MPa may not be achievable in the asthenosphere because nonlinear creep mechanisms would activate (Schwenn and Goetze, 1978).

The results shown in the main text give the flux of melt out of the asthenosphere due to diking, S_{dike}, as a function the source melt fraction for diking in the DBL, ϕ_{DBL}, for different values of diking parameters such as dike fluid viscosity and tectonic stress. This result can be used as a time-variable boundary condition at z=0 by taking ϕ_{DBL} as the melt fraction at the top of a DBL. For simplicity, we fit a continuous curve of the form $S_{\text{dike}} = A\phi_{DBL}^3$ to the numerical result in Figure 2.5 of the main text. For the case when the dike viscosity is 1 Pa s and the tectonic stress is 10 MPa, $A \approx 5 \times 10^{-5}$ m/s and when the dike viscosity is 10 Pa s and the tectonic stress is 5 MPa, $A \approx 2 \times 10^{-5}$ m/s.

The evolution of the melt fraction at the top of a DBL normalized by the imposed reference melt fraction is shown in Figure 2.9. In all cases, ϕ_{DBL} initially increases then oscillates with decreasing amplitude about a mean melt fraction consistent with the inferred steady state melt fraction from Figure 5 of the main text. Steady state is reached in a few 10s of kyrs. The diking parameters, rather than the reference melt fraction determine the steady state ratio of $\phi_{\mathrm{DBL}}/\phi_o$.

2.8.2 Line Sink Solutions to Time Dependent Diffusion

In coupling a propagating dike to a poro-elastic source region, we make use of intuition gained by considering a line sink solution to the transient diffusion equation. This appendix gives a brief overview of line sinks, following the approach of Carslaw and Jaeger (1959, p 255-263), who considered the analogous problem of heating due to heat sources of various geometries. For the dike propagation problem, the source region is governed by the transient diffusion equation,

$$\frac{\partial P}{\partial t} = \underline{\nabla} \cdot D \underline{\nabla} P, \tag{2.14}$$

where P is pressure and D is the hydraulic diffusivity. For constant diffusivity, solutions for a continuous line sources can be constructed by first integrating the solution for an instantaneous point source over a spatial dimension, then integrating the result over time, to arrive at the solution for the pressure due to a continuous line source that varies in time (Carslaw and Jaeger, 1959, p 261):

$$P = \frac{1}{4D\pi} \int_0^t \frac{q(t')}{t-t'} \mathrm{e}^{-\frac{r^2}{4D(t-t')}} \mathrm{d}t' + P_i \tag{2.15}$$

where $q(t)$ is the magnitude of the sink and P_i is the initial pressure. If the sink is constant, q_o, 2.15 can be evaluated analytically by making the substitution $u = r^2/(4D(t-t'))$, leading to

$$P = \frac{q_o}{4D\pi}\mathrm{Ei}\left(\frac{r^2}{4Dt}\right) + P_i. \tag{2.16}$$

where $\mathrm{Ei}(x)$ is the exponential integral, defined as

$$\mathrm{Ei}(x) = \int_x^\infty \frac{\mathrm{e}^{-g}}{g}\mathrm{d}g \tag{2.17}$$

The radial flux, $S_r = -\frac{k}{\mu}\frac{\partial P}{\partial r}$, determines the flow rate into the sink. Using Leibniz' rule of integration (Boas, 1983, p 233) and the chain rule,

$$S_r = \frac{kq_o}{2\mu D\pi r}\mathrm{e}^{-\frac{r^2}{4Dt}}. \tag{2.18}$$

Integrating this result about a semicircle of radius r, the total flux, Q, is

$$Q = \frac{kq_o}{2D\mu}\mathrm{e}^{-\frac{r^2}{4Dt}}. \tag{2.19}$$

The form of equation 2.19 shows that a region of constant flux develops where $r << 2\sqrt{Dt}$. When $r << 2\sqrt{Dt}$, the pressure sink, q_o, can be written in terms of a mass flux as $q_o = \frac{2D\mu}{k}Q$. This relationship reflects the underlying coupling between a dike propagating from a poro-elastic source region; the mass flux in the dike causes a pressure sink, the magnitude of which is determined by the mass flux as well as the hydraulic properties of the source region. The pressure in regions where $r << 2\sqrt{Dt}$ is given by expansion of $\mathrm{Ei}(x)$ for small x (Carslaw and Jaeger, 1959, p 262):

$$P = -\frac{q_o}{4D\pi}\left[\ln\left(\frac{r^2}{4Dt}\right) - \gamma\right] + P_i, \tag{2.20}$$

where $\gamma = 0.5772...$ is Euler's constant. Equation 2.20 can also be deduced from physical arguments by assuming that the flux is constant and integrating equation 2.19 after taking the limit in which $\frac{r^2}{4Dt} << 1$. The important point is that because the flux is constant, the pressure becomes more negative indefinitely ($\frac{r^2}{4Dt} << 1$ so the logarithmic term is negative, and $q_o < 0$ for a sink, so overall P decreases.)

In the problem of interest - a dike propagating from a poro-elastic source - the flux varies in time. One approach would be to use a finite discretization of equation 2.15, but because of the nonlinear relationships between dike width, flow rate and pressure (see main text) small numerical errors are amplified and we are not able to devise a stable numerical strategy when using equation 2.15. We can, however, obtain a reasonable, approximate and numerically stable solution using a semi-analytical approach. We assume that there is some small region of radius r_o close to the dike entrance that is always at the steady state flux (i.e. $r_o << 2\sqrt{Dt}$). The flux in $r < r_o$ is constant, so that 2.20 is applicable and if $P(r_o)$ is known, then the pressure at the base of the dike, P_d, can be calculated by subtracting $P_d - P(r_o)$ and calculating the dike base pressure by evaluating 2.20 at half the dike width, $w/2$:

$$P_d - P(r_o) = \frac{2q_o}{4D\pi}\ln\left(\frac{r_o}{w/2}\right) \tag{2.21}$$

Substituting $q_o = -\frac{2D\mu}{k}Q$ (the negative sign accounts for the fact that a positive flux in the dike is a pressure sink in the source region) and solving for P_d, we arrive at equation 6 of the main text:

$$P_d = P(r_o) + \frac{\mu Q}{k\pi} \ln\left(\frac{w/2}{r_o}\right) \tag{2.22}$$

In the region $r \geq r_o$, we calculate the pressure by a numerical solution of the transient diffusion equation in 1D cylindrical geometry with a time variable flux boundary condition at $r = r_o$ and a fixed pressure, P_i, at a distance that is sufficiently large so that pressure variations do not interact with the boundary. $P(r_o)$ from the numerical calculation can then be used along with equation 2.22 to extrapolate to the dike pressure P_d. The numerical solution uses a 2$^{\text{nd}}$ order accurate finite volume spatial discretization and first order accurate forward temporal projection of the transient diffusion equation on a domain that extends to $r = 20$ km on a variable mesh with minimum element size of 10 m at r_o.

2.9 References

Aharonov, E., J. A. Whitehead, P. B. Kelemen, and M. Spiegelman 1995. Channeling instability of upwelling melt in the mantle. *J. Geophys. Res. 100*(B10), 20433–20450.

Bercovici, D., Y. Ricard, and G. Schubert 2001. A two-phase model for compaction and damage 1. General Theory. *J. Geophys. Res. 106*(B5), 8887–8906.

Bialas, R. W., W. R. Buck, and R. Qin 2010. How much magma is required to rift a continent? *Earth and Planetary Science Letters 292*(1-2), 68–78.

Boas, M. 1983. *Mathematical Methods in the Physical Sciences, 2nd Edition*. Wiley.

Brace, W. F., J. B. Walsh, and W. T. Frangos 1968. Permeability of granite under high pressure. *J. Geophys. Res. 73*(6), 2225–2236.

Buck, W. R. 2004. Consequences of asthenospheric variability on continental rifting. In G. Karner, B. Taylor, N. Driscoll, and D. Kohlstedt (Eds.), *Rheology and Deformation of the Lithosphere at Continental Margins*, pp. 1–30. Columbia University Press.

Buck, W. R., L. L. Lavier, and A. N. B. Poliakov 2005. Modes of faulting at mid-ocean ridges. *Nature 434*(7034), 719–723.

Cai, Z., and D. Bercovici 2013. Two-phase damage models of magma-fracturing. *Earth and Planetary Science Letters 368*(0), 1–8.

Carslaw, H., and J. Jaeger 1959. *Conduction of Heat in Solids* (2 ed.). Oxford Univ Press.

Coble, R., and W. Kingery 1956. Effect of porosity on physical properties of sintered alumina. *Journal of the American Ceramic Society 39*(11), 377–385.

Cochran, J. R. 1983. A model for development of Red Sea. *AAPG Bulletin 67*(1), 41–69.

Daines, M. J., and D. L. Kohlstedt 1994. The transition from porous to channelized flow due to melt/rock reaction during melt migration. *Geophys. Res. Lett. 21*(2), 145–148.

England, P. C., and R. F. Katz 2010. Melting above the anhydrous solidus controls the location of volcanic arcs. *Nature 467*(7316), 700–703.

Evans, R. L., P. Tarits, A. D. Chave, A. White, G. Heinson, J. H. Filloux, H. Toh, N. Seama, H. Utada, J. R. Booker, and M. J. Unsworth 1999. Asymmetric Electrical Structure in the Mantle Beneath the East Pacific Rise at 17 °S. *Science 286*(5440), 752–756.

Fischer, K. M., H. A. Ford, D. L. Abt, and C. A. Rychert 2010. The lithosphere-asthenosphere boundary. *Annual Review of Earth and Planetary Sciences* **38**, 551–575.

Forsyth, t. M. S. T., D. W. 1998. Imaging the Deep Seismic Structure Beneath a Mid-Ocean Ridge: The MELT Experiment. *Science 280*(5367), 1215–1218.

Fowler, A. C. 1985. A mathematical model of magma transport in the asthenosphere. *Geophysical & Astrophysical Fluid Dynamics 33*(1), 63–96.

Fowler, A. C., and D. R. Scott 1996. Hydraulic crack propagation in a porous medium. *Geophysical Journal International 127*(3), 595–604.

Gaherty, J. B., T. H. Jordan, and L. S. Gee 1996. Seismic structure of the upper mantle in a central Pacific corridor. *J. Geophys. Res. 101*(B10), 22291–22309.

Ghods, A., and J. Arkani Hamed 2000. Melt migration beneath mid ocean ridges. *Geophysical Journal International 140*(3), 687–697.

Holtzman, B., N. Groebner, M. Zimmerman, S. Ginsberg, and D. Kohlstedt 2003. Stress-driven melt segregation in partially molten rocks. *Geochem. Geophys. Geosyst 4*(5).

Hourdin, F., and A. Armengaud 1999. The Use of Finite-Volume Methods for Atmospheric Advection of Trace Species. Part I: Test of Various Formulations in a General Circulation Model. *Monthly Weather Review 127*(5), 822–837.

Katz, R. F. 2008. Magma dynamics with the enthalpy method: Benchmark solutions and magmatic focusing at mid-ocean ridges. *Journal of Petrology 49*(12).

Katz, R. F. 2010. Porosity-driven convection and asymmetry beneath mid-ocean ridges. *Geochem. Geophys. Geosyst* **11**.

Katz, R. F., and S. M. Weatherley 2012. Consequences of mantle heterogeneity for melt extraction at mid-ocean ridges. *Earth and Planetary Science Letters 335336*(0), 226–237.

Kawakatsu, H., P. Kumar, Y. Takei, M. Shinohara, T. Kanazawa, E. Araki, and K. Suyehiro 2009. Seismic Evidence for Sharp Lithosphere-Asthenosphere Boundaries of Oceanic Plates. *Science 324*(5926), 499–502.

Kelemen, P. B., and E. Aharonov 1998. Periodic formation of magma fractures and generation of layered gabbros in the lower crust beneath oceanic spreading ridges. *Geophysical monograph* **106**, 267–289.

Lange, R. L., and I. S. E. Carmichael 1990. Thermodynamic properties of silicate liquids with emphasis on density, thermal expansion and compressibility. *Reviews in Mineralogy and Geochemistry 24*(1), 25–64.

Lawn, B. R. 1993. *Fracture of brittle solids.* Cambridge Univ Pr.

Li, X., R. Kind, X. Yuan, I. Wlbern, and W. Hanka 2004. Rejuvenation of the lithosphere by the Hawaiian plume. *Nature 427*(6977), 827–829.

Lister, J. R. 1990. Buoyancy-driven fluid fracture: the effects of material toughness and of low-viscosity precursors. *Journal of Fluid Mechanics* **210**, 263–280.

Lister, J. R., and R. C. Kerr 1991. Fluid-Mechanical Models of Crack Propagation and Their Application to Magma Transport in Dykes. *J. Geophys. Res. 96*(B6), 10049–10077.

MATLAB 2010. *version 7.10.0 (R2010a).* Natick, Massachusetts: The MathWorks Inc.

McHone, J. G., D. L. Anderson, E. K. Beutel, and Y. A. Fialko 2005. Giant dikes, rifts, flood basalts, and plate tectonics: A contention of mantle models. *Geological Society of America Special Papers* **388**, 401–420.

McKenzie, D. 1984. The Generation and Compaction of Partially Molten Rock. *Journal of Petrology 25*(3), 713–765.

Menzies, M. A., S. L. Klemperer, C. J. Ebinger, and J. Baker 2002. Characteristics of volcanic rifted margins. *Geological Society of America Special Papers* **362**, 1–14.

Mériaux, C., and C. Jaupart 1998. Dike propagation through an elastic plate. *J. Geophys. Res.* **103**, 18295–18314.

Morgan, J. 1983. Hotspot tracks and the early rifting of the Atlantic. *Tectonophysics 94*(1-4), 123–139.

Morgan, W. J. 1971. Convection Plumes in the Lower Mantle. *Nature 230*(5288), 42–43.

Nicolas, A., and M. Jackson 1982. High Temperature Dikes in Peridotites: Origin by Hydraulic Fracturing. *Journal of Petrology 23*(4), 568–582.

Pollard, D. D. 1976. On the form and stability of open hydraulic fractures in the earth's crust. *Geophysical Research Letters 3*(9), 513–516.

Qin, R., and W. R. Buck 2008. Why meter-wide dikes at oceanic spreading centers? *Earth and Planetary Science Letters 265*(3-4), 466–474.

Renner, J., B. Evans, and G. Hirth 2000. On the rheologically critical melt fraction. *Earth and Planetary Science Letters 181*(4), 585–594.

Renner, J., K. Viskupic, G. Hirth, and B. Evans 2003. Melt extraction from partially molten peridotites. *Geochem. Geophys. Geosyst. 4*(5).

Roper, S., and J. Lister 2005. Buoyancy-driven crack propagation from an overpressured source. *Journal of Fluid Mechanics 536*(1), 79–98.

Royden, L., J. Sclater, and R. V. Herzen 1980. Continental margin subsidence and heat flow: important parameters in formation of petroleum hydrocarbons. *Bull. Am. Assoc. Pet. Geol.* **64**, 173–187.

Rubin, A. M. 1993. Tensile fracture of rock at high confining pressure: implications for dike propagation. *Journal of Geophysical Research 98*(B9), 15919–15.

Rubin, A. M. 1995. Propagation of Magma-Filled Cracks. *Annual Review of Earth and Planetary Sciences 23*(1), 287–336.

Rubin, A. M. 1998. Dike ascent in partially molten rock. *Journal of Geophysical Research 103*(20), 901–20.

Rychert, C. A., K. M. Fischer, and S. Rondenay 2005. A sharp lithosphere-asthenosphere boundary imaged beneath eastern North America. *Nature 436*(7050), 542–545.

Rychert, C. A., J. O. Hammond, N. Harmon, J. M. Kendall, D. Keir, C. Ebinger, I. D. Bastow, A. Ayele, M. Belachew, and G. Stuart 2012. Volcanism in the Afar Rift sustained by decompression melting with minimal plume influence. *Nature Geoscience 5*(6), 406–409.

Rychert, C. A., and P. M. Shearer 2009. A Global View of the Lithosphere-Asthenosphere Boundary. *Science 324*(5926), 495–498.

Rychert, C. A., and P. M. Shearer 2011. Imaging the lithosphere-asthenosphere boundary beneath the Pacific using SS waveform modeling. *J. Geophys. Res. 116*(B7).

Schmerr, N. 2012. The Gutenberg Discontinuity: Melt at the Lithosphere-Asthenosphere Boundary. *Science 335*(6075), 1480–1483.

Schwenn, M. B., and C. Goetze 1978. Creep of olivine during hot-pressing. *Tectonophysics 48*(1–2), 41–60.

Scott, D. R., and D. J. Stevenson 1984. Magma solitons. *Geophys. Res. Lett. 11*(11), 1161–1164.

Scott, T., and D. L. Kohlstedt 2006. The effect of large melt fraction on the deformation behavior of peridotite. *Earth and Planetary Science Letters 246*(3–4), 177–187.

Simpson, G., M. Spiegelman, and M. I. Weinstein 2010. A multiscale model of partial melts: 2. Numerical results. *J. Geophys. Res. 115*(B4).

Sleep, N. H. 1988. Tapping of melt by veins and dikes. *Journal of Geophysical Research 93*(B9), 10255–10.

Sparks, D. W., and E. M. Parmentier 1991. Melt extraction from the mantle beneath spreading centers. *Earth and Planetary Science Letters 105*(4), 368–377.

Spence, D., and D. Turcotte 1985. Magma-driven propagation of cracks. *Journal of Geophysical Research 90*(B1), 575–580.

Spiegelman, M. 1993. Physics of melt extraction: Theory, implications and applications. *Philosophical Transactions of the Royal Society of London. Series A: Physical and Engineering Sciences 342*(1663), 23–41.

Stevenson, D. J. 1989. Spontaneous small-scale melt segregation in partial melts undergoing deformation. *Geophys. Res. Lett. 16*(9), 1067–1070.

Tan, Y., and D. V. Helmberger 2007. Trans-Pacific upper mantle shear velocity structure. *J. Geophys. Res. 112*(B8).

Tucholke, B. E., M. D. Behn, W. R. Buck, and J. Lin 2008. Role of melt supply in oceanic detachment faulting and formation of megamullions. *Geology 36*(6).

Turcotte, D., and G. Schubert 2002. *Geodynamics* (2 ed.). New York, N.Y.: Cambridge University Press.

Van Leer, B. 1977. Towards the ultimate conservative difference scheme. IV. A new approach to numerical convection. *Journal of Computational Physics 23*(3), 276–299.

Wark, D. A., and E. B. Watson 1998. Grain-scale permeabilities of texturally equilibrated, monomineralic rocks. *Earth and Planetary Science Letters 164*(3-4), 591–605.

White, R. S., G. D. Spence, S. R. Fowler, D. P. McKenzie, G. K. Westbrook, and A. N. Bowen 1987. Magmatism at rifted continental margins. *Nature 330*(6147), 439–444.

Whitmarsh, R. B., G. Manatschal, and T. A. Minshull 2001. Evolution of magma-poor continental margins from rifting to seafloor spreading. *Nature 413*(6852), 150–154.

Wong, T.-F., S.-C. Ko, and D. L. Olgaard 1997. Generation and maintenance of pore pressure excess in a dehydrating system 2. Theoretical analysis. *J. Geophys. Res. 102*(B1), 841–852.

Wright, T. L., and F. W. Klein 2006. Deep magma transport at Kilauea volcano, Hawaii. *Lithos 87*(1–2), 50–79.

Yuan, H., and B. Romanowicz 2010. Lithospheric layering in the North American craton. *Nature 466*(7310), 1063–1068.

2.10 Tables and Figures

Symbol	Value or Definition	Description
a	1 cm	grain size
g	9.8 m s^{-2}	gravitational acceleration
H	$3 \cdot 10^5$ J/kg	latent heat of crystallization
K_c	1 MPa $m^{1/2}$ [1]	critical stress intensity factor
M	50 GPa [1]	elastic stiffness
T_m	1200^{o}C	solidus temperature
β	10^{-10} Pa^{-1}	composite fluid and solid compressibility
$\Delta\rho$	300 kg m^{-3}	difference between solid and fluid density
η	10^{19} Pa s	solid shear viscosity
κ	10^{-6} m^2 s^{-1}	thermal diffusivity
μ_f	1, 10 Pa s	fluid viscosity
ρ_f	3000 kg m^{-3}	fluid density
σ	5, 10 MPa	tectonic deviatoric stress
ϕ_o	0.01-0.05	reference background porosity
ϕ_{RCMF}	0.25 [2]	rheologically critical melt fraction

Table 2.1: Alphabetical list of constants and reference scales with definitions or values used and description. References: [1] Rubin (1995), [2] Scott and Kohlstedt (2006).

Symbol	Definition	Description
D	$\frac{k}{\phi\mu_f\beta}$	pressure diffusivity
h		crack height
k	$\frac{a^2\phi^3}{300}$	permeability
L		lithosphere thickness
P		excess pressure
P_d		dike base excess pressure
Q		crack volume flux
r		radial source region coordinate (Figure 2.1c)
T		temperature
t		time
w		crack width
z		height above LAB
λ		freezing front similarity constant
ξ	$\eta\phi^{-1}$	bulk (compaction) viscosity
ϕ		porosity

Table 2.2: Variables and coordinates

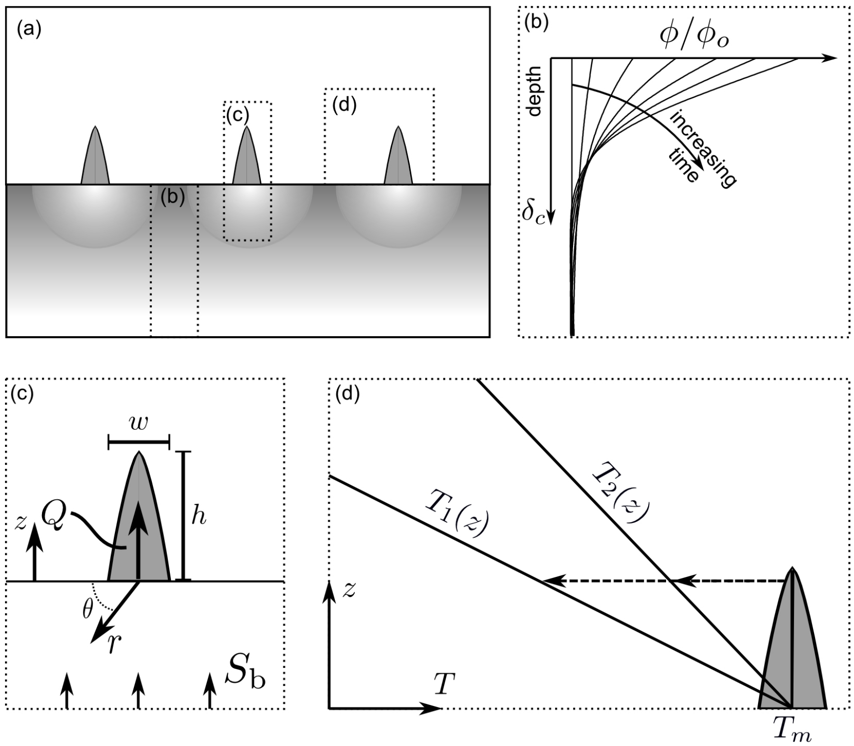

Figure 2.1: The accumulation of melt at the lithosphere-asthenosphere boundary and subsequent penetration of melt into the lithosphere (inset a) is controlled by the interaction of the processes illustrated in insets b-d. (b) Melt formed in the asthenosphere rises buoyantly by porous flow and accumulates beneath a freezing boundary in a decompacting boundary layer. ϕ_o is the reference background melt fraction and δ_c is the reference compaction length. For ϕ_o=0.01 and typical parameters in table 1, $\delta_c \approx 20$ km. (c) If the excess pressure is sufficiently high, dikes may propagate into the lithosphere. The growth rate and ultimate volume of a dike is limited by the rate at which fluid can move into the dike as well as the supply rate of new fluid into the decompacting boundary layer, $S_\mathrm{b}=(1-\phi_o)\Delta\rho g k(\phi_o)/\mu$. (d) The extent of dike propagation is limited by the freezing rate, which depends on the horizontal temperature gradient at each height in the dike. A geotherm with a larger gradient, $T_1(z)$, results in a larger freezing rate than a geotherm with a smaller gradient, $T_2(z)$.

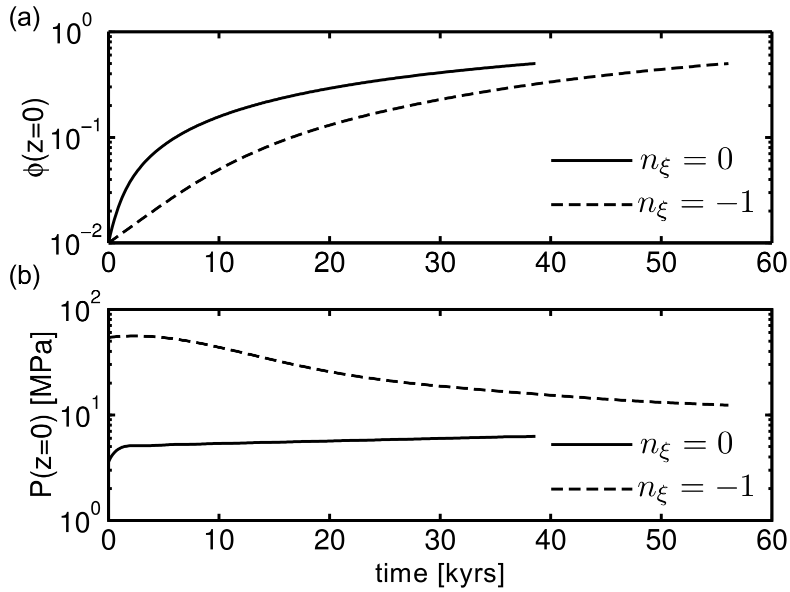

Figure 2.2: Evolution at the top of a decompaction boundary layer using a background melt fraction of 0.01 and the reference values in table 1. (a) Melt fraction and (d) excess pressure for a compaction viscosity that is independent (dashed curve) of melt fraction and inversely dependent on melt fraction (solid curve).

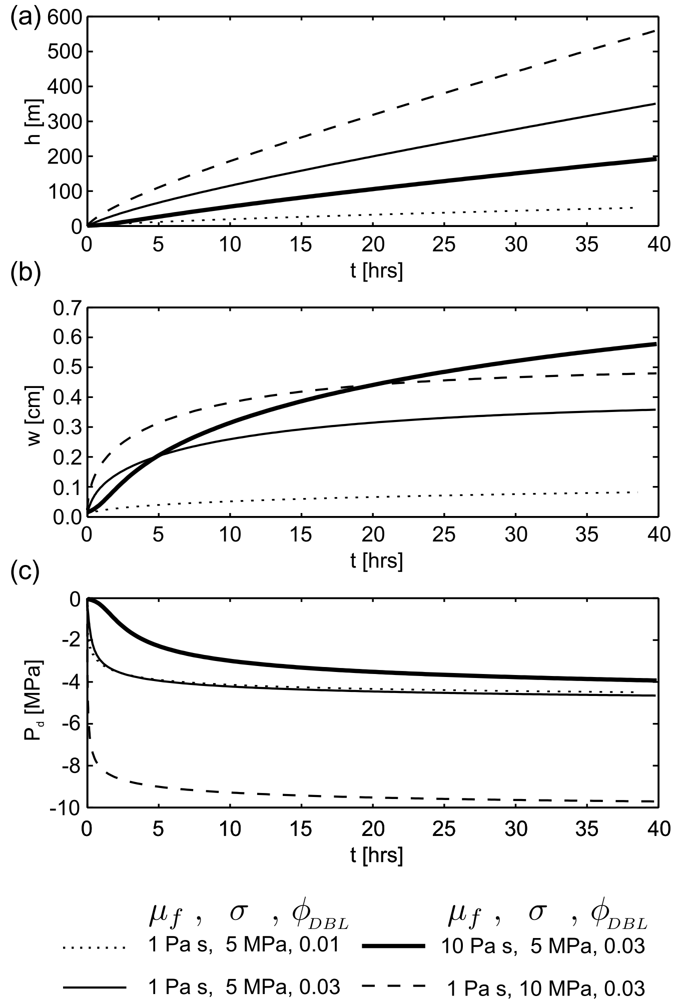

Figure 2.3: Dike propagation from a porous source limited by pressure diffusion. (a) Height, (b) width and (c) excess pressure at the dike base for various source porosities, ϕ_{DBL}, tectonic stresses σ and dike melt viscosities μ_f.

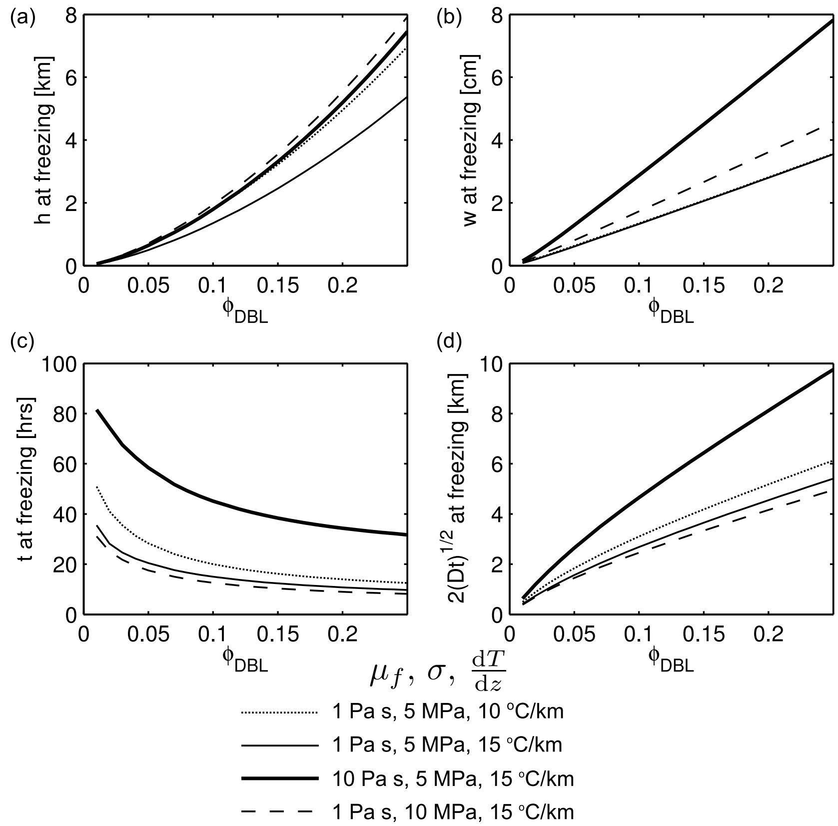

Figure 2.4: Source porosity control on (a) final height at freezing, (b) final width at freezing, (c) time at freezing and (d) diffusion front extent at freezing for various tectonic stresses σ and dike melt viscosities μ_f.

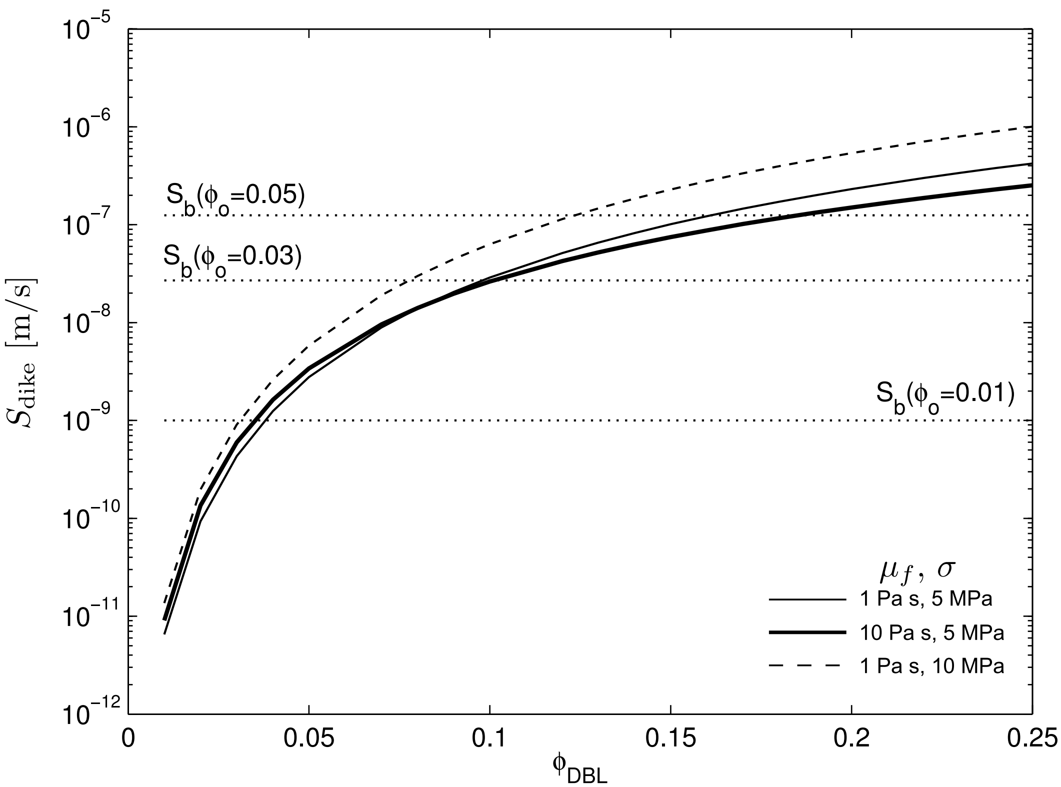

Figure 2.5: The volumetric flow rate out of a decompacting boundary layer at the LAB due to diking, S_{dike} for various tectonic stresses σ and fluid viscosities μ_f. Also plotted as horizontal dotted lines is the buoyant flux into a DBL, $S_{\mathrm{b}}=(1-\phi_o)\Delta\rho g k(\phi_o)/\mu$ for fixed upwelling melt fraction of 0.01, 0.03 and 0.05. The total melt in a DBL is expected to increase when $S_{\mathrm{dike}}<S_b$.

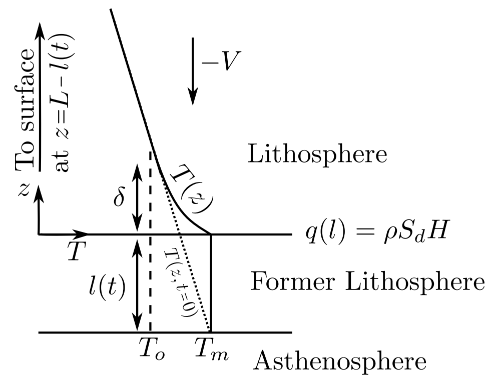

Figure 2.6: Schematic depiction of lithosphere thinning. The lithosphere of initial thickness, L is heated at its base by a planar heat source, q, due to the freezing of dikes intruding at a rate S_d and releasing heat per volume of $H\rho$. The vertical coordinate, z, is fixed to the T=T_m isotherm so that the lithosphere moves past the LAB at an apparent velocity, $-V$. In front of the LAB, a thermal boundary layer extends a distance δ beyond the current location of the LAB. The total amount of thinning is the distance the LAB has moved, $l(t)$. ΔT in the text is the difference between T_m and T_o, the temperature at the point where the geotherm is unaffected by the thermal boundary layer δ.

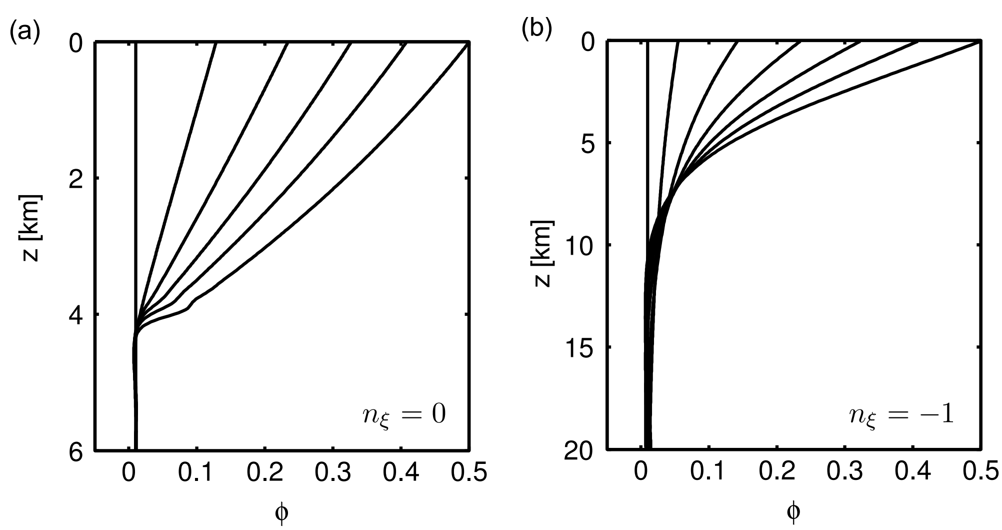

Figure 2.7: Evolution of a decompacting boundary layer with no diking (impermeable boundary) for a compaction viscosity of $\xi = \phi^{n_\xi}$ with (a) $n_\xi = 0$ and (b) $n_\xi = -1$. The porosity dependent case shows a much thicker DBL because the compaction length scales with the square root of ξ.

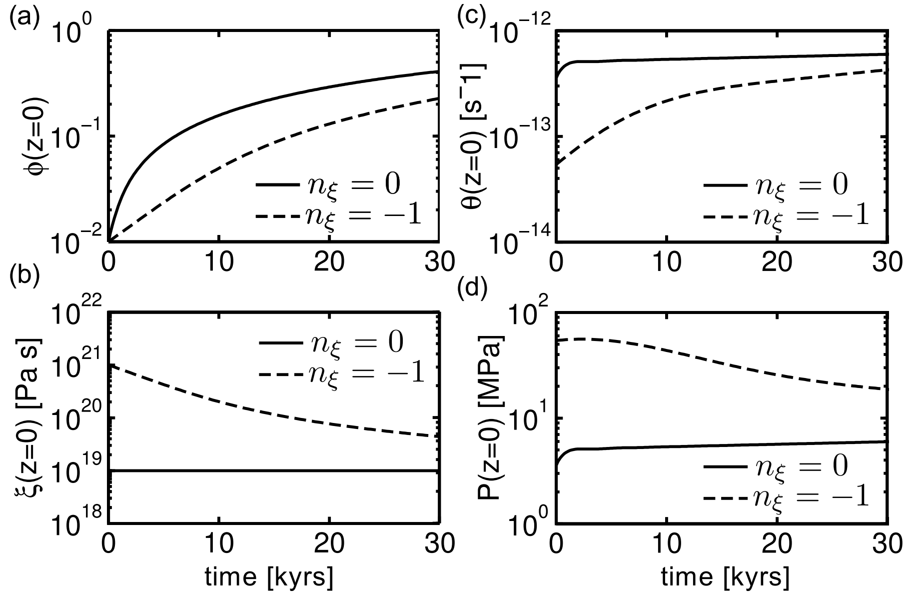

Figure 2.8: Evolution of porosity, ϕ, compaction viscosity, $\xi = \eta\phi^{n_\xi}$, dilatation rate, θ, and excess pressure P at the top of a DBL with no diking (impermeable boundary).

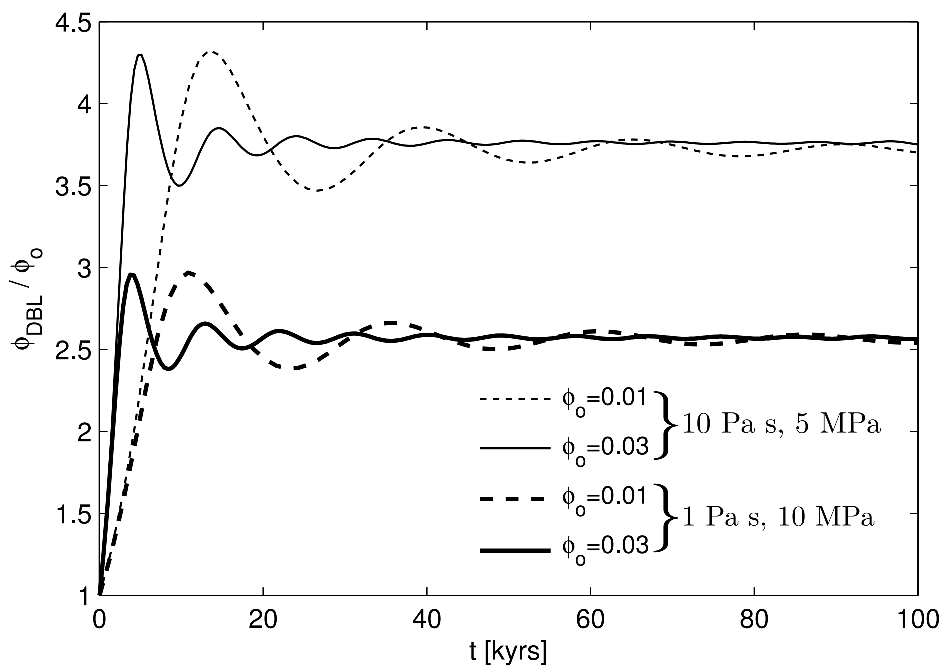

Figure 2.9: Time evolution of melt fraction at the top of a DBL, ϕ_{DBL}, compared to the reference buoyant melt fraction, ϕ_o, for a DBL with diking. The boundary condition at the LAB is time dependent and set by $S_{\text{dike}}(\phi_{DBL})$ in Figure 2.5. After a few kyrs, ϕ_{DBL} oscillates with decreasing amplitude about a mean melt fraction consistent with the expected steady state ϕ_{DBL} from Figure 2.5.

Chapter 3 | Melt Migration Beneath Thinning Lithosphere

C. Havlin[1], **E.M. Parmentier**[1], **and G. Hirth**[1].

1. Department of Earth, Environmental and Planetary Science, Brown University, Providence, RI 02912, USA

In preparation for submission.

3.1 Abstract

In this study, we investigate how diking at the lithosphere-asthenosphere boundary (LAB) may influence the thermal and mechanical evolution of the lithosphere. Because of the importance of magmatic heat transfer and magmatic strain accommodation in continental rifts (e.g. Royden *et al.*, 1980; Bialas *et al.*, 2010; Ebinger and Casey, 2001) and the correlation between hot spot volcanism and rifting (e.g. Morgan, 1981, 1983; Nyblade and Robinson, 1994), we consider the case where melt is generated by adiabatic decompression in a mantle plume beneath thick lithosphere subject to an extensional tectonic force. We construct a basic state model in which the heat flux from the asthenosphere into the lithosphere is the sum of heat fluxes from vertical melt transport and (parameterized) small scale convection. The heat flux is used in solving for the temperature, deformation and thinning of the lithosphere. We then use the resulting LAB topography and lithosphere stress in 2-D calculations of melt migration in the asthenosphere subject to a diking flux (Havlin *et al.*, 2013) along the LAB in order to evaluate the potential for 2-D geometrical focusing to modify lithosphere thinning and melt accumulation.

We find that basal heating by melt infiltration results in thermal thinning at rates faster than heat conduction alone (tens of km/Myr). Amplification of stress in the remaining lithosphere is sufficient to trigger surface extension with little to no evidence of magmatic activity, which has implications for the strain accommodation in developing rift basins (Ebinger and Casey, 2001) where extension first occurs along basin-bounding normal faults and then transfers to narrow magmatic segments. The time between extension onset and mantle lithosphere erosion matches the time between extension onset and magmatic segmentation in the Central Main Ethiopian Rift (Ebinger and Casey, 2001) for a friction coefficient between 0.12 and 0.36. Rather than invoke fault weakening due to elevated pore pressure and whole-lithosphere hy-

dration to explain a coefficient of friction lower than 0.6 (e.g. Moresi and Solomatov, 1998), we view the low friction coefficient as a result of dynamic earthquake rupture, which can induce failure on large areas of a fault at stresses significantly lower than the Byerlee stress (e.g. Noda and Lapusta, 2013), resulting in a lower effective coefficient of friction on tectonic time-scales.

In addition to tectonic implications, our results offer insight into dynamics of melt accumulation at the base of the lithosphere. Our results show that diking at the LAB limits horizontal melt transport along a sloping LAB, which may explain the apparent lack of magma mixing over short length scales observed in the Central Main Ethiopian Rift (Rooney, 2010; Rooney *et al.*, 2011, 2014). For the parameter range tested, we did not find any conditions for which melt accumulates to close to the disaggregation limit ($\sim$0.25, Scott and Kohlstedt (2006)), implying that whole-lithosphere heating by magmatic intrusion (Bialas *et al.*, 2010) is limited to cases of exceptional melt production such as in the arrival of a plume head at the base of the lithosphere. And finally, lithosphere thinning rates calculated here are similar to those inferred from thermobarometry of xenoliths and melt inclusions in the Big Pines Volcanic Field in the western U.S. (Gazel *et al.*, 2012), corroborating the possible presence of a melt-rich boundary layer at the base of the lithosphere. Finally, our 2-D melt distributions are consistent with the hypothesis that melt accumulating at its solidus produces the strong negative seismic velocity gradients observed near the base of the lithosphere. Our results predict that a high melt fraction boundary layer will persist throughout rifting as observed in the Salton Trough (Lekic *et al.*, 2011) and the Rio Grande (**?**). While the absence of a phase beneath the Hawaii (Rychert *et al.*, 2013) and Yellowstone (Hopper *et al.*, 2014) hotspots requires some additional process of melt focusing, our results suggest that a negative phase is not observed beneath the Main Ethiopian Rift (Rychert *et al.*, 2012) because melt can migrate by porous flow most of the way to the crust.

3.2 Introduction

Early studies of magmatism at rifts primarily considered melt generation and eruption a byproduct of rifting (e.g. McKenzie and Bickle, 1988; White and McKenzie, 1989), but magmatism may influence continental rifting in several ways. In general, the transfer of melt from the asthenosphere to the lithosphere transports heat that can thermally weaken the lithosphere (e.g. Royden *et al.*, 1980). The heating reduces the lithosphere yield stress and subsequently lessens the tectonic force required for extension (Bialas *et al.*, 2010). In addition to thermal weakening, the accumulation and infiltration of melt facilitates strain localization and lithospheric rupture (Ebinger, 2005). In East Africa, rifting tends to initiate along compositional heterogeneities (Dunbar and Sawyer, 1989; Theunissen *et al.*, 1996). Initially, strain is accommodated by extension along basin-bounding normal faults in the presence of diffuse volcanic activity (Ebinger and Casey, 2001). As a rift basin matures, the locus of strain shifts from the border faults to narrow magmatic segments (Ebinger and Casey, 2001) where dike intrusion accommodates the majority of extension (Bilham *et al.*, 1999; Ebinger and Casey, 2001; Keir *et al.*, 2006). Typically, studies adopt a top-down view where extension thins the lithosphere, which creates topography along the base of the lithosphere and generates melt by adiabatic decompression (e.g. Ebinger and Casey, 2001). As thinning progresses, the increasing topography along the lithosphere-asthenosphere boundary diverts melt up-slope towards the rift axis until sufficient melt accumulates for magmatic intrusions to accommodate a large fraction of strain in the basin.

Most studies on the influence of melt in rift zones neglect the generation, migration and accumulation of melt in the asthenosphere by parameterizing the melt supply at the base of the lithosphere. One notable exception is the model of Schmeling (2010), which included melt generation and two phase flow beneath rifting lithosphere.

Schmeling (2010) concluded that melt primarily influences local buoyancy, resulting in increased mantle upwelling velocities and higher rift flank uplift due to the low density of melt. In a following study, Schmeling and Wallner (2012) investigated the impact of intrusional heating and found that the impact of intrusional heating depends on the depth range of melt intrusion and the lateral focusing of melt in the asthenosphere. While insightful, these studies simplify the two-phase system by assuming equal pressure in the fluid and solid, which ignores the effect of decompaction and compaction.

Decompaction of the solid matrix may influence the accumulation and transport in several ways. Sparks and Parmentier (1991) showed that melt collecting beneath the solidus-geotherm intersection generates a decompacting boundary layer of high melt fraction, creating a high permeability channel that can focus melt up-slope. Additionally, excess pressures in a decompacting boundary layer can be sufficiently high to generate dikes, relieving melt overpressure and locally heating the lithosphere near its base (Havlin *et al.*, 2013). One of the goals of this study is to evaluate the extent of lateral melt focusing and dike intrusion in a decompacting boundary layer at the base of the lithosphere.

In addition to better understanding how melt infiltration may influence rift evolution, studying the accumulation of melt at the base of the lithosphere may offer insight into the origin of the rapid decrease in seismic velocity observed near the expected base of the lithosphere (e.g. Fischer *et al.*, 2010). The origin of the negative velocity gradient is uncertain, but two main hypotheses are typically discussed in the literature; the negative velocity gradient could arise from melt collecting beneath its solidus (e.g. Kawakatsu *et al.*, 2009) or from the transition from anhydrous, depleted lithosphere to hydrated, fertile asthenosphere (Karato and Jung, 1998). A number of studies in regions influenced by volcanism provide valuable insight into the possible origin of the negative velocity gradient near the base of the lithosphere and we briefly review the observations here. In many receiver function studies, the negative phase is often referred to as the lithosphere-asthenosphere boundary (LAB) phase, but here we use a more general nomenclature and refer to the receiver function phases originating from near the base of the lithosphere simply as a negative phase.

A negative phase originating near the base of the lithosphere occurs in the vicinity of hotspots that have been studied. Beneath the Hawaiian hotspot (Rychert *et al.*, 2013) a strong decrease in seismic velocity is observed at depths of $\sim 70-80$ km, except for a noticeable gap 100-200 km wide in the vicinity of the volcanic axis but offset by about 100 km. The Galapagos hotspot shows a fairly continuous negative phase at a similar depth to Hawaii ($\sim$70 km), with a deepening in direction of plate motion from 66-80 km (Rychert *et al.*, 2014). Along the Snake River Plain, a negative phase was identified at $\sim$50 (Levander and Miller, 2012) or $60-70$ km (Hopper *et al.*, 2014). In both studies (Levander and Miller, 2012; Hopper *et al.*, 2014), there is no obvious negative phase beneath Yellowstone. Though not a hotspot, the shallowest and strongest negative phases in the eastern Phanerozoic accreted terrain of Australia occur beneath regions of high heat flow and recent Cenozoic volcanism (Ford *et al.*, 2010).

Extensional environments also record a strong negative velocity gradient near the expected base of the lithosphere. The Salton Trough, a trans-tensional basin that in the western U.S. where magmatic intrusion may have replaced a large fraction of the crust (e.g., Fuis *et al.*, 1984; Schmitt and Vazquez, 2006), shows a negative phase at a relatively constant depth of $\sim$40 km that deepens to $\sim$70 km on the basin flanks over a horizontal distance of less than 50 km (Lekic *et al.*, 2011). The Rio Grande Rift exhibits a shallow $\sim$50 km negative phase, similar to the rest of the Basin and Range (Lekic and Fischer, 2013). In the highly magmatic Main Ethiopian Rift, a strong decrease in seismic velocity is observed at $\sim 70-80$ km depth beneath the rift flanks, but the negative phase is noticeably absent directly beneath the rift (Rychert *et al.*, 2012). Farther south along the East African Rift, two negative phases are observed (Wolbern *et al.*, 2012). The shallow phase is observed beneath the Albertine Rift at 50 km depth while beneath the rift flanks and adjacent Tanzanian craton, the negative phase deepens to 80-100 km (Wolbern *et al.*, 2012). The deeper negative phase occurs at 140 km depth beneath the rift and between 200-220 km beneath the Tanzanian Craton. The deeper phase is similar to the base of the high velocity lid as measured by surface waves (Weeraratne *et al.*, 2003) and Wolbern *et al.* (2012) interpret the shallow negative phase as a melt-infiltration front and the deep negative phase as the base of the lithosphere.

In the following, we describe plume-induced lithosphere heating from convective destabilization and melt infiltration (Section 3.2.1). In Section 3.2.2 we summarize the results from Havlin *et al.* (2013) and present an updated calculation that better shows the dependence of diking at the LAB on lithosphere stress. In Section 3.3, we describe the components of our model, which includes melt migration in the asthenosphere (Section 3.3.2), energy conservation in the lithosphere (Section 3.3.1) and a force-conservation model of lithosphere deformation (Section 3.3.1). Section 3.4.1 shows that lithosphere thinning by basal heating from melt infiltration can amplify stress in the remaining lithosphere and trigger extension of typical continental lithosphere in 5-20 Myrs (depending on model parameters). 2-D melt migration calculations using the LAB topography and stress from the thermal-mechanical model and the diking flux of Havlin *et al.* (2013) as a boundary condition along the sloping LAB reveal that melt streamlines remain mostly vertical and melt fractions remain around a few percent (Section 3.4.2).

In the discussion (Section 3.5), we show that the time between onset of mechanical extension and erosion of the mantle lithosphere predicted by the model can reproduce the observed time between basin formation and magmatic segmentation in the Central Main Ethiopian Rift for melt productivity consistent with regional mantle potential temperatures and a friction coefficient for brittle faulting less than ∼0.36. A low friction coefficient supports the view that on tectonic time scales, the brittle strength of rock is effectively limited by dynamic earthquake rupture (Noda and Lapusta, 2013). We also show that our calculated 2-D melt distributions are consistent with the lack of lateral magma mixing beneath volcanoes in the Central Main Ethiopian Rift (Rooney, 2010; Rooney *et al.*, 2011) and the shallowing of a magma accumulation zone in the Big Pines Volcanic Field in the western U.S. (Gazel *et al.*, 2012). And finally, we discuss our results in the context of receiver function observations beneath volcanic and extensional regions. Our results seem consistent with the hypothesis that melt accumulating at its solidus produces the strong negative seismic velocity gradients observed near the base of the lithosphere.

3.2.1 Lithosphere Heating from Mantle Plumes

As a plume impinges on the base of the lithosphere (Figure 3.1), it spreads laterally as a viscous gravity current (Olson and Corcos, 1980; Huppert, 1982; Sleep, 1987; Bercovici and Lin, 1996). A number of numerical and theoretical studies have shown that as a hot plume impinges on the base of the lithosphere, small scale convective instabilities destabilize the bottom of the lithosphere (Yuen and Fleitout, 1985; Sleep, 1994; Moore *et al.*, 1998, 1999; Agrusta *et al.*, 2013) and the convective boundary layer is described by the scaling relationships initially determined for a cooling conductive lid (Davaille and Jaupart, 1993; Grasset and Parmentier, 1998). The convective heat flux supplied to the base of the lithosphere, q_c can be calculated using the scaling relationship of Davaille and Jaupart (1993)

$$q_c = -0.47 k_T (\rho \alpha g / \kappa \eta_s)^{1/3} \Delta T_v^{4/3}, \tag{3.1}$$

where k_T, ρ, α, g, κ, η_s and ΔT are the thermal conductivity (3 W m^{-1} K^{-1}), density (3300 kg m^{-3}), thermal expansivity (3×10^{-5} K^{-1}), gravitational acceleration (9.8 m^2 s^{-1}), thermal diffusivity (10^{-6} m^2 s^{-1}), viscosity of the convecting medium and the viscous temperature scale, respectively. The viscous temperature scale describes the sensitivity of viscosity to temperature changes and for a viscosity described by an Arrhenius temperature relationship is defined by (e.g. Grasset and Parmentier, 1998)

$$\Delta T_v = \frac{RT^2}{Q}, \tag{3.2}$$

where R is the universal gas constant (8.314 J mol^{-1} K^{-1}), T is temperature (in Kelvin) below the thermal boundary layer and Q is activation energy. For a typical plume excess temperature of 150°C, activation energy for olivine of 5×10^5 J mol^{-1}, and a viscosity of 10^{21} Pa s at 1200^{o}C, the convective heat flux into the lithosphere base is on the order of 50 mW m^{-2}.

As a plume upwells, a portion of its energy is partitioned into generating melt. While the energy carried by migrating melt is small compared to the total heat transported into the upper mantle by a plume (Sleep, 1990), the heat flux into the lithosphere due to infiltrating melt may be comparable to the conductive heat flux estimated above. As a first calculation, consider a 1-D, steady state melting column. At steady state, the porosity in the melting column does not evolve so that the flux of melt out the top of the column, S_d, must equal the integral of the melt generation rate, $\dot{\Gamma}$, over the column height:

$$S_d = \int_{z_1}^{z_2} \dot{\Gamma} \mathrm{d}z, \tag{3.3}$$

where z_1 is the melting onset depth and z_2 is the top of the melting column and $z = 0$

at the base of the melting column and increases upwards. Because the melt and solid temperatures are equal for melt migrating by porous flow, the excess advective heat flux carried by the melt is $\rho_f L S_d$, where ρ_f and L are melt density (2700 kg m^{-3}) and latent heat (500 kJ kg^{-1}). For adiabatic decompression melting, the melting rate is given by the product of the solid upwelling velocity, V_z^s, and melt productivity $\mathrm{d}F/\mathrm{d}z$: $\dot{\Gamma} = V_z^s \mathrm{d}F/\mathrm{d}z$. Taking a constant upwelling rate of 20 cm/yr, a constant melt productivity of 1.5×10^{-3} km^{-1} (i.e., 15% melting in 100 km), and a melting column thickness of 100 km yields an energy flux of 1.3 W m^2, implying that if melt efficiently infiltrates the lithosphere the associated heat flux could locally exceed the convective heat flux from a hot plume.

While similar in magnitude, the convective heat flux and melt heat flux have significantly different spatial distributions. Most melt in an upwelling plume is generated in the upwelling conduit where decompression rate is greatest. While small scale convection can result in secondary melting (Ballmer *et al.*, 2007, 2011; Agrusta *et al.*, 2013), the melting rate is highest near the plume axis (Bianco *et al.*, 2008, 2011) and drops off rapidly with distance from the plume axis (figure 3.1b). The convective heat flux, however, varies over a much larger spatial scale. Hot plume material can spread on the order of 1000 km from the plume axis (e.g. Ribe and Christensen, 1994; Bercovici and Lin, 1996). Calculations of the average temperature and thickness of pancaking plume material (Bercovici and Lin, 1996) show that the average temperature drops off with a decay length scale of 500 km. Similarly, the lithosphere thinning of ~50 km spread over 800 km observed by (Moore *et al.*, 1999) implies that the convective heat flux decays at a similar length scale. The important point is that the convective heat flux into the lithosphere base will be relatively constant over the shorter melt heat flux length scale (figure 3.1b).

3.2.2 Melt Infiltration

Motivated by seismic observations that show a rapid decrease in seismic velocity near the expected base of the lithosphere (e.g. Rychert *et al.*, 2005; Kawakatsu *et al.*, 2009; Schmerr, 2012), which could be generated by melt accumulating beneath its solidus, we previously investigated the propagation of dikes from a partially molten boundary layer at the base of the lithosphere (Havlin *et al.*, 2013). In this section, we briefly review the physical basis and important conclusions relevant to the present study.

The first important result from Havlin *et al.* (2013) is that the excess pressure generated in a partially molten boundary layer in the absence of diking can easily reach a few MPa well before enough melt accumulates for the solid matrix to disaggregate (∼0.25 Scott and Kohlstedt (2006)). At an excess pressure of a few MPa, stress concentrations around a crack tip would cause flaws only a few cm long to grow; for a crack length of h_c, the critical effective pressure for propagation is given by $\sim K_c/\sqrt{h_c}$ (e.g. Lawn, 1993) where the critical stress intensity factor, K_c, is equal about 1 MPa m$^{-1/2}$ for rocks (e.g. Rubin, 1995). Thus, small flaws in a partially molten boundary layer would be critically unstable and grow. While we did not treat the initial nucleation of flaws, possible origins include micro-cracking (Cai and Bercovici, 2013) or grain boundary triple junctions (Rubin, 1998).

The time scale for melt migration in a viscously deforming, porous medium is orders of magnitude greater than the elastic time scale of a propagating dike. Thus to couple the propagation of dikes to a partially molten zone of melt accumulation at the base of the lithosphere, we considered the propagation of a dike from a compressible poro-elastic source region (e.g. Brace *et al.*, 1968; Wong *et al.*, 1997) where the permeability of the source region is constant on the time scale of a single dike and determined by accumulation of melt by porous flow.

Similar to other studies of dike propagation in the partially molten mantle (Sleep, 1988; Fowler and Scott, 1996; Rubin, 1998), we found that dikes do not exceed a few cm in width. Such narrow dikes would freeze rapidly as they intrude into the lithosphere, but repeated intrusions could locally heat the lithosphere allowing subsequent dikes and migrating melt to move higher into the lithosphere. In order to calculate a time-averaged flux of melt across the LAB due to dikes, we calculated the width, height, elapsed growth time and spacing of dikes for a suite of controlling parameters. The average volumetric flow rate due to diking, is then $S_d = (\text{width} \times \text{height})/(\text{growth time} \times \text{spacing})$. The dike dimensions (width, height) and growth time fall out directly from the calculations for a given source melt fraction, fluid viscosity, local geotherm and stress state. As dikes grow from a poro-elastic source, a radial pressure shadow extends into the source to an extent $\sqrt{Dt}$, where D is the pressure diffusivity of the source ($D \equiv k/\beta\eta_f$, with permeability k, effective source compressibility β and fluid viscosity η_f.). Thus, the extent of the pressure shadow when a dike freezes determines the minimum spacing for non-interacting dikes.

In figure 3.2a, we plot the time-averaged diking melt flux, S_d, against the melt fraction, ϕ, in a zone of melt accumulation at the base of the lithosphere, modified from figure 5 of Havlin *et al.* (2013). While not exact, the dependence of the diking melt flux, S_d, increases with roughly the cube of the melt fraction, reflecting the permeability of the source region ($k \propto \phi^3$).

In addition to the melt fraction of the source, the dike flux increases with increasing tectonic (deviatoric) stress. While the stress at the base of the lithosphere is likely small due to the high temperature and low viscosity, stress concentrations arising from lithosphere thinning could create local regions where diking is more efficient. Using the model from Havlin *et al.* (2013), we calculated the dike flux for a wider range of extensional tectonic stresses ($\sigma > 0$ in tension). Because the diking flux depends on a range of parameters, we introduce a nondimensional scale that we refer to as the diking efficiency parameter, defined as the ratio of the diking flux to the buoyant Darcy flux at the same melt fraction

$$D_k \equiv \frac{S_d}{S_b}, \tag{3.4}$$

where $S_b = \Delta\rho g k/\eta_f$, where $\Delta\rho$, g, k and η_f are the fluid-solid density difference, gravitational acceleration, permeability and fluid viscosity, respectively. When $D_k < 1$ (as it is in all cases here), the diking flux is smaller than the buoyant Darcy flux at the same melt fraction – this means that if melt is arriving at the base of the lithosphere at a rate $S_b(\phi_o)$ where ϕ_o is some reference melt fraction, then the melt fraction at the base of the lithosphere will increase until reaching a melt fraction ϕ_{LAB} at which the diking flux can balances the incoming melt (i.e., $S_d(\phi_{\mathrm{LAB}}) = D_k S_b(\phi_o)$), as shown in the Supplemental Material of Havlin *et al.* (2013). In any case, the additional calculations at a wider range of extensional tectonic stress show that for a fixed melt fraction, diking efficiency increases linearly with increasing stress (figure 3.2b). As a result, thinning of the lithosphere may influence dike propagation from the LAB by introducing geometrical focusing effects and by changing the available stress for diking.

The heat flux from freezing dikes near the base of the lithosphere is comparable to the convective heat flux described in section 3.2.1. Because dikes intrude near the base of the lithosphere where the temperature is close to the solidus of melt, latent heat release dominates the heat budget and the diking heat flux is simply $\rho_f L S_d$. For a partially molten boundary layer with $\phi = 0.03$, the diking heat flux is 1.4W m^{-2} (taking S_d from figure 3.2a and $\rho_f L$ from the previous section).

3.3 Model Setup and Methods

To investigate the role of heat flux due to melt infiltration in extensional environments, we use a suite of model components that describe the thermal and mechanical evolution of the lithosphere, melt migration in the asthenosphere and the coupling between the asthenosphere and lithosphere. We consider a basic state in which the melt flux into the base of the lithosphere is given by the vertically integrated melt production in the asthenosphere. The associated heat flux from melt production is used as a boundary condition to calculate the thermal mechanical evolution of lithosphere. Given the lithosphere-asthenosphere boundary topography and lithosphere stress state from the basic state model, we calculate 2-D melt distributions and melt velocities. We then calculate a melt infiltration heat flux that includes 2-D focusing effects and compare to the result to the imposed 1-D melt heat flux.

We calculate lithosphere thermal evolution (Section 3.3.1) by solving the transient heat equation and fixing the temperature at the lithosphere base at 1200^{o}C, based on geophysical observations as discussed in Section 3.3.1. The basal boundary migrates at a velocity determined by the local energy balance between conduction into the lithosphere and heat provided from the asthenosphere through melt infiltration and small scale convection. We treat mechanical deformation of the lithosphere (Section 3.3.1) in a simplified manner, assuming constant horizontal force and local pure shear to calculate horizontal strain rate. Thus the horizontal extension rate is a function of horizontal position and not a function of depth. The lithosphere rheology in the deformation model is temperature dependent so that locally hot or thinned regions tend to localize strain. Additionally, we couple the lithosphere deformation and thermal models by using the solid velocities from lithosphere deformation in the advective term of the heat equation.

At various stages of thermal and mechanical thinning, we pause the model to calculate the distribution of melt in the asthenosphere and evaluate the role of 2-D effects in modulating the melt infiltration heat flux. Because the time scale for melt migration in the asthenosphere is relatively short compared to the solid state deformation and thermal evolution of the lithosphere, we consider the boundary fixed on melt migration time scales and calculate a quasi steady state melt fraction distribution for a given lithosphere-asthenosphere topography and stress sate (Section 3.3.2). We experiment with a range of cases, using the diking parametrization described in Section 3.2.2 as a boundary condition so that the melt flux across the LAB depends on both the local melt fraction and the lithosphere stress state.

3.3.1 Lithosphere Evolution

Thermal Evolution

In this study, we define the base of the lithosphere as an isotherm, T_{LAB}C, and solve the two dimensional transient advection-diffusion equation for temperature with a prescribed heat flux from convective and intrusional components along the base of the lithosphere. To save computational expense, we calculate solutions about the symmetry plane x=0. Using an immersed boundary approach (see Supplementary Material), we enforce $T = T_{\mathrm{LAB}}$ along the lithosphere-asthenosphere boundary and advect the boundary with velocity calculated through an energy balance in the vicinity of the boundary. Additionally, we include advection of heat due to mechanical thinning (Section 3.3.1). The relevant governing equation and boundary conditions (figure 3.3) are

$$\frac{\partial T}{\partial t} = \kappa \nabla^2 T + \underline{V}^s \cdot \nabla T \tag{3.5}$$

$$T(x_{\mathrm{L}}, z_{\mathrm{L}}) = T_{\mathrm{LAB}}, \tag{3.6}$$

$$T(x, z{=}0) = 0^{\circ}\mathrm{C}, \ \left.\frac{\partial T}{\partial x}\right|_{x=0,\max(x)} = 0 \tag{3.7}$$

where T, $\underline{V}^s$ and κ are the temperature, solid velocity and thermal diffusivity, respectively. The points $(x_{\mathrm{L}}, z_{\mathrm{L}})$ define the boundary points.

We use a 1-D initial temperature field corresponding to a steady state plate model for continental lithosphere in which heat producing elements are concentrated in the crust (Turcotte and Schubert, 2002, p. 141). The adjustable parameters are the surface heat flux, the heat flux into the base of the lithosphere and the crustal thickness. Results shown here use a fixed surface heat flux of 50 mW m^2 and crustal thickness of 30 km. The heat flux into the base (varied from 20-30 mW m^{-2}) is the initial background heat flux used to calculate the initial condition, which is distinct from the heat flux imposed due to plume-lithosphere interaction and melt infiltration.

We fix the solidus temperature at T_{LAB}=1200°C, based loosely on geophysical observations and dynamics of convective instabilities. Several studies of receiver functions in subducting oceanic lithosphere in the Pacific observe a decrease in seismic velocity near the expected base of the lithosphere (Kawakatsu *et al.*, 2009; Kumar and Kawakatsu, 2011). The depth of the velocity drop roughly decreases with age of the subducting lithosphere, following a plate cooling model isotherm in the range of 900-1300°C (Kumar and Kawakatsu, 2011). Studies using SS precursors (Rychert and Shearer, 2011; Schmerr, 2012) observe a similar trend across the Pacific, though the age dependence is much less obvious (or perhaps nonexistant) when the different studies are compared in detail (Rychert *et al.*, 2012). For the observed velocity decrease to coincide with the base of the rigid lithosphere, the depth of the velocity decrease should occur in the vicinity of the viscosity increase that separates the convecting mantle from the rigid, conductive lithosphere. In studies of convective instabilities at the base of the lithosphere above a mantle plume, material at 1200-1300°C is typically sufficiently viscous to not participate in the underlying convection (e.g. Moore *et al.*, 1998, 1999; Agrusta *et al.*, 2013) and so we choose an isotherm on the upper range of that inferred from geophysical studies, T_{LAB}=1200°C.

The total heat flux, q, that drives lithosphere thinning is the sum of a heat flux due to small scale convection beneath the lithosphere,q_c, and the heat flux from infiltrating melt that freezes. We calculate a melt flux assuming 1-D, steady state melting at each point in x, and then later use the 2-D melt migration calculation to assess whether or not melt transport is mostly vertical. For 1-D, steady state melting, the flux out the top of a melting column is given by equation 3.3 so that the total heat flux is given by

$$q(x) = q_c + \rho_f L \int_{z_1}^{z_2} \dot{\Gamma}(x, z)\mathrm{d}z. \tag{3.8}$$

Because melt maintains thermal equilibrium with the solid in the asthenosphere and we are investigating the case where melt intrudes near its solidus temperature, we neglect the sensible heat advected by the melt and include only the latent heat in equation 3.8. The convective heat flux does not vary significantly over the region of primary melt production (see Section 3.2.1) and we use a constant q_c calculated by the scaling relationship given by equation 3.1 at a plume excess temperature of 150^{o}C. For a specified melting rate distribution, $\dot{\Gamma}(x, z)$ (see Section 3.3.2), we can then calculate $q(x)$ which we use to calculate a boundary velocity.

We calculate the boundary velocity by considering conservation of energy in the vicinity of the lithosphere-asthenosphere boundary in a fashion similar to Spohn and Schubert (1982). As the solidus isotherm moves upward, the heat required to raise the temperature from the solidus to the temperature of the convecting mantle is $\rho_s C_p \Delta T + \phi \rho_f L$, where ΔT is the difference in the convecting mantle temperature and the solidus temperature. The difference in the total heat flux into the lithosphere base, q (equation 3.8), and the conductive heat flux away from the boundary into the lithosphere supplies the heat to move the solidus. For a reference frame fixed to the solidus isotherm with n defining the unit normal direction, the energy balance that determines the boundary velocity, V_B, is

$$0 = k_T \frac{\partial T}{\partial n} - q(x) - \rho_s C_p \Delta T V_B \left(1 + \frac{\rho_f L \phi}{\rho_s C_p \Delta T}\right), \tag{3.9}$$

where k_T, ρ and C_p are thermal conductivity, density and specific heat, respectively. For a classical Stefan problem, ϕ=1, and the latent heat is a significant sink of energy. For the partially molten system here, $\phi < 1$ and reflects the melt fraction in the convective material below the lithosphere. For typical asthenospheric melt fractions of less than 0.05, a solidus temperature of 1200°C and a plume at 1450°C, $\frac{\rho_f L \phi}{\rho_s C_p \Delta T} < 0.08$ and so we neglect the latent heat term in the energy balance here and write the boundary velocity as

$$V_B = \frac{k_T \frac{\partial T}{\partial n} - q(x)}{\rho_s C_p \Delta T}. \tag{3.10}$$

A possibly important difference between our formulation and that of Spohn and Schubert (1982) is that we neglect the pressure dependence of the solidus and use a constant value. At this stage, the 2-D model is already fairly complex without this additional dependence, and so for now we neglect the pressure dependence of the solidus and note that the assumption of a constant solidus temperature should be re-evaluated in future studies.

Equation 3.10 describes the magnitude of the thinning rate normal to the LAB. In x, z coordinates, the components of the boundary velocity depend on the local boundary angle, θ (figure 3.3). Furthermore, the total thinning rate in the reference frame of the lithosphere is the sum of the solid velocities from deformation $\underline{V}^s$ (described in Section 3.3.1) and the boundary velocity from the local energy balance so that the total velocity of the boundary in x and z coordinates is given by

$$V_B^z = V_B\cos(\theta) + V_z^s, \tag{3.11}$$

$$V_B^x = V_B\sin(\theta) + V_x^s. \tag{3.12}$$

We solve the transient heat equation (3.5) using a finite volume discretization on a uniform mesh. For the advective term, we use a second order accurate, conservative slope-limiting advection scheme (Van Leer, 1977; Hourdin and Armengaud, 1999) and we step forward the temperature in time with an explicit forward difference. The temperature is fixed at the solidus along the lithosphere base using an immersed boundary method. Specifically, we follow the algorithm described by Tseng and Ferziger (2003) for enforcing Dirichlet boundary condition with a linear reconstruction with an image point method.

To calculate the boundary velocity, we approximate the conductive heat flux in the lithosphere using forward difference,

$$\frac{\partial T}{\partial n} \approx \frac{1}{\Delta n}\left(T(\Delta n) - T_{\mathrm{LAB}}\right). \tag{3.13}$$

The discrete approximation of the boundary velocity is then

$$V_B = \frac{\frac{k_T}{\Delta n}\left(T(\Delta n) - T_{\mathrm{LAB}}\right) - q(x_i)}{\rho C_p \Delta T}, \tag{3.14}$$

where x_i indicates the discrete horizontal position where the V_B is being evaluated. Because temperatures are defined at cell centers on the regular mesh (figure 3.3), evaluating the temperature normal to the boundary at $T(\Delta n)$ requires local interpolation, which we discuss in the Supplementary Material. After calculating the boundary velocity, the boundary points are advected in a Lagrangian sense (Udaykumar *et al.*, 2001) using an explicit Euler step.

Mechanical Evolution

To treat the mechanical thinning of the lithosphere, we develop a deformation model for a lithosphere under a horizontal tectonic force. For mechanical equilibrium, the net horizontal force in the lithosphere must sum to zero. We consider a balance between a constant far field tectonic force F_o and a resisting force due to rock strength F_r:

$$F_o - F_r = 0. \tag{3.15}$$

In a similar manner to Bialas *et al.* (2010), we consider the case where the extensional force is derived from the regional topographic swell generated by plume buoyancy. In this case, horizontal stresses are similar to ridge push and the resulting force is in the range of 2.5-6 TN m^{-1} (Bott, 1991). This assumption is justified in the case of the East Africa Rift (which we focus on in the discussion) by the presence of a regional topographic swell consistent with the presence of buoyant material in the asthenospheric mantle (e.g. Nyblade and Robinson, 1994). In this study, we use $F_o = 6$ TN m^{-1} and assume that local thinning of the lithosphere does not greatly influence the available force so that F_o is constant (until lithosphere failure occurs, discussed below).

The resisting force in the force balance is the integral of the lithosphere yield stress,

$$F_r = \int_0^{z_L(x)} \sigma \mathrm{d}z, \tag{3.16}$$

where $z_L(x)$ is the local lithosphere thickness and the deviatoric stress, σ, is given by the minimum of Byerlee's law (Byerlee, 1978) and a ductile yield stress:

$$\sigma = \min \left\{ \begin{array}{l} \mu P \\ \left(\frac{\dot{\epsilon}}{A_{\text{dis}}} \exp((Q_{\text{dis}} + PV_{\text{dis}})/RT) \right)^{1/n_{\text{dis}}} \end{array} \right\}, \tag{3.17}$$

where μ is a friction coefficient, A_{dis} is a compositional dependent pre-exponential constant, $\dot{\epsilon}$ is strain rate, Q_{dis} is activation energy, P is hydrostatic pressure, V_{dis} is activation volume, R is the universal gas constant, T is the absolute temperature and n_{dis} is the stress exponent. We use the thermal model described in the previous section to calculate T and set the compositional parameters (μ,A_{dis},Q_{dis},V_{dis},n_{dis}) at the start of each simulation, leaving the strain rate as the only unknown variable. In the results presented here, we use creep parameters for dry, olivine dislocation creep (Hirth and Kohlstedt, 2003) given in table 3.3.

In the simulations presented here, we vary μ between 0.12 and 0.36. As discussed in more detail in section 3.5.1, geophysical and theoretical studies of earthquakes indicate that dynamic rupture can induce failure on large sections of a fault so that the average stress never reaches the Byerlee stress (e.g. Noda and Lapusta, 2013). So in this study, we view μ as an effective friction coefficient that reflects the slip at lower stress due to dynamic rupture. For the sake of comparison, the upper end that we test, 0.36, is the same as the effective coefficient of friction for a rock with a pore fluid at hydrostatic pore pressure (Brace and Kohlstedt, 1980), but we stress that we are considering a dry lithosphere and use 0.36 only as a point of comparison.

As the lithosphere thins, the tectonic force is distributed over a smaller thickness and eventually the lithosphere cannot support the full force. The maximum force accommodated by the lithosphere is simply the integral of the brittle yield stress over lithosphere thickness, $\mu\rho_s g z_L^2/2$. For a force of 6 TN m^{-1} and a friction coefficient of 0.36, the minimum lithosphere thickness to support the applied force is ~30 km. For smaller friction coefficient, the minimum lithosphere thickness increases. When the lithosphere cannot support the full force, it deforms at a rate limited by external plate boundary conditions. In our model, if a portion of the lithosphere reaches total failure (when $F_r < F_o$), we reduce the tectonic force by the force deficit and calculate strain rates in the failed regions using a constant displacement rate. In this case, the strain rate in the failed region is simply the far field displacement rate divided by the total width of the failed region. We use a displacement rate of 1 mm yr^{-1} based on typical plate velocities in East Africa (e.g. Stamps *et al.*, 2008).

For a given tectonic stress, we calculate the strain rate as a function of x in the lithosphere by substituting (3.16)-(3.17) into (3.15) and minimizing with respect to $\dot{\epsilon}$:

$$-\int_0^{z_L(x)} \sigma(\dot{\epsilon})\mathrm{d}z + F_o = 0. \tag{3.18}$$

We repeat the minimization for each lithosphere column, and so calculate the strain rate as a function of x. Because strain rate can vary by many orders of magnitude in our model and the minimization needs to be repeated for each x, we minimize equation 3.18 with a simple tabulation method. For each lithospheric column, we calculate the residual of 3.18 for a range of strain rates and then take the strain rate that yields the lowest residual. If the residual is higher than an imposed tolerance (1%), we repeat the tabulation for a subset of strain rates in the vicinity of the previous low. In practice, we found that minimizing 3.18 with respect to $\log\dot{\epsilon}$ avoids potentially troubling round off error. We integrate σ using Simpson's Rule (Press, 2007).

After finding $\dot{\epsilon}(x)$, we calculate the solid velocity of the lithosphere assuming that the lithosphere deforms by pure shear. In this case, the vertical and horizontal solid velocities are

$$V_z^s(x,z) = -\dot{\epsilon}(x)\frac{z}{z_L(x)}, \tag{3.19}$$

$$V_x^s(x,z) = \int_0^x \dot{\epsilon}(x)\mathrm{d}x. \tag{3.20}$$

We then use V_z^s and V_x^s to calculate the advective transport of heat in the thinning lithosphere (Section 3.3.1).

In addition to the tectonic forces from plate boundary conditions and regional uplift, buoyancy forces from crustal thinning, basin infill and thermal expansion strongly influence rift morphology (e.g. Buck, 1991; Bialas and Buck, 2009). In this study, our aim is to investigate the fundamental coupling between melt migration and lithosphere thinning. Toward that end, we treat the simplest possible model by neglecting buoyancy forces, leaving their inclusion to future studies.

3.3.2 Melt Migration

To treat melt migration in the asthenosphere, we solve the 2-D system of equations for the porous flow of melt in the viscously deforming asthenosphere (e.g. Spiegelman, 1993a,b). Because the time scale of melt migration is short compared to the thermal and mechanical evolution of the lithosphere, the melt distribution adjusts rapidly to any changes in the lithosphere state and so we calculate quasi steady state melt distributions for a given lithosphere structure. One of the unique features of our model is that we enforce boundary conditions on the two-phase system along the sloping lithosphere-asthenosphere boundary using an immersed boundary method (e.g. Mittal and Iaccarino, 2005; Tseng and Ferziger, 2003). This approach allows us to investigate the situation with a nonzero flux into the lithosphere that is dependent on local lithosphere stress and the melt fraction just below the boundary. Because the 2-D two-phase system has been investigated in a wide variety of studies, in this section we describe the general assumptions of the two-phase model and the formulation of the diking flux at the lithosphere-asthenosphere boundary. We describe the governing equations in more detail in the Supplementary Material.

General Assumptions

In our solution, we assume that the viscosity of the asthenosphere is sufficiently low to neglect dynamic pressure gradients from solid shear (Morgan, 1987; Spiegelman and McKenzie, 1987), resulting in melt flow primarily driven by melt buoyancy. As a result, the momentum conservation equations for the two-phase system simplify to a single Helmholtz equation the relates the excess pressure (difference between fluid and solid pressure) to pressure gradients arising from buoyancy and compaction(e.g. Aharonov *et al.*, 1995). We decompose the solid velocity field into the gradient and curl of a scalar and vector flow potential (Spiegelman, 1993a) and calculate solid compaction velocities by solving the resulting Poisson equation. We then calculate the total velocity field by summing the compaction velocities and the background flow induced by the mechanical thinning of the lithosphere.

We use commonly adopted constitutive relationships for permeability, k, and compaction viscosity, ξ: $\xi = \eta_s \phi^{-1}$ (e.g. Simpson *et al.*, 2010) and $k = \frac{\phi^3 a^2}{300}$ (e.g. Wark and Watson, 1998), with grain size a=1 cm and background solid shear viscosity $\eta_s = 10^{19}$ Pa s. It is worth noting that while many theoretical studies use $\xi \propto \phi^{-1}$, experiments on partially molten rocks may indicate a larger (i.e., more negative) exponent (Renner *et al.*, 2003).

Melt in our model is generated with a prescribed melting rate, $\dot{\Gamma}$, that captures the main features of melting in a mantle plume. In general, the melting rate from adiabatic decompression is related to melt productivity $\frac{\mathrm{d}F}{\mathrm{d}P}$, solid upwelling velocity

V_z^s and the hydrostatic pressure gradient (e.g. Phipps Morgan, 2001):

$$\dot{\Gamma} = \rho_s g \frac{\mathrm{d}F}{\mathrm{d}P} V_z^s, \tag{3.21}$$

The melting rate in a mantle plume is highest along the plume axis, where temperatures and velocities are highest. Additionally, as the plume impinges on the lithosphere base and upward flow stagnates, decompression melting ceases. We represent this melting rate distribution using a Gaussian function that decays with distance from a plume axis and with height above melting onset. Two decay scales, x_p and δ_z, characterize the decay in the horizontal and vertical directions, respectively:

$$\dot{\Gamma}(x) = \rho_s g \frac{\mathrm{d}F}{\mathrm{d}P} V_o \mathrm{exp}\left(-(x/x_p)^2\right) \exp\left(-(z/\delta_z)^2\right), \tag{3.22}$$

where $\frac{\mathrm{d}F}{\mathrm{d}P}$ and V_o are now the maximum melt productivity and upwelling velocity in the plume center. We fix δ_z at 60 km , V_o at 20 cm/yr, x_p at 50 km and vary $\frac{\mathrm{d}F}{\mathrm{d}P}$ (see table 3.2).

We solve the melt migration governing equations with a finite volume discretization. The fluid mass conservation equation is solved using a second order conservative slope-limiting advection scheme (Van Leer, 1977; Hourdin and Armengaud, 1999). The Helmholtz equation for excess pressure and Poisson equation for compaction potential are solved using GMRES with Jacobian preconditioning through PETSc (Balay *et al.*, 2013). For boundary conditions for excess pressure and flow (figure 3.3), we set the compaction rate to zero on the bottom horizontal and right vertical boundary (P=0, $\frac{\partial S}{\partial x_i} = 0$) and set the $x = 0$ plane as symmetric ($\frac{\partial P}{\partial x} = 0, S_x$=0). The boundary condition along the sloping interface is discussed below. The melt fraction is set to a small nonzero value below the prescribed melting onset depth (ϕ=10^{-6}).

See Supplementary Material for the full set of governing equations and additional boundary conditions on the solid velocity.

Diking Flux at the LAB

Along the lithosphere-asthenosphere boundary, we enforce a flux boundary condition based on the diking flux described in Section 3.2.2 using an immersed boundary approach. Along the base of the lithosphere, we enforce the Darcy flux, S, normal to the boundary,

$$\underline{S} \cdot \hat{n}\Big|_{T=T_{\mathrm{LAB}}} = S_d. \tag{3.23}$$

In our model, the imposed flux S_d is time dependent and varies with the melt fraction just below the boundary and the lithosphere stress. In Section 3.2.2, we described the time averaged flux of melt across the base of the lithosphere predicted by the numerical scaling relationship of Havlin *et al.* (2013). The main feature is that the diking flux increases with both the melt fraction just below the lithosphere base and the available tectonic stress. As noted earlier in section 3.2.2 and figure 3.2b, the diking efficiency, D_k (the ratio of the dike flux to the buoyant Darcy flux at the same melt fraction), increases linearly with stress. Assuming that the diking flux increases as ϕ^3 (figure 3.2)

$$D_k = \frac{\sigma}{\sigma_o} D_k(\sigma_o). \tag{3.24}$$

For this study, we take a slope, $D_k(\sigma_o)/\sigma_o$, of 0.3/100 MPa^{-1} based on the stress dependence of the diking efficiency shown in figure 3.2b, which captures the essential features of a strong dependence of dike flux on melt fraction and stress state.

To enforce the dike flux, we first calculate D_k from the stress state at the base of the lithosphere calculated in the thermal-mechanical model (Sections 3.3.1,3.3.1). The flux that is applied along the boundary is then

$$\underline{S} \cdot \hat{n} \Big|_{T=T_{\mathrm{LAB}}} = S_b D_k, \tag{3.25}$$

where $S_b = \Delta \rho g k / \eta_f$. We use the permeability k just below the boundary and update $S_b D_k$ every time step so that the dike flux out adjusts as melt fraction changes beneath the boundary. In our formulation, we solve for excess pressure and so the imposed flux constrains the pressure gradient normal to the boundary. Similar to our solution for the thermal evolution, we apply the immersed boundary algorithm of Tseng and Ferziger (2003) to impose the Neumann condition on excess pressure along the lithosphere base using linear reconstruction. The numerical scheme and application of the immersed boundary method is addressed in more detail in the Supplementary Material.

We calculate the heat flux from infiltrating melt to account for both melt injected in dikes and melt that freezes on to the base of the lithosphere. From mass conservation, the total flow of melt at a given depth is the sum of the Darcy flux, $\underline{S}$, and the porosity advected by the solid velocity $\underline{V}^s$:

$$\phi \underline{v}^f = \underline{S} + \phi \underline{V}^s. \tag{3.26}$$

so that even when $S = 0$, there can be an associated heat source from freezing melt. Because melt maintains thermal equilibrium with the surrounding matrix and we are considering dikes intruding at the base of the lithosphere, the heat flux into the lithosphere due to melt infiltration is primarily from latent heat so that the melt infiltration heat flux,q_m, is the product of the boundary-normal flux and the latent heat,

$$q_m = \rho_f L(\underline{S} + \phi \underline{V}^s) \cdot \hat{n}. \tag{3.27}$$

In this study, we calculate q_m a posteriori from the 2-D melt migration model and compare to the heat flux from 1-D melt migration at steady state that is used to force the thermal model.

3.4 Results

3.4.1 Lithosphere Thinning

First, we consider lithosphere thinning forced by the heat flux from vertical, steady state melt migration. This basic state yields rapid lithosphere thinning at rates greater than those calculated for solid state models of thermal-mechanical erosion by mantle plumes. We identify two main stages of lithosphere thinning common to all simulations: (1) purely thermal thinning in which temperature varies rapidly near the lithosphere base and (2) coupled thermal-mechanical thinning in which strain rates increase to a magnitude typical of rifts. The transition between the two depends strongly melt productivity, the initial geotherm, the coefficient of friction in the lithosphere. Simulations presented here use model dimensions of 200 km by 200 km, with uniform 2 km by 2 km cells.

In figure 3.4, we show a typical thermal evolution for a lithosphere thinning a peak melt productivity of 6 % GPa^{-1}, 0.24 friction coefficient and initial geotherm calculated for a basal heat flux of 30 mW m^{-2}. Other parameters, which we fix for all simulations presented here, are given in table 3.3. The nondimensional melting rate in the asthenosphere, used in all simulations, is shown in 3.4b. The resulting heat flux into the lithosphere base (shown in figure 3.4a) is then the integral of the melting rate over z for each x added to the background heat flux from small scale, solid state convection. For the melt productivity in this case (6 % GPa^{-1}), the heat flux varies from above 300 mW m^{-2} at the plume axis to about 50 mW m^{-2} where melting is negligible.

The large heat flux from infiltrating melt drives rapid thinning of the lithosphere. In the example in figure 3.4, the lithosphere starts with a thickness just under 100 km and then thins rapidly to around 70, 50 and 35 km at times of 5, 10 and 15 Mrs, respectively (figures 3.4c, 3.4d, 3.4e). While the lithosphere base appears stepped in figure 3.4, the Lagrangian boundary points that track the LAB define a smoothly varying boundary (figure 3.5a) and the temperature varies smoothly in the vicinity of the boundary, which lends confidence to the immersed boundary approach used here. Because diffusion of heat in the lithosphere is relatively slow, a thermal boundary layer develops at the base of the lithosphere, evident in vertical profiles of the temperature at x=0 shown in figure 3.5b. These profiles are similar to those calculated for lithosphere thinning from convective destabilization (Yuen and Fleitout, 1985) but advance more rapidly due to the additional melt infiltration heat flux. These results show that significant thermal thinning may occur without modification of the surface heat flow, a point that we return to in the discussion.

In figure 3.6, we present the mechanical data from the same simulation as in figure 3.4. As the lithosphere warms, the strain rate (3.6a) increases and localizes in the region of greatest thinning. Correspondingly, the stress at the base of the lithosphere increases as strain rate increases (3.6b). Between 10-11 Myrs, the peak strain rate increases to a value typical of rifts (10^{-15} s^{-1}). As mechanical thinning initiates the additional velocity component is evident in the slight change in boundary curvature at 14 Mrs from 0 to 30 km in figure 3.5a. After this point, thermal and mechanical thinning proceeds until the remaining lithosphere can no longer support the tectonic force (after about 12.9 Myr, pure curve in figure 3.6). Upon lithosphere failure, the strain rate in the interior deforming region ($x < 30$ km) decreases to a value determined by the farfield displacement rate.

In figure 3.7, we summarize a suite of simulations by plotting the minimum lithosphere thickness (3.7a) and maximum strain rate (3.7b) for different values of melt productivity, friction coefficient and initial geotherm. Increasing melt productivity increases the lithosphere thinning rate, resulting in earlier onset of mechanical extension (compare solid blue, black and red curves). Decreasing the friction coefficient results in earlier onset of mechanical thinning and a slightly faster thinning rate (compare bold, solid and dashed black curves). Finally, a cooler initial temperature due to a lower initial heat flux (black dash-dot curve) results in an initially thicker lithosphere and slower thinning rates. For each simulation, the lithosphere stress at the LAB mimics the strain rate curves as in the case in Figure 3.6 and so we do not plot the stress at the lithosphere base in Figure 3.7.

3.4.2 Melt Infiltration

To calculate melt distribution and the dike infiltration heat flux at the LAB, we paused the thermal-mechanical lithosphere thinning model at different stages of thinning and used the resulting LAB topography and stress state at the LAB to calculate quasi-steady melt fraction distributions in the asthenosphere. In this section, we first describe the time evolution of quasi-steady melt fraction and infiltration heat flux as the lithosphere thins and then show the dependence for varying melt productivity and lithosphere strength at a fixed time. The important results are (1) melt fraction never approaches the disaggregation limit, even with increased horizontal focusing from LAB topography and (2) the diking heat flux is well described by the imposed 1-D heat flux, except in a narrow, ~ 10 km wide zone at the axis where the heat flux is significantly higher.

In figure 3.8, we show the quasi-steady state melt fraction and melt velocity streamlines at times of 2, 4, 6 and 8 Myrs for a peak melt productivity of 6 % GPa^{-1} and a friction coefficient of 0.12. At each time (3.8a-3.8d), a narrow high-melt fraction boundary layer develops parallel to the boundary and melt streamlines re-orient from vertical to up-slope within the boundary layer. As lithosphere topography steepens, melt streamlines increasingly bend over resulting in horizontal transport of around 1-15 km (figure 3.8d). Horizontal transport is limited to the most steeply sloped section of the LAB so that melt generated more than ∼10 km off-axis never reaches the plume/rift axis. Despite increased horizontal focusing, the maximum melt fraction is maintained at a similar value between 0.02-0.05 throughout. This is a consequence of the coupling between the dike flux and the local melt fraction; melt focusing along the LAB brings more melt, which increases the diking flux, which prevents the melt fraction from increasing.

Using the melt velocity streamlines and quasi-steady melt fields, we calculate the heat flux across the LAB from diking (see Section 3.3.2) for each time shown in figure 3.8 and plot the result in figure 3.9 along with the imposed diking heat flux calculated from 1-D steady-state melting that is used to force the thermal model (black curve). The most obvious feature is the narrow, ∼ 10 km wide, peak in heat flux at the plume/rift axis that is maintained throughout the simulation. While there is some grid-scale variability apparent in the calculated flux, when we integrate the difference in the calculated flux and the imposed heat flux across the model domain, the two balance to within a few percent error, indicating that the numerical approach successfully conserves mass (i.e., all the melt generated is accounted for).

For all parameters tested, the melt distribution and calculated heat flux behave similarly. In figures 3.10 and 3.11 we show melt distributions, melt streamlines and the calculated diking heat flux at 8 Myr for a lithosphere with a higher friction coefficient (0.36) and melt productivity of 6 and 8 % GPa^{-1}. Similar to the case in figure 3.8, a narrow high melt fraction boundary layer develops at the LAB with limited up-slope transport of melt (figures 3.10a and 3.10b). At higher productivity (figure 3.10b), the melt fraction in the boundary layer is generally higher but up-slope transport is not significantly enhanced and the peak melt fraction only reaches 0.048. Similar to the case in figure 3.9, the calculated melt fluxes shown in figure 3.11 show an increased diking heat flux at the plume/rift axis, with negligible dependence on the friction coefficient. Higher melt production results in a stronger focusing of the dike heat flux (dashed green curve in figure 3.11).

In summary, when diking occurs at the LAB, (1) melt fractions never exceed $\sim$0.05 for the limited (but reasonable) range of parameters that we test, (2) diversion of melt along LAB topography induces horizontal transport over a significant fraction of the melting region ($\sim$15 km lateral transport) but melt generated off-axis freezes before reaching the axis and (3) within $\sim$ 10 km of the rift/plume axis, the calculated diking heat flux is significantly higher than the imposed diking heat flux from 1-D steady state melting, but in general the diking heat flux from 1-D steady state melting reasonably matches the calculated heat flux off-axis.

3.5 Discussion

The major points of the simulations conducted here are (1) thinning of the lithosphere from basal heating by intruding dikes proceeds at a rate (tens of km Myr^{-1}) faster than that from only heating by convective instability, (2) infiltrating dikes prevent formation of disaggregated magma bodies deep in the lithosphere, and (3) 2-D melt migration can result in a concentrated heat flux on the order 10 km wide. In the following, we discuss implications with regards to tectono-magmatic strain accommodation, magmatic mixing and eruptions in continental rifts, focusing in large part on the Central Main Ethiopian rift (section 3.5.1). We then discuss our results in the context of receiver function observations from Hawaii and the East African Rift.

3.5.1 Strain, Magmatism and Lithosphere Thinning

The transfer of strain from accommodation on border faults to narrow magmatic segments requires a steady supply of magma. The current understanding is that extension of the lithosphere along preexisting weakness causes thinning that produces melt and LAB topography that focus melt to narrow regions (e.g. Ebinger and Casey, 2001). Though pre-existing heterogeneities undoubtedly influence the spatial distribution and propagation of rifts (e.g. Dunbar and Sawyer, 1989; Theunissen *et al.*, 1996; Tommasi and Vauchez, 2001), the integrated strength of the lithosphere for typical continental lithosphere exceeds available forces for rifting (e.g. Buck, 2004, 2006; Bialas *et al.*, 2010). The simulations presented here suggest that lithospheric extension could begin due to stress concentrations arising from thermal thinning concentrated at the lithosphere base and not manifested at the surface - melt intrudes only a short height above the LAB, and the thermal boundary layer associated with thinning does not greatly affect the surface heat flow on the time scale of thinning (figure 3.5b). Furthermore, because small-scale diking prevents accumulation of large melt fractions (figures 3.8, 3.10), it is unlikely that disaggregated magma chambers will form until the lithosphere thins to crustal levels where mafic melt is less buoyant. We suggest that (1) the onset of extension may be triggered by melt-induced thinning at the lithosphere base and (2) the transfer of strain from border faults to magmatic segments is coincident with the thermal/mechanical erosion of the mantle lithosphere. Once a thermally insulated pathway is created from the source region to the crust, melt can pond and accumulate to levels sufficiently high for intruding into the crust. The time between the extension onset time and the magmatic segmentation time should then be related to the time it takes most of the remaining mantle lithosphere to erode.

To test the possibility that basal heating by melt infiltration and subsequent mantle lithosphere removal can explain the timing between extension onset and the shift in strain to magmatic segments, we recorded the time of extension onset and the time at which the lithosphere base reaches crustal levels for each simulation. Because the 2-D melt migration models show that melt flow is mostly vertical (except in a narrow region at the plume axis), we use the thermal-mechanical model with a melt infiltration heat flux fixed by the 1-D, steady state melting to calculate extension onset and mantle lithosphere erosion times. We define the extension onset time as the first point in the simulations where the maximum strain rate reaches 10^{-15} s^{-1}, a value typical for rifts. We then calculate the delay between extension onset and the time at which the LAB reaches the base of the crust, which we term the mantle lithosphere rupture time, t_{rupture}. We plot the difference in rupture and onset time in figure 3.12 as a function of melt productivity (controlling the thermal thinning rate) and the coefficient of friction for the lithosphere. As melt productivity increases, the increasing thermal thinning rate reduces the delay between extension and rupture while decreasing the friction coefficient results in an earlier extension onset.

In the Central Main Ethiopian Rift (MER), extension initiated around 8.3-9.7 Ma (Woldegabriel *et al.*, 1990) and then shifted to magmatic accommodation by 1.6 Ma (Ebinger and Casey, 2001), giving a delay time of 6.7-8.1 Ma, in the possible range that we predict. We can further narrow the field by considering reasonable limits for melt productivity, which is primarily a function of composition and potential temperature (Phipps Morgan, 2001). In figure 3.13a, we plot the productivity of peridotite with 100 PPM H_2O in an adiabatically upwelling column for potential temperatures of 1450^{o}C to 1550^{o}C in 25^oC increments using a hydrous peridotite solidus (Katz *et al.*, 2003). Details of the calculation are described in Havlin and Parmentier (2014). To compare to the simulations here, where we use a constant productivity, we average the productivity curves over the melting column height (figure 3.13b). Geochemical and geophysical constraints on the mantle potential temperature beneath East Africa indicates mantle potential temperatures 140-170^{o}C above ambient mantle (Rooney *et al.*, 2012) so that the average productivity is likely between 0.37-0.65, depending on the water content. The overlap between the likely values for productivity and the observed time delay (figure 3.12) show that lithosphere thinning by basal heating can explain the onset of extension and the shift in strain accommodation observed in the central MER for a friction coefficient less than 0.36.

Though the effective friction coefficient required to match the timing of extension and magmatic strain transfer is less than that for classic frictional faulting (0.6 for dry rock; Brace and Kohlstedt, 1980), the required coefficient is similar to that observed in previous geophysical and theoretical studies. Measurements of nodal planes (Middleton and Copley, 2013; Craig *et al.*, 2014), bore hole measurements from mature faults (Lockner *et al.*, 2011; Zoback *et al.*, 1987) and studies investigating stresses generated in megathrusts (Lamb, 2006; Herman *et al.*, 2010; Copley *et al.*, 2011) all suggest that the effective friction coefficient is less than 0.3, perhaps even less than 0.1. The low effective coefficient can be attributed to the dynamic weakening during earthquake rupture in which the coefficient of dynamic friction governs slip (Rice and Cocco, 2007) and so it is not immediately obvious whether or not the low coefficient of friction attributed to dynamic friction is applicable on the tectonic time-scale of rifting (or initiation of subduction where a similarly low friction coefficient is required (Moresi and Solomatov, 1998)). However, studies of earthquake rupture propagation show that when the rupturing material exhibits rate weakening behavior, only a small portion of a fault needs to reach the Byerlee stress to nucleate an earthquake and cause slip over a large fraction of the fault (e.g. Noda and Lapusta, 2013). As a result, slip may occur on the majority of a fault at a stress significantly lower than the Byerlee stress so that in a sense the effective coefficient on tectonic time scales is buffered at a value close to that of dynamic friction. While somewhat speculative, this explains the low friction coefficient required by models of tectonic time-scale processes (this study, Moresi and Solomatov, 1998) without invoking the presence of a fluid at or above hydrostatic pressure over the entire lithosphere. And finally, it is worth noting that the observation of deep (25-40 km) earthquakes in East Africa within regions where extension is still dominated by border faults (Shudofsky *et al.*, 1987; Jackson and Blenkinsop, 1993; Nyblade and Langston, 1995; Camelbeeck and Iranga, 1996) requires a relatively deep brittle-ductile transition, which would be encouraged with a lower friction coefficient.

Beyond offering insight into the transfer of strain in rift basins, the model presented in this study can explain several observations from the geochemistry of lavas erupted in the central MER. In general, lavas erupted from continental rifts exhibit an impressive diversity of composition that varies spatially and temporally (Deniel *et al.*, 1994). Even within magmatic segments, heterogeneity of unique source characteristics is preserved between individual cinder cones, indicating poor lateral mixing of magma (Rooney, 2010; Rooney *et al.*, 2011, 2014). Our 2-D melt migration models show that while there is some focusing of melt along the LAB as the lithosphere thins, diking effectively short circuits up-slope transport so that melt migration is mostly vertical (figures 3.8, 3.10). As a result, diking at the LAB may limit mixing between melts with different source lithologies.

In addition to geochemical variations in the MER, the magmatic-induced thinning model presented here is consistent with observations from the Big Pines Volcanic Field in the western U.S. (Gazel *et al.*, 2012). Using thermobarometry of xenoliths and melt inclusions, Gazel *et al.* (2012) showed samples erupted less than 0.5 Ma generally equilibrated at $\sim$1 GPa less than samples erupted greater than 0.5 Ma. Due to the similarity in the equilibration depth of young samples and the LAB as measured by surface wave tomography, Gazel *et al.* (2012) suggested that the melts equilibrated in a melt accumulation zone at the base of the lithosphere before erupting, and that the shallowing in equilibration depth represents a shallowing of the LAB to its current depth. The thinning rates that we calculate (10s of km/Myr) are sufficiently fast to thin the lithosphere by 30 km ($\sim$1 GPa) in 3 Myr or less, so that melt-induced thinning may explain the observed shallowing of equilibration depths.

Finally, we discuss the occurrence of extrusive volcanism within rifts. Our simulations indicate that melting at steady state does not result in disaggregation and subsequent dikes capable of traversing the lithosphere, but rifting in East Africa is accompanied by volcanism throughout rift evolution, punctuated by early outpouring of flood basalts (e.g. Davidson and Rex, 1980; Menzies *et al.*, 2002; Furman *et al.*, 2006).The implication is that the origin of extrusive volcanism is related to time dependent melting phenomenon, possibly associate with initial melting of a new source. For instance, the arrival of a plume head at the base of the plate may produce melt at rates much higher than considered here (e.g. Hofmann *et al.*, 1997), in which case melt may collect in high enough quantities that micro-diking at the LAB cannot balance. In this case, thermal weakening by diking over a larger fraction of the lithosphere may occur (Bialas *et al.*, 2010; Schmeling and Wallner, 2012). Furthermore, we do not consider additional production of melt that occurs as the lithosphere thins. As the melting column height and upwelling from mechanical thinning increase, the melt production will increase. Regardless, the modeling undertaken here shows that diffuse melt infiltration across the LAB can result in significant thermal erosion of the lithosphere.

3.5.2 Receiver Functions Beneath Volcanic and Extensional Regions

The 2-D melt distributions calculated in the present study relate in several ways to the negative velocity gradient imaged by receiver functions near the base of the lithosphere (see Section 3.2). When diking occurs at the lithosphere-asthenosphere boundary (LAB), a quasi-steady state high melt fraction boundary layer develops, as seen in 2-D melt distributions in figures 3.8 and 3.10 and as shown in 1-D by Havlin *et al.* (2013). The elevated melt fraction (0.02-0.05) would generate a considerable drop in shear wave velocity (ϕ of 0.02 results in about a 15% drop in shear wave velocity using the relaxed, organized cuspate geometry of Hammond and Humphreys (2000)) and our results predict that in regions of mantle melt production the largest amplitude velocity change should coincide with the shallowest point in the lithosphere. As noted in Section 3.2, the shallowest and strongest negative velocity gradients observed in eastern Australia correspond with recent Cenozoic volcanism (Ford *et al.*, 2010). Our results suggest that local regions of increased melt generation result in local lithosphere thinning and increased melt accumulation. Lateral transport may occur, but variations in melt generation primarily control the thinning and quasi-steady melt fraction.

Our study considers plume impingement on a fixed plate, but relative motion between the plume and plate will reduce the time available for thinning. For the Hawaiian and Galapagos hotspots, the melt distribution at 2-4 Myr in figure 3.8 is most applicable and shows that a strong seismic velocity contrast would be expected above a region of melt production and that less than 20 km of thinning may result from basal heating by dikes. Only 20 km of thinning would be difficult to resolve beneath Hawaii and Galapagos, where uncertainties in depth locations for the migrated receiver functions are on the order of ± 10 km (Rychert *et al.*, 2013, 2014).

The lack of a negative phase beneath Yellowstone (Hopper *et al.*, 2014) and the gap beneath Hawaii (Rychert *et al.*, 2013) are not easily explained by our model at present but the "missing" phase in the Main Ethiopian Rift (Rychert *et al.*, 2012) is consistent with our model. The absence of a phase seems to suggest that there is a well developed, thermally insulated network that allows melt to pass through most of the lithosphere without freezing. However, our model needs on the order of 10 Myrs to erode most of the lithosphere and the Hawaii and Galapagos have only 2-5, given the motion of the Pacific plate. One possibility is that the locally high heat flux that we calculate close to the plume axis (Figures 3.9,3.11) causes highly localized thinning, which may then drain adjacent regions and prevent accumulation. Alternatively, the solidus of the melt may evolve as solidification proceeds due to partitioning of volatile elements into the remaining melt, which may allow melt to migrate to a much shallower level. The lack of a negative phase beneath the Main Ethiopian Rift (Rychert *et al.*, 2012) is more easily explained; when thinning proceeds to the point where the mantle lithosphere has been mostly eroded, melt can easily migrate to the base of the crust, in which case the negative phase would destructively interfere with the Moho phase. Vp/Vs ratios greater than 2.0 in Ethiopia strongly suggest the presence of partial melt in the crust (Hammond *et al.*, 2011), supporting the idea that melt can easily migrate without accumulating at depth beneath the rift axis. In all these cases, the negative phase off-axis is likely due to accumulation above regions of low melting rate – in our model, the melting rate decays to 0, but a small amount of melting would result in accumulation and negligible thinning (e.g., 60-80 km off-axis in figure 3.8).

The negative velocity gradient observed beneath extensional regions such as the Salton Trough (Lekic *et al.*, 2011), Rio Grande Rift (Lekic and Fischer, 2013) and Albertine Rift (Wolbern *et al.*, 2012) indicate that a barrier to melt flow persists at depth beneath along the base of most of the lithosphere in these locations. The evidence for extrusive and intrusive volcanism in these locations requires that some pathways for melt exist, which could arise from local regions of high melt generation and infiltration (e.g., Figures 3.9,3.11). The localities that exhibit a gap in the negative phase are regions typically associated with high melt production and mantle plumes (Hawaii, Yellowstone, Afar), which suggests that in most locations of "normal" melting, melt accumulates at the base of the lithosphere before migrating farther.

In summary, though there are many remaining questions about how melting and melt migration give rise to the observed velocity decrease near the base of the lithosphere, our results seem to be consistent with a melt accumulation origin. A difference in hydration and/or fertility may add an additional contrast, especially if volatile-rich melts concentrate volatiles at the lithosphere-asthenosphere boundary, but the accumulation of melt at its solidus is likely the more dominant cause of the rapid seismic velocity decrease at the base of the lithosphere.

3.6 Conclusion

We developed a framework for coupling melt migration in the asthenosphere to the thermal mechanical evolution of the lithosphere through the propagation of dikes from a partially molten boundary layer at the base of the lithosphere. At present, we have explored a relatively limited parameter range, but initial results show that diking from the lithosphere-asthenosphere boundary (1) results in rapid thermal erosion (10s of km Myr^{-1}) that concentrates stress in the remaining lithosphere and triggers surface extension without altering the surface heat flow, (2) reduces horizontal transport along the sloping lithosphere-asthenosphere boundary and (3) prevents accumulation of melt fraction above $\sim$0.05. We find that 2-D focusing effects result in a peak in the dike infiltration heat flux within a narrow zone above the region of maximum melt production so that over the whole width of the model domain, the heat flux into the lithosphere from diking is reasonably approximated by 1-D steady state melt extraction.

In the discussion, we show that the predicted time between extension onset triggered by basal lithosphere erosion and the point at which the mantle lithosphere erodes completely can reproduce the time between extension onset and transfer of strain to magmatic segments in the Central Main Ethiopian Rift. Given the observed strain accommodation transfer time and reasonable melt production rates, the friction coefficient for brittle failure required for the lithosphere in East Africa is less than 0.36, consistent with the presence of deep earthquakes in incipient rift basins and the low effective coefficient of friction predicted for a lithosphere where dynamic rupture limits the stress to values less than the Byerlee stress. Thinning rates and melt streamlines are consistent with inferences of thinning and poor magma mixing in both the western U.S. and East Africa. And the calculated melt distributions are consistent with the view that the velocity drop imaged by receiver functions near the base of the lithosphere is due accumulation of melt at its solidus.

In summary, basal heating of the lithosphere by infiltrating melt is an efficient mechanism for lithosphere thinning for typical melt production rates, warranting further study. In particular, considering the role of buoyancy forces during extension, a pressure-dependent solidus and a wider range of plume parameters (upwelling velocity, potential temperature) may yield interesting behavior with implications for the accumulation and infiltration of melt at the lithosphere-asthenosphere boundary.

3.7 Supplemental Material

3.7.1 Two-Phase 2-D Governing Equations

The migration of magma in the asthenosphere is governed by a system of equations that describe conservation of mass, momentum and energy for a porous flow of melt through viscously deforming mantle (McKenzie, 1984; Fowler, 1985; Ribe, 1985; Bercovici *et al.*, 2001). Here, we briefly describe the governing equations for the system in 2-D (Spiegelman, 1993a,b). As we are only considering energy conservation in the lithosphere, we do not present the analogous equation for energy conservation of the two phase system.

Under the extended Boussinesq approximation, mass changes in fluid or solid volume fraction arise from gradients in an advective flux and melting or freezing,

$$\frac{\partial \phi}{\partial t} = \underline{\nabla} \cdot (\phi \underline{v}^f) + \dot{\Gamma} \tag{3.28}$$

$$\frac{\partial}{\partial t}(1-\phi) = \underline{\nabla} \cdot ((1-\phi)\underline{V}^s) - \dot{\Gamma} \tag{3.29}$$

where $\underline{v}^f$ is the fluid (melt) velocity, ϕ is melt fraction (i.e., porosity), $\dot{\Gamma}$ is the melting rate and $\underline{V}^s$ is the solid velocity. We describe our treatment of the melting rate $\dot{\Gamma}$ in the main text in Section 3.3.2.

Though each phase is considered incompressible, porosity of the aggregate changes due to compaction or decompaction driven by various pressure gradients. Pressure gradients arise due to buoyancy of the fluid (e.g. Sparks and Parmentier, 1991), viscous pressure gradients from solid convection (e.g. Spiegelman and McKenzie, 1987), surface tension (e.g. Stevenson, 1986), melt-rock reactions (e.g. Daines and Kohlstedt, 1994; Spiegelman *et al.*, 2001) and dynamic viscosity feedbacks (e.g. Stevenson, 1989; Holtzman and Kohlstedt, 2007). In general, this leads to a generalized Stokes-system that resembles the traditional Stokes flow for convection of a fluid at infinite Prandtl number. As a first approach in coupling a two-phase model to lithosphere deformation, we consider only buoyancy forces. This simplifies the governing equation for conservation of momentum considerably, leaving a variable coefficient Helmholtz equation for excess pressure, P (e.g. Aharonov *et al.*, 1995):

$$\frac{P}{\xi} - \underline{\nabla} \cdot \frac{k}{\eta_f}(\underline{\nabla} P - \Delta\rho \underline{g}) = 0 \tag{3.30}$$

where ξ is the compaction viscosity, k is permeability, η_f is fluid viscosity, $\Delta\rho$ is the solid-fluid density difference and $\underline{g}$ is gravitational acceleration. We take η_f to be a constant 1 Pa s, while ξ and k are both functions of porosity, ϕ. We use a commonly adopted form of the compaction viscosity, $\xi \approx \eta_s \phi^{-1}$ (e.g. Simpson *et al.*, 2010), but note that laboratory studies may indicate a stronger dependence on ϕ (Renner *et al.*, 2003). We use a permeability that scales with the cube of the melt fraction, $k = \frac{\phi^3 a^2}{C}$ (Wark and Watson, 1998), with a grain size a=1 cm and matrix tortuosity C=300.

The solid velocities can be decomposed into scalar and vector potential gradients via a Helmholtz decomposition (Spiegelman, 1993a),

$$\underline{V}^s = \underline{\nabla}\psi + \underline{\nabla} \times \underline{\Psi}. \tag{3.31}$$

Taking the divergence of equation 3.31 and recognizing $P/\xi = \underline{\nabla} \cdot \underline{V}^s$ reveals that the flow arising from the scalar potential, $\underline{V}^s_\psi \equiv \underline{\nabla}\psi$, is solely due to the compaction and decompaction of the solid,

$$\frac{P}{\xi} = \nabla^2\psi. \tag{3.32}$$

The velocity arising from the vector potential, $\underline{V}^s_\Psi \equiv \underline{\nabla} \times \underline{\Psi}$, is due to incompressible stokes flow due to imposed boundary conditions and body forces. Thus, the system can be solved sequentially by first solving for P (equation 3.30), then ψ (equation 3.32). A conventional stokes solver, or in our case a simplified deformation model, can be used to solve for the stokes velocity, giving the total velocity $\underline{V}^s = \underline{V}^s_\psi + \underline{V}^s_\Psi$. The Darcy velocity is determined by P and so the fluid velocities can be calculated,

$$\underline{S} = -\frac{k}{\eta_f}(\underline{\nabla}P - \Delta\rho\underline{g}), \tag{3.33}$$

$$\underline{v}^f = \underline{S}/\phi + \underline{V}^s. \tag{3.34}$$

3.7.2 Compaction Velocity Boundary Conditions

As describe in Section 3.3.2, we enforce a time and spatially dependent dike flux normal to the lithosphere-asthenosphere boundary (LAB). A similar condition exists for the solid velocity. Because of the short relaxation time for rock at a temperature close to the solidus, we assume that stresses generated by small-scale diking are dissipated rapidly and correspondingly, there is a flow of solid material back across the boundary to balance the melt flux. The solid compaction velocity, $\underline{V}_c^s$, normal to the boundary is then

$$\underline{V}_c^s \cdot \hat{n} = -S_d. \tag{3.35}$$

In terms of the solid scalar potential U, the equivalent statement is that the normal gradient of the scalar potential is the negative of the flux across the boundary,

$$\frac{\partial U}{\partial n} = -S_d. \tag{3.36}$$

We enforce this condition while solving the Poisson equation for the scalar potential using the immersed boundary method in an analogous fashion to enforcing the gradient in excess pressure.

Along the left and right boundaries, we set the normal derivative of U to zero (no compaction across the boundaries). Along the bottom boundary, we enforce $U = 0$, though cases with $\frac{\partial U}{\partial z} = 0$ yield nearly identical results.

3.7.3 The Immersed Boundary Method

The immersed boundary method (IBM) has been used in a wide variety of studies to enforce boundary conditions along topologically complex surfaces that intersect a fixed, Eulerian grid (e.g. Mittal and Iaccarino, 2005). The major advantage of the IBM is that it avoids potentially complicated re-meshing procedures when enforcing boundary conditions along curved surfaces. In this study, we employ the algorithm of Tseng and Ferziger (2003) to enforce boundary conditions along the base of the lithosphere. Specifically, we use a Dirichlet condition to enforce a constant temperature (Section 3.3.1) and a Neumann to enforce a time-variable melt flux (3.3.2) along the boundary. The linear extrapolation described by Tseng and Ferziger (2003) uses the values of nearby points in the computational domain to construct values for the ghost cells residing across the boundary. The linear weighting function, which we write in terms of excess pressure P is given by

$$P = a_o + a_1 x + a_2 z, \tag{3.37}$$

where a_o, a_1 and a_2 are weighting coefficients, and x, z are spatial coordinates. For a Neumann condition, the weighting coefficients are found by solving the system of equations

$$\begin{bmatrix} a_o \\ a_1 \\ a_2 \end{bmatrix} = \mathrm{inv}(\underline{\underline{B}}) \begin{bmatrix} \frac{\partial P}{\partial n} \\ P_1 \\ P_2 \end{bmatrix}, \tag{3.38}$$

where P_1 and P_2 are neighboring points evaluated at locations (x_1, z_1) and (x_2, z_2), $\frac{\partial P}{\partial n}$ is the boundary condition being enforce, and n is the outward normal direction from the boundary. The weighting matrix $\underline{\underline{B}}$ is given by

$$\underline{\underline{B}} = \begin{vmatrix} 0 & -\sin\theta & \cos\theta \\ 1 & x_1 & z_1 \\ 1 & x_2 & z_2 \end{vmatrix}, \tag{3.39}$$

where θ is the local boundary slope. Enforcing a Dirichlet condition is analogous except the first row of $\underline{\underline{B}}$ is replaced with the ghost cell coordinates, $(1\ x_g\ z_g)$, and $\frac{\partial P}{\partial n}$ is replaced with the desired value.

To save computational expense, we solve 3.37-3.39 analytically, resulting in the equation for the ghost cell value,

$$\begin{aligned} P_g =& \frac{\partial P}{\partial n}(A_{11} + x_g A_{21} + z_g A_{31}) \ ... \\ &+ P_1(A_{12} + x_g A_{22} + z_g A_{32}) \ ... \\ &+ P_2(A_{13} + x_g A_{23} + z_g A_{33}), \end{aligned} \tag{3.40}$$

where A_{ij} are the components of the matrix inv($\underline{\underline{B}}$), found analytically. For enforcing the temperature condition, we use 3.40 directly to calculate a value to place in the ghost cell. The diffusion operator then treats the ghost cell as a normal cell in the centered space scheme. However, for the excess pressure, we are using a direct solver and we use 3.40 to replace the corresponding row in the solution matrix from the discretization of the excess pressure Helmholtz equation.

The algorithm of Tseng and Ferziger (2003) was developed for a fixed boundary position, but the boundary here is moving (at least in the thermal problem). A number of approaches are possible (see Mittal and Iaccarino (2005) for a review) and we adopt a simple Lagrangian front tracking method, most similar to that described by Udaykumar *et al.* (2001). The boundary velocity is calculated using a local energy balance (Section 3.3.1) and used to advect a set of boundary nodes. As the boundary nodes move, the boundary can deform, which requires either adding additional points or boundary re-meshing (Udaykumar *et al.*, 2001). To avoid this complication, we instead advect the boundary nodes using only the vertical component of the boundary velocity, which in effect averages the local boundary position between nodes every time step. Additionally, calculating the boundary velocity requires evaluating the local temperature field to calculate the temperature derivative on the lithosphere-side of the boundary (Section 3.3.1). We construct a local interpolation scheme using the same linear weighting scheme as for enforcing boundary conditions, except the boundary condition is replaced with a known value from the computational grid.

3.8 References

Agrusta, R., D. Arcay, A. Tommasi, A. Davaille, N. Ribe, and T. Gerya 2013. Small-scale convection in a plume-fed low-viscosity layer beneath a moving plate. *Geophysical Journal International*, 128.

Aharonov, E., J. A. Whitehead, P. B. Kelemen, and M. Spiegelman 1995. Channeling instability of upwelling melt in the mantle. *J. Geophys. Res. 100*(B10), 20433–20450.

Balay, S., J. Brown, , K. Buschelman, V. Eijkhout, W. D. Gropp, D. Kaushik, M. G. Knepley, L. C. McInnes, B. F. Smith, and H. Zhang 2013. PETSc Users Manual. Technical Report ANL-95/11 - Revision 3.4, Argonne National Laboratory.

Ballmer, M., J. Van Hunen, G. Ito, P. Tackley, and T. Bianco 2007. Non-hotspot volcano chains originating from small-scale sublithospheric convection. *Geophysical Research Letters 34*(23).

Ballmer, M. D., G. Ito, J. van Hunen, and P. J. Tackley 2011. Spatial and temporal variability in Hawaiian hotspot volcanism induced by small-scale convection. *Nature Geoscience 4*(7), 457–460.

Bercovici, D., and J. Lin 1996. A gravity current model of cooling mantle plume heads with temperaturedependent buoyancy and viscosity. *Journal of Geophysical Research: Solid Earth (19782012) 101*(B2), 3291–3309.

Bercovici, D., Y. Ricard, and G. Schubert 2001. A two-phase model for compaction and damage 1. General Theory. *J. Geophys. Res. 106*(B5), 8887–8906.

Bialas, R. W., and W. R. Buck 2009. How sediment promotes narrow rifting: Application to the Gulf of California. *Tectonics 28*(4).

Bialas, R. W., W. R. Buck, and R. Qin 2010. How much magma is required to rift a continent? *Earth and Planetary Science Letters 292*(1-2), 68–78.

Bianco, T. A., G. Ito, J. van Hunen, M. D. Ballmer, and J. J. Mahoney 2008. Geochemical variation at the Hawaiian hot spot caused by upper mantle dynamics and melting of a heterogeneous plume. *Geochemistry, Geophysics, Geosystems 9*(11).

Bianco, T. A., G. Ito, J. van Hunen, M. D. Ballmer, and J. J. Mahoney 2011. Geochemical variations at intraplate hot spots caused by variable melting of a veined mantle plume. *Geochemistry, Geophysics, Geosystems 12*(7).

Bilham, R., R. Bendick, K. Larson, P. Mohr, J. Braun, S. Tesfaye, and L. Asfaw 1999. Secular and tidal strain across the Main Ethiopian Rift. *Geophysical Research Letters 26*(18), 2789–2792.

Bott, M. 1991. Ridge push and associated plate interior stress in normal and hot spot regions. *Tectonophysics 200*(1), 17–32.

Brace, W., and D. Kohlstedt 1980. Limits on lithospheric stress imposed by laboratory experiments. *Journal of Geophysical Research: Solid Earth (19782012) 85*(B11), 6248–6252.

Brace, W. F., J. B. Walsh, and W. T. Frangos 1968. Permeability of granite under high pressure. *J. Geophys. Res. 73*(6), 2225–2236.

Buck, W. 2006. The role of magma in the development of the Afro-Arabian Rift System. *Geological Society, London, Special Publications 259*(1), 43–54.

Buck, W. R. 1991. Modes of Continental Lithospheric Extension. *J. Geophys. Res. 96*(B12), 20161–20178.

Buck, W. R. 2004. Consequences of asthenospheric variability on continental rifting. In G. Karner, B. Taylor, N. Driscoll, and D. Kohlstedt (Eds.), *Rheology and Deformation of the Lithosphere at Continental Margins*, pp. 1–30. Columbia University Press.

Byerlee, J. 1978. Friction of rocks. *Pure and applied Geophysics 116*(4-5), 615–626.

Cai, Z., and D. Bercovici 2013. Two-phase damage models of magma-fracturing. *Earth and Planetary Science Letters 368*(0), 1–8.

Camelbeeck, T., and M. Iranga 1996. Deep crustal earthquakes and active faults along the Rukwa trough, eastern Africa. *Geophysical Journal International 124*(2), 612–630.

Copley, A., J. Avouac, J. Hollingsworth, and S. Leprince 2011. The 2001 Mw 7.6 Bhuj earthquake, low fault friction, and the crustal support of plate driving forces in India. *Journal of Geophysical Research: Solid Earth (19782012) 116*(B8).

Craig, T. J., A. Copley, and T. A. Middleton 2014. Constraining fault friction in oceanic lithosphere using the dip angles of newly-formed faults at outer rises. *Earth and Planetary Science Letters* **392**, 94–99.

Daines, M. J., and D. L. Kohlstedt 1994. The transition from porous to channelized flow due to melt/rock reaction during melt migration. *Geophys. Res. Lett. 21*(2), 145–148.

Davaille, A., and C. Jaupart 1993. Transient high-Rayleigh-number thermal convection with large viscosity variations. *Journal of Fluid Mechanics* **253**, 141–166.

Davidson, A., and D. Rex 1980. Age of volcanism and rifting in southwestern Ethiopia. *Nature* **283**, 657–658.

Deniel, C., P. Vidal, C. Coulon, P.-J. Vellutini, and P. Piguet 1994. Temporal evolution of mantle sources during continental rifting: The volcanism of Djibouti (Afar). *J. Geophys. Res. 99*(B2), 2853–2869.

Dunbar, J. A., and D. S. Sawyer 1989. How preexisting weaknesses control the style of continental breakup. *Journal of Geophysical Research 94*(B6), 7278–7292.

Ebinger, C. 2005. Continental break-up: the East African perspective. *Astronomy & Geophysics 46*(2), 2–16.

Ebinger, C., and M. Casey 2001. Continental breakup in magmatic provinces: An Ethiopian example. *Geology 29*(6), 527–530.

Fischer, K. M., H. A. Ford, D. L. Abt, and C. A. Rychert 2010. The lithosphere-asthenosphere boundary. *Annual Review of Earth and Planetary Sciences* **38**, 551–575.

Ford, H. A., K. M. Fischer, D. L. Abt, C. A. Rychert, and L. T. Elkins-Tanton 2010. The lithosphere-asthenosphere boundary and cratonic lithospheric layering beneath Australia from Sp wave imaging. *Earth and Planetary Science Letters 300*(3-4), 299–310.

Fowler, A. C. 1985. A mathematical model of magma transport in the asthenosphere. *Geophysical & Astrophysical Fluid Dynamics 33*(1), 63–96.

Fowler, A. C., and D. R. Scott 1996. Hydraulic crack propagation in a porous medium. *Geophysical Journal International 127*(3), 595–604.

Fuis, G., W. Mooney, J. Healy, G. McMechan, and W. Lutter 1984. A seismic refraction survey of the Imperial Valley region, California. *Journal of Geophysical Research: Solid Earth (19782012) 89*(B2), 1165–1189.

Furman, T., J. Bryce, T. Rooney, B. Hanan, G. Yirgu, and D. Ayalew 2006. Heads and tails: 30 million years of the Afar plume. *Geological Society, London, Special Publications 259*(1), 95–119.

Gazel, E., T. Plank, D. W. Forsyth, C. Bendersky, C. A. Lee, and E. H. Hauri 2012. Lithosphere versus asthenosphere mantle sources at the Big Pine Volcanic Field, California. *Geochemistry, Geophysics, Geosystems 13*(6).

Grasset, O., and E. Parmentier 1998. Thermal convection in a volumetrically heated, infinite Prandtl number fluid with strongly temperaturedependent viscosity: Implications for planetary thermal evolution. *Journal of Geophysical Research: Solid Earth (19782012) 103*(B8), 18171–18181.

Hammond, J., J. Kendall, G. Stuart, D. Keir, C. Ebinger, A. Ayele, and M. Belachew 2011. The nature of the crust beneath the Afar triple junction: evidence from receiver functions. *Geochemistry, Geophysics, Geosystems 12*(12).

Hammond, W. C., and E. D. Humphreys 2000. Upper mantle seismic wave velocity: Effects of realistic partial melt geometries. *J. Geophys. Res. 105*(B5), 10975–10986.

Havlin, C., and E. Parmentier 2014. Implications for melt transport and source heterogeneity in upwelling mantle from the magnitude of Sp converted phases generated at the onset of melting. *Geophysical Research Letters* **41**, 54445450.

Havlin, C., E. Parmentier, and G. Hirth 2013. Dike propagation driven by melt accumulation at the lithosphere-asthenosphere boundary. *Earth and Planetary Science Letters* **376**, 20–28.

Herman, F., P. Copeland, J. Avouac, L. Bollinger, G. Maho, P. Le Fort, S. Rai, D. Foster, A. Pcher, and K. Stwe 2010. Exhumation, crustal deformation, and thermal structure of the Nepal Himalaya derived from the inversion of thermochronological and thermobarometric data and modeling of the topography. *Journal of Geophysical Research: Solid Earth (19782012) 115*(B6).

Hirth, G., and D. Kohlstedt 2003. Rheology of the upper mantle and the mantle wedge: A view from the experimentalists. *AGU Geophysical Monograph* **138**, 83–106.

Hofmann, C., V. Courtillot, G. Feraud, P. Rochette, G. Yirgu, E. Ketefo, and R. Pik 1997. Timing of the Ethiopian flood basalt event and implications for plume birth and global change. *Nature 389*(6653), 838–841.

Holtzman, B. K., and D. L. Kohlstedt 2007. Stress-driven melt segregation and strain partitioning in partially molten rocks: Effects of stress and strain. *Journal of Petrology 48*(12), 2379–2406.

Hopper, E., H. A. Ford, K. M. Fischer, V. Lekic, and M. J. Fouch 2014. The lithosphere–asthenosphere boundary and the tectonic and magmatic history of the northwestern United States. *Earth and Planetary Science Letters*.

Hourdin, F., and A. Armengaud 1999. The Use of Finite-Volume Methods for Atmospheric Advection of Trace Species. Part I: Test of Various Formulations in a General Circulation Model. *Monthly Weather Review 127*(5), 822–837.

Huppert, H. E. 1982. The propagation of two-dimensional and axisymmetric viscous gravity currents over a rigid horizontal surface. *Journal of Fluid Mechanics* **121**, 43–58.

Jackson, J., and T. Blenkinsop 1993. The Malai earthquake of March 10, 1989: Deep faulting within the East African rift system. *Tectonics 12*(5), 1131–1139.

Karato, S.-i., and H. Jung 1998. Water, partial melting and the origin of the seismic low velocity and high attenuation zone in the upper mantle. *Earth and Planetary Science Letters 157*(3-4), 193–207.

Katz, R. F., M. Spiegelman, and C. H. Langmuir 2003. A new parameterization of hydrous mantle melting. *Geochemistry, Geophysics, Geosystems 4*(9).

Kawakatsu, H., P. Kumar, Y. Takei, M. Shinohara, T. Kanazawa, E. Araki, and K. Suyehiro 2009. Seismic Evidence for Sharp Lithosphere-Asthenosphere Boundaries of Oceanic Plates. *Science 324*(5926), 499–502.

Keir, D., C. Ebinger, G. Stuart, E. Daly, and A. Ayele 2006. Strain accommodation by magmatism and faulting as rifting proceeds to breakup: seismicity of the northern Ethiopian rift. *Journal of Geophysical Research: Solid Earth (19782012) 111*(B5).

Kumar, P., and H. Kawakatsu 2011. Imaging the seismic lithosphere-asthenosphere boundary of the oceanic plate. *Geochem. Geophys. Geosyst. 12*(1).

Lamb, S. 2006. Shear stresses on megathrusts: Implications for mountain building behind subduction zones. *Journal of Geophysical Research: Solid Earth (19782012) 111*(B7).

Lawn, B. R. 1993. *Fracture of brittle solids*. Cambridge Univ Pr.

Lekic, V., and K. M. Fischer 2013. Contrasting lithospheric signatures across the western United States revealed by Sp receiver functions. *Earth and Planetary Science Letters*.

Lekic, V., S. W. French, and K. M. Fischer 2011. Lithospheric thinning beneath rifted regions of Southern California. *Science 334*(6057), 783–787.

Levander, A., and M. S. Miller 2012. Evolutionary aspects of lithosphere discontinuity structure in the western US. *Geochemistry, Geophysics, Geosystems 13*(7).

Lockner, D. A., C. Morrow, D. Moore, and S. Hickman 2011. Low strength of deep San Andreas fault gouge from SAFOD core. *Nature 472*(7341), 82–85.

McKenzie, D. 1984. The Generation and Compaction of Partially Molten Rock. *Journal of Petrology 25*(3), 713–765.

McKenzie, D., and M. Bickle 1988. The volume and composition of melt generated by extension of the lithosphere. *Journal of Petrology 29*(3), 625–679.

Menzies, M. A., S. L. Klemperer, C. J. Ebinger, and J. Baker 2002. Characteristics of volcanic rifted margins. *Geological Society of America Special Papers* **362**, 1–14.

Middleton, T. A., and A. Copley 2013. Constraining fault friction by re-examining earthquake nodal plane dips. *Geophysical Journal International*, 427.

Mittal, R., and G. Iaccarino 2005. Immersed boundary methods. *Annu. Rev. Fluid Mech.* **37**, 239–261.

Moore, W. B., G. Schubert, and P. Tackley 1998. Three-dimensional simulations of plume-lithosphere interaction at the Hawaiian swell. *Science 279*(5353), 1008–1011.

Moore, W. B., G. Schubert, and P. J. Tackley 1999. The role of rheology in lithospheric thinning by mantle plumes. *Geophysical Research Letters 26*(8), 1073–1076.

Moresi, L., and V. Solomatov 1998. Mantle convection with a brittle lithosphere: thoughts on the global tectonic styles of the Earth and Venus. *Geophysical Journal International 133*(3), 669–682.

Morgan, J. 1981. Hotspot tracks and the opening of the Atlantic and Indian oceans. In C. Emiliani (Ed.), *The Oceanic Lithosphere*, Volume 7. of *The Sea.*, pp. 443–487. New York, N.Y.: John Wiley and Sons, Inc.

Morgan, J. 1983. Hotspot tracks and the early rifting of the Atlantic. *Tectonophysics 94*(1-4), 123–139.

Morgan, J. P. 1987. Melt migration beneath midocean spreading centers. *Geophysical Research Letters 14*(12), 1238–1241.

Noda, H., and N. Lapusta 2013. Stable creeping fault segments can become destructive as a result of dynamic weakening. *Nature 493*(7433), 518–521.

Nyblade, A. A., and C. A. Langston 1995. East African earthquakes below 20 km depth and their implications for crustal structure. *Geophysical Journal International 121*(1), 49–62.

Nyblade, A. A., and S. W. Robinson 1994. The African Superswell. *Geophys. Res. Lett. 21*(9), 765–768.

Olson, P., and G. Corcos 1980. A boundary layer model for mantle convection with surface plates. *Geophysical Journal International 62*(1), 195–219.

Phipps Morgan, J. 2001. Thermodynamics of pressure release melting of a veined plum pudding mantle. *Geochemistry, Geophysics, Geosystems 2*(4).

Press, W. H. 2007. *Numerical recipes 3rd edition: The art of scientific computing.* Cambridge university press.

Renner, J., K. Viskupic, G. Hirth, and B. Evans 2003. Melt extraction from partially molten peridotites. *Geochem. Geophys. Geosyst. 4*(5).

Ribe, N., and U. Christensen 1994. Threedimensional modeling of plumelithosphere interaction. *Journal of Geophysical Research: Solid Earth (19782012) 99*(B1), 669–682.

Ribe, N. M. 1985. The deformation and compaction of partial molten zones. *Geophysical Journal International 83*(2), 487–501.

Rice, J. R., and M. Cocco 2007. *Tectonic Faults: Agents of Change on a Dynamic Earth*, Chapter Seismic fault rheology and earthquake dynamics, pp. 99–137. MIT Press.

Rooney, T. O. 2010. Geochemical evidence of lithospheric thinning in the southern Main Ethiopian Rift. *Lithos 117*(1), 33–48.

Rooney, T. O., I. D. Bastow, and D. Keir 2011. Insights into extensional processes during magma assisted rifting: Evidence from aligned scoria cones. *Journal of Volcanology and Geothermal Research 201*(1-4), 83–96.

Rooney, T. O., I. D. Bastow, D. Keir, F. Mazzarini, E. Movsesian, E. B. Grosfils, J. R. Zimbelman, M. S. Ramsey, D. Ayalew, and G. Yirgu 2014. The protracted development of focused magmatic intrusion during continental rifting. *Tectonics*.

Rooney, T. O., C. Herzberg, and I. D. Bastow 2012. Elevated mantle temperature beneath East Africa. *Geology 40*(1), 27–30.

Royden, L., J. Sclater, and R. V. Herzen 1980. Continental margin subsidence and heat flow: important parameters in formation of petroleum hydrocarbons. *Bull. Am. Assoc. Pet. Geol.* **64**, 173–187.

Rubin, A. M. 1995. Propagation of Magma-Filled Cracks. *Annual Review of Earth and Planetary Sciences 23*(1), 287–336.

Rubin, A. M. 1998. Dike ascent in partially molten rock. *Journal of Geophysical Research 103*(20), 901–20.

Rychert, C. A., K. M. Fischer, and S. Rondenay 2005. A sharp lithosphere-asthenosphere boundary imaged beneath eastern North America. *Nature 436*(7050), 542–545.

Rychert, C. A., J. O. Hammond, N. Harmon, J. M. Kendall, D. Keir, C. Ebinger, I. D. Bastow, A. Ayele, M. Belachew, and G. Stuart 2012. Volcanism in the Afar Rift sustained by decompression melting with minimal plume influence. *Nature Geoscience 5*(6), 406–409.

Rychert, C. A., N. Harmon, and C. Ebinger 2014. Receiver function imaging of lithospheric structure and the onset of melting beneath the Galpagos Archipelago. *Earth and Planetary Science Letters* **388**, 156–165.

Rychert, C. A., G. Laske, N. Harmon, and P. M. Shearer 2013. Seismic imaging of melt in a displaced Hawaiian plume. *Nature Geoscience 6*(8), 657–660.

Rychert, C. A., N. Schmerr, and N. Harmon 2012. The Pacific lithosphere-asthenosphere boundary: Seismic imaging and anisotropic constraints from SS waveforms. *Geochemistry, Geophysics, Geosystems 13*(9), –.

Rychert, C. A., and P. M. Shearer 2011. Imaging the lithosphere-asthenosphere boundary beneath the Pacific using SS waveform modeling. *J. Geophys. Res. 116*(B7).

Schmeling, H. 2010. Dynamic models of continental rifting with melt generation. *Tectonophysics 480*(1), 33–47.

Schmeling, H., and H. Wallner 2012. Magmatic lithospheric heating and weakening during continental rifting: A simple scaling law, a 2D thermomechanical rifting model and the East African Rift System. *Geochemistry, Geophysics, Geosystems 13*(8).

Schmerr, N. 2012. The Gutenberg Discontinuity: Melt at the Lithosphere-Asthenosphere Boundary. *Science 335*(6075), 1480–1483.

Schmitt, A., and J. Vazquez 2006. Alteration and remelting of nascent oceanic crust during continental rupture: evidence from zircon geochemistry of rhyolites and xenoliths from the Salton Trough, California. *Earth and Planetary Science Letters 252*(3), 260–274.

Scott, T., and D. L. Kohlstedt 2006. The effect of large melt fraction on the deformation behavior of peridotite. *Earth and Planetary Science Letters 246*(3–4), 177–187.

Shudofsky, G. N., S. Cloetingh, S. Stein, and R. Wortel 1987. Unusually deep earthquakes in East Africa: Constraints on the thermomechanical structure of a continental rift system. *Geophysical Research Letters 14*(7), 741–744.

Simpson, G., M. Spiegelman, and M. I. Weinstein 2010. A multiscale model of partial melts: 2. Numerical results. *J. Geophys. Res. 115*(B4).

Sleep, N. H. 1987. Lithospheric heating by mantle plumes. *Geophysical Journal International 91*(1), 1–11.

Sleep, N. H. 1988. Tapping of melt by veins and dikes. *Journal of Geophysical Research 93*(B9), 10255–10.

Sleep, N. H. 1990. Hotspots and Mantle Plumes: Some Phenomenology. *J. Geophys. Res. 95*(B5), 6715–6736.

Sleep, N. H. 1994. Lithospheric thinning by midplate mantle plumes and the thermal history of hot plume material ponded at sublithospheric depths. *Journal of Geophysical Research: Solid Earth (19782012) 99*(B5), 9327–9343.

Sparks, D. W., and E. M. Parmentier 1991. Melt extraction from the mantle beneath spreading centers. *Earth and Planetary Science Letters 105*(4), 368–377.

Spiegelman, M. 1993a. Flow in deformable porous media. Part 1 Simple analysis. *Journal of Fluid Mechanics* **247**, 17–38.

Spiegelman, M. 1993b. Flow in deformable porous media. Part 2 Numerical analysis; the relationship between shock waves and solitary waves. *Journal of Fluid Mechanics* **247**, 39–63.

Spiegelman, M., P. B. Kelemen, and E. Aharonov 2001. Causes and consequences of flow organization during melt transport: The reaction infiltration instability in compactible media. *J. Geophys. Res. 106*(B2), 2061–2077.

Spiegelman, M., and D. McKenzie 1987. Simple 2-D models for melt extraction at mid-ocean ridges and island arcs. *Earth and Planetary Science Letters 83*(1-4), 137–152.

Spohn, T., and G. Schubert 1982. Convective thinning of the lithosphere: a mechanism for the initiation of continental rifting. *Journal of Geophysical Research: Solid Earth (19782012) 87*(B6), 4669–4681.

Stamps, D. S., E. Calais, E. Saria, C. Hartnady, J. Nocquet, C. J. Ebinger, and R. M. Fernandes 2008. A kinematic model for the East African Rift. *Geophysical Research Letters 35*(5).

Stevenson, D. 1986. On the role of surface tension in the migration of melts and fluids. *Geophysical Research Letters 13*(11), 1149–1152.

Stevenson, D. J. 1989. Spontaneous small-scale melt segregation in partial melts undergoing deformation. *Geophys. Res. Lett. 16*(9), 1067–1070.

Theunissen, K., J. Klerkx, A. Melnikov, and A. Mruma 1996. Mechanisms of inheritance of rift faulting in the western branch of the East African Rift, Tanzania. *Tectonics 15*(4), 776–790.

Tommasi, A., and A. Vauchez 2001. Continental rifting parallel to ancient collisional belts: an effect of the mechanical anisotropy of the lithospheric mantle. *Earth and Planetary Science Letters 185*(1), 199–210.

Tseng, Y.-H., and J. H. Ferziger 2003. A ghost-cell immersed boundary method for flow in complex geometry. *Journal of Computational Physics 192*(2), 593–623.

Turcotte, D., and G. Schubert 2002. *Geodynamics* (2 ed.). New York, N.Y.: Cambridge University Press.

Udaykumar, H., R. Mittal, P. Rampunggoon, and A. Khanna 2001. A sharp interface Cartesian grid method for simulating flows with complex moving boundaries. *Journal of Computational Physics 174*(1), 345–380.

Van Leer, B. 1977. Towards the ultimate conservative difference scheme. IV. A new approach to numerical convection. *Journal of Computational Physics 23*(3), 276–299.

Wark, D. A., and E. B. Watson 1998. Grain-scale permeabilities of texturally equilibrated, monomineralic rocks. *Earth and Planetary Science Letters 164*(3-4), 591–605.

Weeraratne, D. S., D. W. Forsyth, K. M. Fischer, and A. A. Nyblade 2003. Evidence for an upper mantle plume beneath the Tanzanian craton from Rayleigh wave tomography. *Journal of Geophysical Research 108*(B9).

White, R., and D. McKenzie 1989. Magmatism at Rift Zones: The Generation of Volcanic Continental Margins and Flood Basalts. *J. Geophys. Res. 94*(B6), 7685–7729.

Wolbern, I., G. Rmpker, K. Link, and F. Sodoudi 2012. Melt infiltration of the lower lithosphere beneath the Tanzania craton and the Albertine rift inferred from S receiver functions. *Geochemistry, Geophysics, Geosystems 13*(8).

Woldegabriel, G., J. L. Aronson, and R. C. Walter 1990. Geology, geochronology, and rift basin development in the central sector of the Main Ethiopia Rift. *Geological Society of America Bulletin 102*(4), 439–458.

Wong, T.-F., S.-C. Ko, and D. L. Olgaard 1997. Generation and maintenance of pore pressure excess in a dehydrating system 2. Theoretical analysis. *J. Geophys. Res. 102*(B1), 841–852.

Yuen, D. A., and L. Fleitout 1985. Thinning of the lithosphere by small-scale convective destabilization. *Nature* **313**, 125–128.

Zoback, M. D., M. L. Zoback, V. S. Mount, J. Suppe, J. P. Eaton, J. H. Healy, D. Oppenheimer, P. Reasenberg, L. Jones, and C. B. Raleigh 1987. New evidence on the state of stress of the San Andreas fault system. *Science 238*(4830), 1105–1111.

3.9 Tables and Figures

Symbol	Description	Symbol	Description
q_c	convective heat flux	$x_{\mathrm{L}}, z_{\mathrm{L}}$	LAB coordinates
q_m	melt infiltration heat flux	$\hat{n}$	LAB unit normal vector
q	total heat flux, $q_c + q_m$	θ	local LAB slope
ϕ	melt fraction (i.e., porosity)	z	depth
η_s	solid shear viscosity	x	horizontal coordinate
ξ	compaction viscosity	σ	deviatoric stress
k	permeability	$\dot{\Gamma}$	meting rate
T	temperature	$\underline{V}_B$	LAB velocity
$\underline{V}^s$	solid velocity	F_r	resisting frictional force
$\underline{v}^f$	fluid velocity	$\dot{\epsilon}$	strain rate
$\underline{S}$	Darcy flux	P_h	hydrostatic pressure
S_d	dike flux	D_k	diking efficiency, S_d/S_b

Table 3.1: Variables, vectors noted by underline.

Symbol	Description	Range
μ	coefficient of friction	0.12 - 0.36
$\frac{\mathrm{d}F}{\mathrm{d}P}$	peak melt productivity	3 - 10 % GPa^{-1}
q_o	initial basal heat flux for initial geotherm	20-30 mWm^{-2}

Table 3.2: Parameter range

Symbol	Description	Value/Definition
k_T	thermal conductivity	3 W $m^{-1}K^{-1}$
κ	thermal diffusivity	10^{-6} m^2s^{-1}
α	thermal expansivity	3×10^{-5} K^{-1}
C_p	specific heat	10^3 J kg^{-1} K^{-1}
ρ_s	solid density	3300 kg m^{-3}
ρ_f	melt density	2700 kg m^{-3}
$\Delta\rho$	solid-melt density difference	$\rho_s - \rho_f$
a	grain size (for permeability)	1 cm
ΔT_v	viscous temperature scale	RT^2/Q [1]
R	gas constant	8.314 J mol^{-1} K^{-1}
g	gravitational acceleration	9.8 m s^{-2}
Q_{dis}	activation energy	530 kJ $mol^{-}1$ [2]
A_{dis}	pre-exponential constant	10^5 $MPa^{-n_{\text{dis}}}$ s^{-1} [2]
V_{dis}	activation volume	20 cm^3 $mol^{-}1$ [2]
n_{dis}	dislocation creep stress exponent	3.5 [2]
L	latent heat	500 J kg^{-1}
η_f	fluid shear viscosity	1 Pa s
S_b	buoyant Darcy flux	$\Delta\rho g k/\eta_f$
z_1, z_2	melting onset, termination depths	150, 100 km
x_p	melting decay scale in x	50 km
δ_z	melting decay scale in z	60 km
V_o	plume upwelling velocity	20 cm yr^{-1}
T_{LAB}	temperature at the LAB	1200^oC
F_o	extensional tectonic force	6 TN m^{-1}
LAB	lithosphere-asthenosphere boundary	
MER	Main Ethiopian Rift	

Table 3.3: Constants, abbreviations. References: [1] Grasset and Parmentier (1998), [2] Hirth and Kohlstedt (2003)

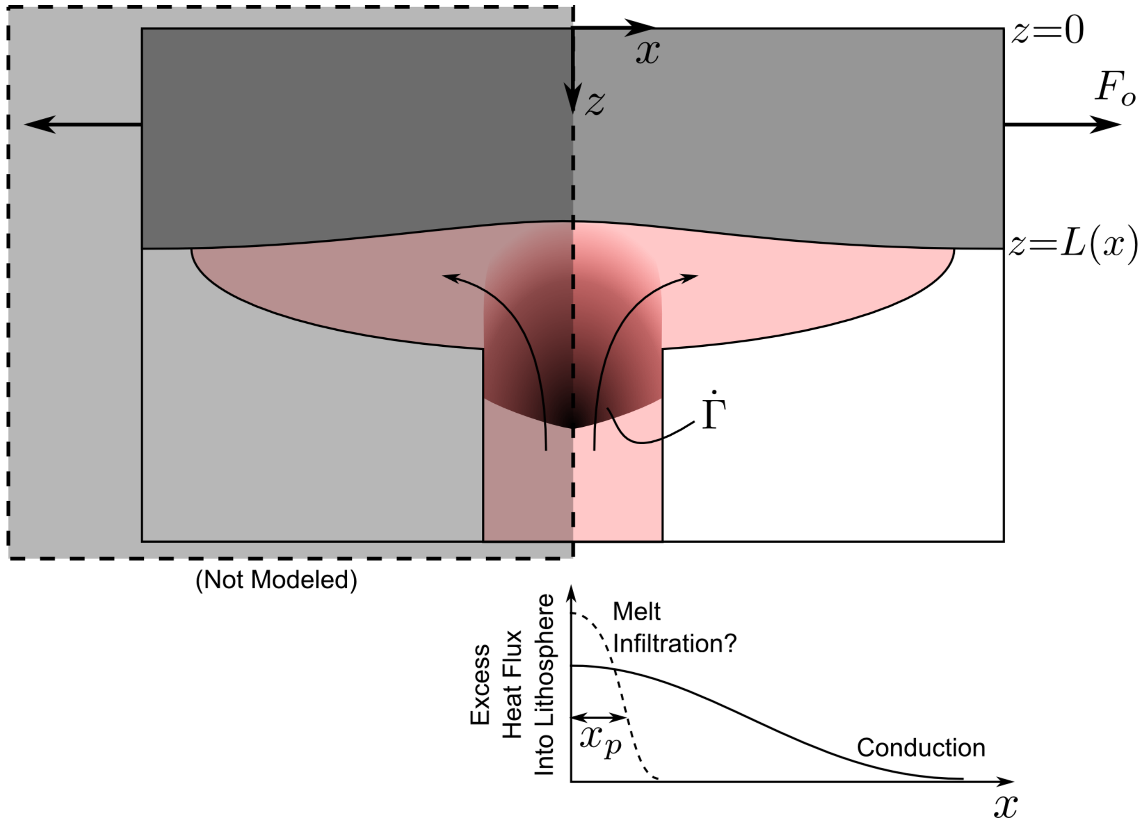

Figure 3.1: Conceptual setup of a plume impinging on a lithosphere subject to a horizontal tectonic force.

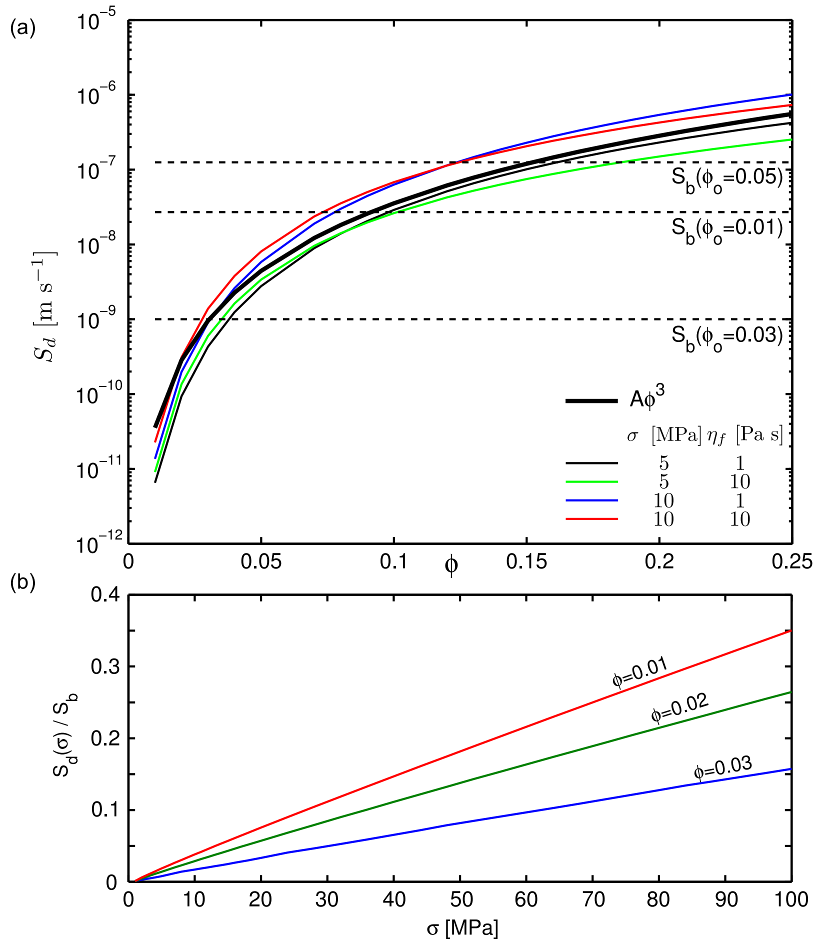

Figure 3.2: The diking flux dependence on (a) ϕ and (b) σ. Panel (a) is modified from Havlin *et al.* (2013).

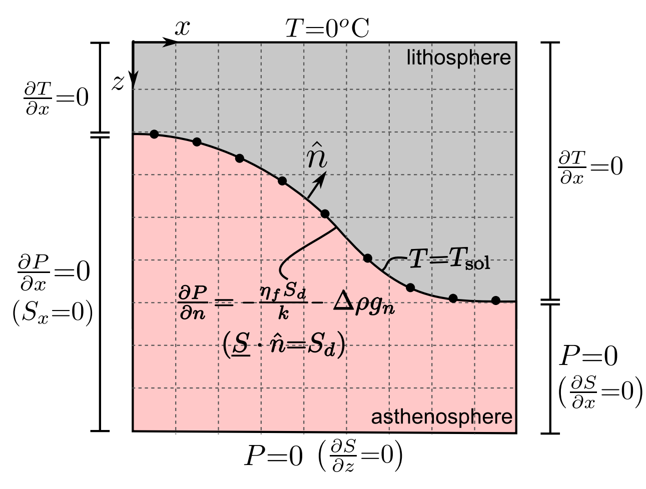

Figure 3.3: Boundary conditions for the lithosphere thermal solution and the asthenosphere melt migration solution.

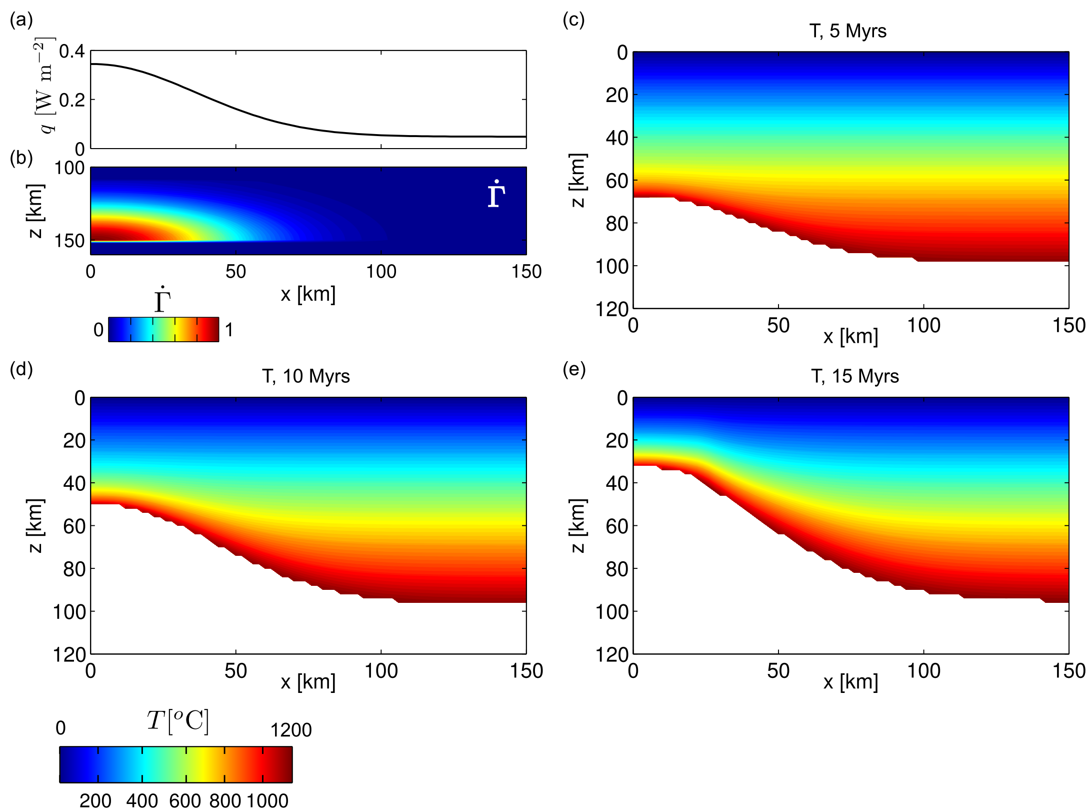

Figure 3.4: Prescribed heat flux and resulting temperature evolution for friction coefficient of 0.24, pre-plume heat flux of 30 mW m^{-2}, 6 TN m^{-1} of tectonic force, peak melt productivity of 6 % GPa^{-1} and plume velocity of 20 cm yr^{-1}.

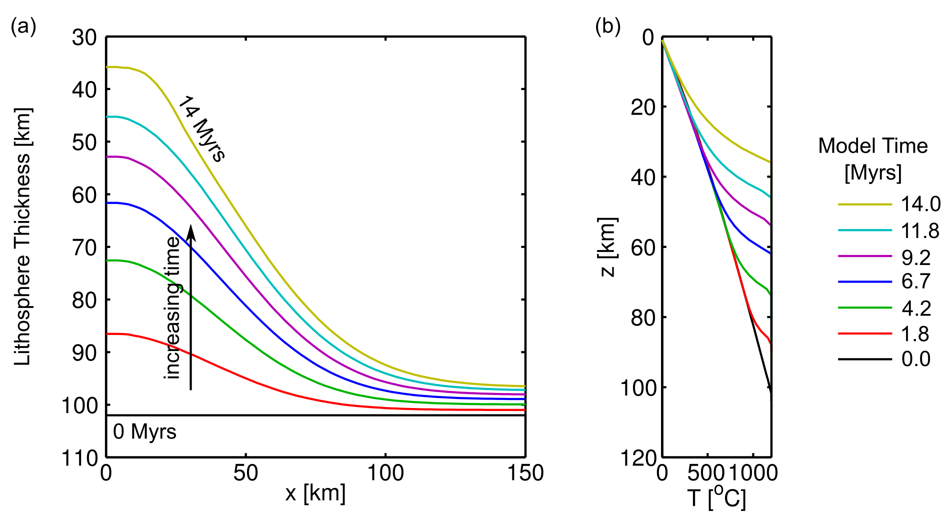

Figure 3.5: Boundary depth and temperature profiles at $x = 0$ for the case in figure 3.4 .

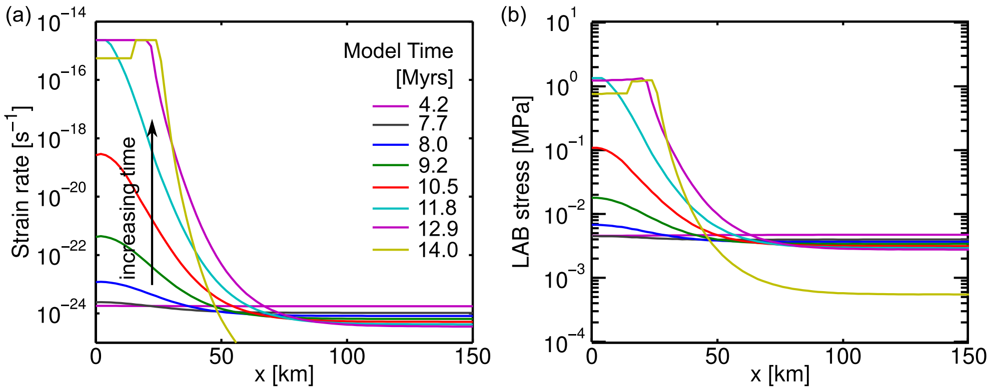

Figure 3.6: (a) strain rate and (b) stress at the LAB for the case in figure 3.4.

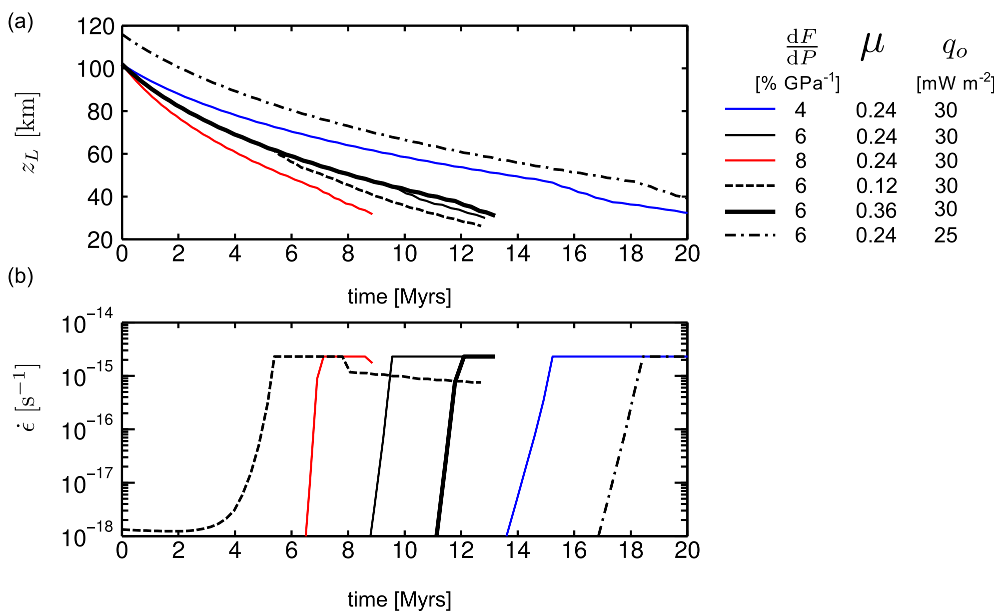

Figure 3.7: Sensitivity to controlling parameters for (a) lithosphere thinning and (b) strain rate. The peak melt productivity, friction coefficient and pre-plume heat flux (for calculating the initial geotherm) are shown in the legend. Colors indicate the productivity while line style indicate either friction coefficient or pre-plume heat flux.

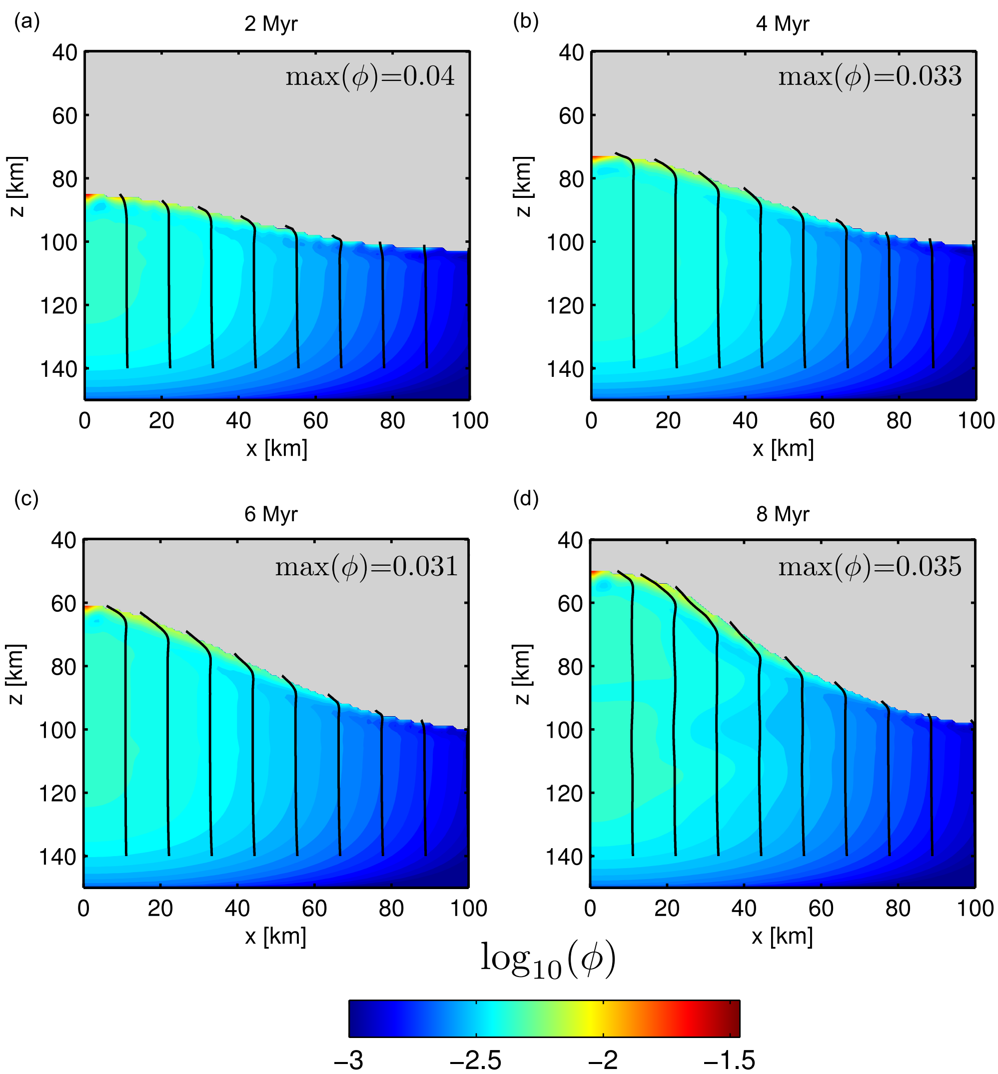

Figure 3.8: Quasi-steady melt fraction and melt streamlines at 2, 4, 6 and 8 Myr for melt productivity 6 % GPa^{-1} and friction coefficient 0.12.

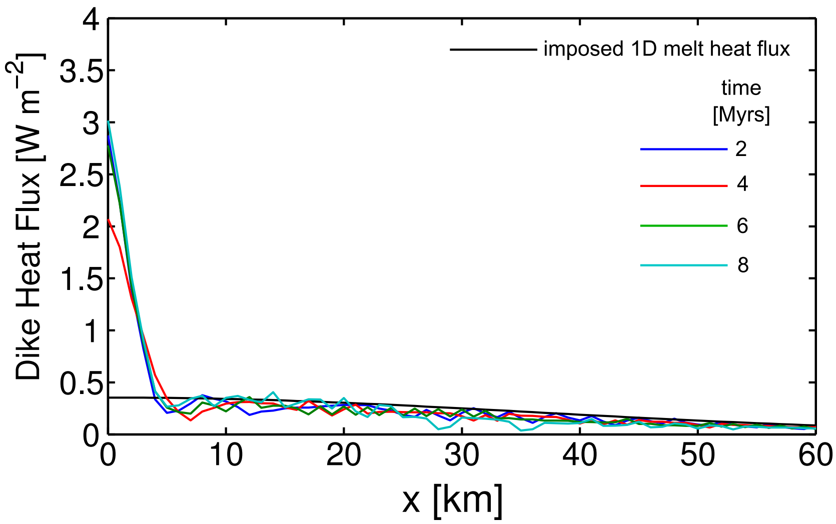

Figure 3.9: Imposed and calculated dike infiltration heat flux. The heat flux from 2D calculations is shown for the same times and parameters as figure 3.8.

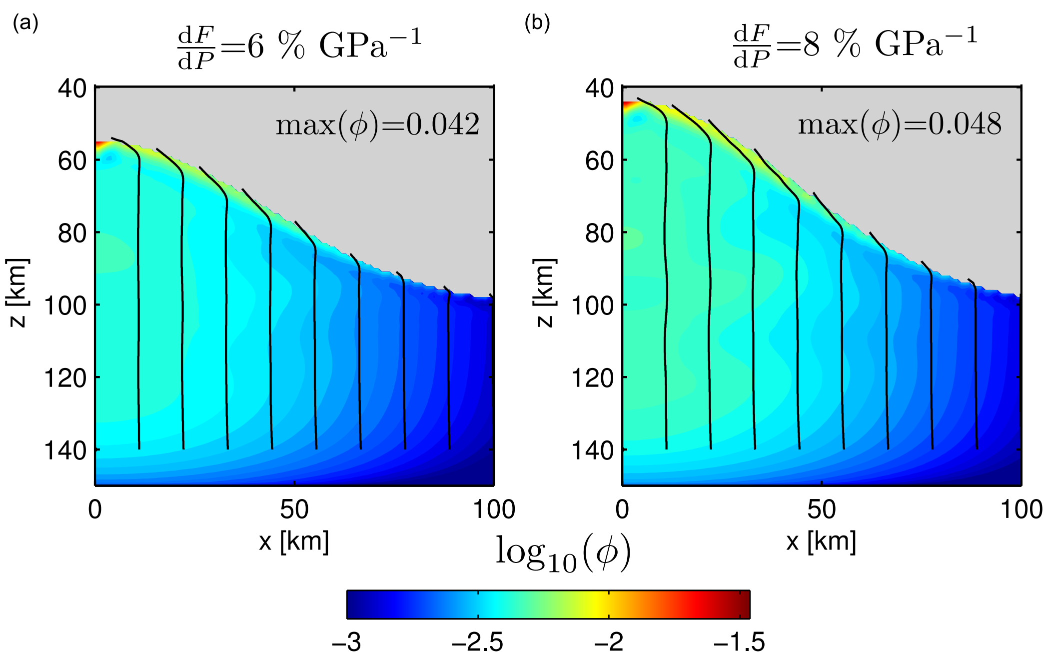

Figure 3.10: Quasi-steady melt fraction and melt streamlines at 8 Myr for a lithosphere with friction coefficient of 0.36. The melt productivity is (a) 6 % GPa^{-1} and (b) 8 % GPa^{-1}.

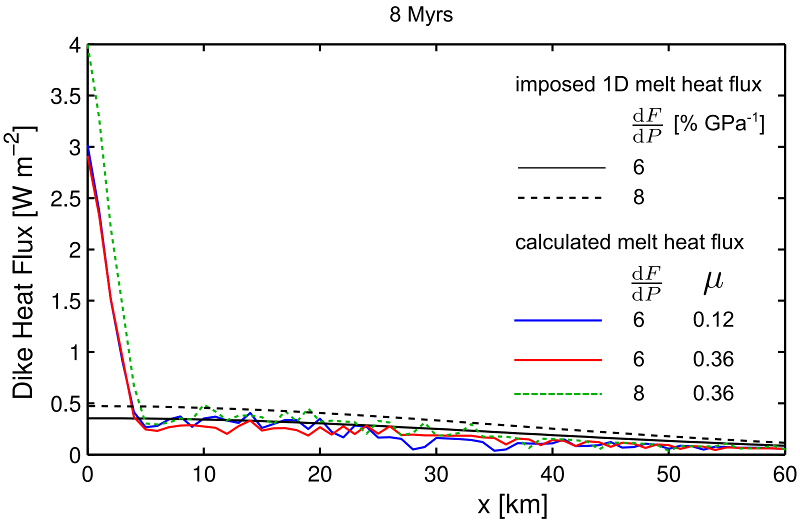

Figure 3.11: Imposed and calculated dike infiltration heat flux. The heat flux from 2D calculations is shown for the same times and parameters as figure 3.10.

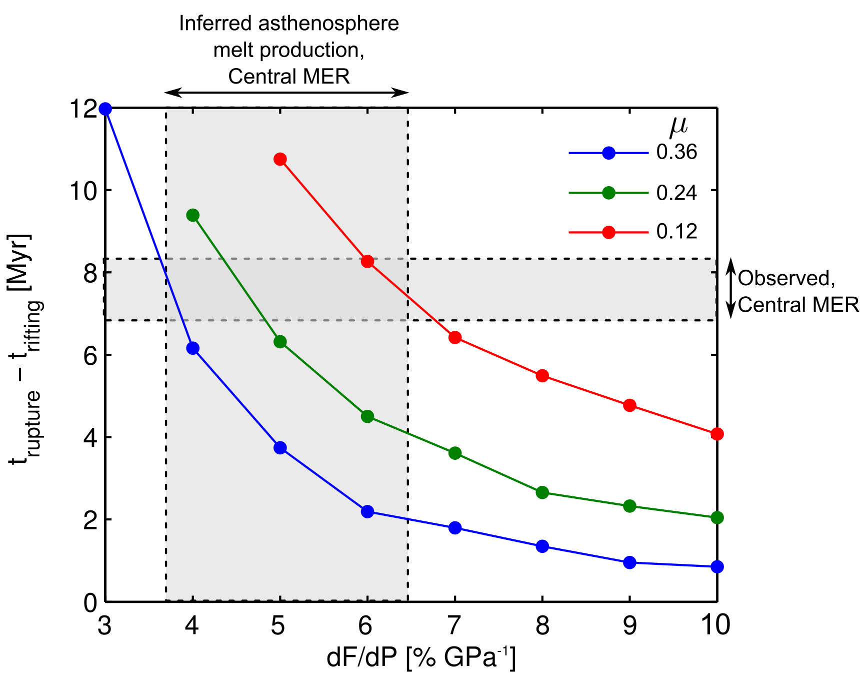

Figure 3.12: Predicted delay between onset of extension and lithosphere rupture (defined as when the LAB reaches the base of the crust). Shaded boxes indicate the observed time between the transfer of strain from border faults to magmatic segments in the central MER (Ebinger and Casey, 2001) and the possible range of melt productivity for peridotite with at an elevated potential temperature consistent with observations (Rooney *et al.*, 2012).

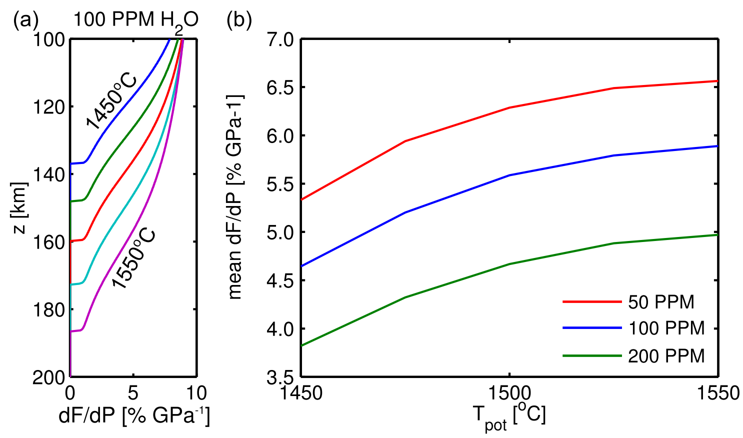

Figure 3.13: (a) melt productivity for peridotite with 100 PPM H_2O and potential temperature from 1450 to 1550^{o}C in 25^{o}C increments using a hydrous mantle peridotite (Katz *et al.*, 2003). (b) Average productivity over the melting column for increasing potential temperature and water content.